elektronisches dokument
ULB Sachsen-Anhalt

Structural study of human FKBP38 and its interaction with calmodulin by NMR and computational methods

Dissertation

zur Erlangung des akademisches Grades
Doctor rerum naturalium (Dr. rer. nat.)

vorgelegt an der Naturwissenschaftlichen Fakultät I der
Martin-Luther-Universität Halle-Wittenberg

von
Mitcheell Maestre Martínez
Geb. am 29. April 1974 in Havanna, Kuba

Halle/Saale, Februar 2008

Gutachter:

1. PD. Dr. Christian Lücke
   Max-Planck-Forschungsstelle für Enzymologie der Proteinfaltung, Halle/Saale
2. Prof. Dr. Milton T. Stubbs
   Martin-Luther-Universität Halle-Wittenberg
3. Prof. Dr. Thomas Peters
   Universität zu Lübeck

Verteidigungsdatum: 13.02.2008

urn:nbn:de:gbv:3-000014742
[http://nbn-resolving.de/urn/resolver.pl?urn=nbn%3Ade%3Agbv%3A3-000014742]

Index

1. Introduction ……..……..……. 1

1.1. PPIases ……...…..…..…… 1

1.1.1. Human FKBPs ……... 3

1.1.2. The human FKBP38 …….. 4

1.1.3. Three-dimensional structures of FKBPs …… 6

1.1.3.1. The prototypic FKBP12 ……..……. 6

1.1.3.2. FKBPs with TPR domains: FKBP51, FKBP52 and *At*FKBP42 …….. 8

1.2. Calcium and calcium-binding proteins ……. 11

1.2.1. Calmodulin ……..…….. 12

1.2.2. Calmodulin binding to target proteins ……..……. 14

1.3. Objectives …….…… 19

2. Materials and Methods …… 20

2.1. Materials ……... 20

2.1.1. Chemicals and materials …… 20

2.1.2. Enzymes ……. 21

2.1.3. Plasmids and templates …….. 21

2.1.4. PCR primers …….. 21

2.1.5. *Escherichia coli* cells ……. 22

2.1.6. Proteins and peptides ……. 22

2.1.7. Chromatography columns …….. 22

2.1.8. Standards ……... 22

2.1.9. Kits ……. 22

2.1.10. Buffers, media and stock solutions …… 22

2.1.11. Equipment …….. 23

2.2. Methods …… 23

2.2.1. Molecular biology methods ……... 23

2.2.1.1. Polymerase chain reaction …… 23

2.2.1.2. Agarose gel electrophoresis …….. 24

2.2.1.3. DNA quantification …….. 24

2.2.1.4. Enzymatic modification of DNA …….. 24

2.2.1.5. Plasmid mini-preparation ……. 25

2.2.1.6. Transformation into competent *Escherichia coli* cells ……. 25

2.2.1.7. Culturing of *Escherichia coli* cells 25
2.2.2. Preparative methods 25
2.2.2.1. Overexpression tests 25
2.2.2.2. Expression of recombinant FKBP38$^{35-153}$ 26
2.2.2.3. Lysis of *Escherichia coli* cells 26
2.2.2.4. Purification of FKBP38$^{35-153}$ 26
2.2.3. Analytical methods 26
2.2.3.1. SDS-PAGE 26
2.2.3.2. Protein quantification 27
2.2.3.3. Internet-based programs 27
2.2.4. NMR spectroscopy 27
2.2.4.1. Structural study of FKBP38$^{35-153}$ 27
2.2.4.1.1. Sample preparation 27
2.2.4.1.2. NMR experiments 28
2.2.4.1.3. Resonance assignment 28
2.2.4.1.4. Structure calculation and refinement 29
2.2.4.2. Study of the interactions of FKBP38$^{35-153}$ with Ca^{2+} and Mg^{2+} 30
2.2.4.3. Study of the interactions between FKBP38 and CaM 30
2.2.4.3.1. Resonance assignments of apo-CaM, holo-CaM and FKBP38$^{290-313}$ 30
2.2.4.3.2. Chemical shift perturbation experiments 31
2.2.4.3.3. Docking calculations 32
2.2.5. Molecular dynamics simulations 34
2.2.6. Crystal structure analysis of FKBP38$^{35-153}$ 36

3. Results and discussion 38
3.1. NMR assignment of the ^{1}H and ^{15}N resonances of FKBP38$^{35-153}$ 38
3.2. Three-dimensional structure of FKBP38$^{35-153}$ 42
3.3. Interaction of FKBP38$^{35-153}$ with Ca^{2+} and Mg^{2+} 47
3.4. Interaction of FKBP38$^{35-153}$ with calmodulin 52
3.4.1. NMR assignment of the backbone amide resonances of apo- and holo-calmodulin 52
3.4.2. Interaction of FKBP38$^{35-153}$ with apo-calmodulin 57
3.4.3. Interaction of FKBP38$^{35-153}$ with holo-calmodulin 62
3.4.4. Comparison of the interactions of FKBP38$^{35-153}$ with apo- and holo-

calmodulin …… 64
3.4.5. Three-dimensional structures of the FKBP38$^{35-153}$/CaM complexes …… 66
3.4.5.1. Three-dimensional structure of the FKBP38$^{35-153}$/apo-CaM complex 66
3.4.5.2. Three-dimensional structure of the FKBP38$^{35-153}$/holo-CaM complex 70
3.4.5.3. Comparison of the three-dimensional structures of the FKBP38$^{35-153}$/CaM complexes ……... 74
3.5. Interaction of FKBP38$^{290-313}$ with holo-calmodulin …… 75
3.5.1. Three-dimensional structure of the FKBP38$^{290-313}$/holo-CaM complex …... 79
3.6. Three-dimensional models of the overall FKBP38/CaM complexes …….. 82
3.6.1. Comparison of the overall FKBP38/CaM complexes with other known CaM complexes …… 84

4. Summary ……. 86

5. References ……... 89

6. Figure Index …… 99

7. Abbreviations …….. 103

8. Appendix ……. 105
8.1. Acknowledgments ……... 105
8.2. Publications …….. 106
8.3. Curriculum vitae …….. 107

Eidesstattliche Erklärung …….. 108

1. Introduction

The human FK506-binding protein 38 (FKBP38) is a constitutively inactive peptidyl prolyl cis/trans isomerase (PPIase) that is activated by calmodulin (CaM) and calcium (Ca^{2+}). Furthermore, this protein plays a key role in Bcl-2 related apoptotic pathways (Edlich et al., 2005; Edlich et al., 2006). Because of all these singular properties, the molecular structure of FKBP38 and the characterization of its interaction with CaM are of major interest.

1.1. PPIases

Proteins play a fundamental role in virtually every biological process, displaying a multitude of functions such as the catalysis of biochemical reactions, the transmission of biological messages in signal transduction pathways, and the trafficking of a wide variety of chemical substances across cell membranes. All proteins are synthesized in the ribosome as linear polypeptide chains. In order to become biologically active, the polypeptide chain has to fold into a unique native three-dimensional structure. Moreover, the failure of proteins to fold correctly and efficiently is associated with the malfunction of biological systems. A variety of diseases such as cystic fibrosis and Alzheimer's disease are the result of protein misfolding (Chaudhuri and Paul, 2006; Cohen and Kelly, 2003).

Although the information for correct folding is encoded by the amino acid sequence for most proteins (Anfinsen, 1973), living organisms are additionally equipped with an efficient folding machinery, consisting of chaperones (Bukau et al., 2006; Hartl, 1996), protein disulfide isomerases (Ellgaard and Ruddock, 2005) and peptide bond isomerases (Fischer, 1994; Fischer and Aumüller, 2003).

Peptide bond isomerases assist the *cis/trans* interconversion of peptide bonds, which possess partial double bond character due to the delocalization of the lone electron pair of the nitrogen atom across the entire amide group. Peptide bonds therefore can only adopt two planar conformations (*cis* or *trans*), which interconvert slowly in comparison with the other torsion angles that define the protein conformation. There are two classes of peptide bond isomerases: (i) the secondary amide peptide bond isomerases (APIases) (Schiene-Fischer et al., 2002) and (ii) the major class of the peptidyl prolyl *cis/trans* isomerases (PPIases, Enzyme class 5.2.1.8.) (Fischer et al., 1989) which assists the interconversion of peptide bonds where proline is in the C-terminal position.

PPIases are ubiquitous in life. The subfamilies of this enzyme class (i) are unrelated to each other in their amino acid sequences, (ii) have distinct substrate specificities, and (iii) prove to be sensitive to different inhibitors. A classification of these enzymes according to their ligand-specificity and sequence similarities allows the identification of three PPIases families: the FK506-binding proteins (FKBPs), the cyclophilins (Cyps) and the parvulins. The members of the first two families are characterized by their ability to bind the low-molecular-weight compounds FK506 (also known as tacrolimus) and cyclosporin A (CsA), producing highly immunosuppressive complexes that lead to the inhibition of T-cell proliferation. Therefore PPIases of these two families are also referred to as immunophilins.

Although no sequence homologies exist between the three PPIase families, the structure of the active site is very similar in all of these enzymes, suggesting that the catalytic pathway utilized by FKBPs, cyclophilins and parvulins is closely related. Albeit several fundamental parameters describing the enzymatic catalysis mediated by PPIases are different, a common pattern of structural motifs has been found in the three-dimensional structures of FKBP and parvulin domains, leading to the definition of an FKBP-like superfold (Sekerina et al., 2000). Hence, the question of how catalysis is carried out by these enzymes still remains open (Fanghänel and Fischer, 2004).

PPIases can consist of one or more PPIase domains, complemented by additional functional segments, such as protein-interaction domains/sites and membrane anchors. These additional segments have been found both N-terminal and C-terminal to the catalytic domain (Galat, 2004a,b) and may account for the regulation and specific localization of the enzymes.

Besides the catalysis of peptidyl prolyl *cis/trans* isomerization, which can play a role in *de novo* protein folding (Brandts et al., 1975; Wedemeyer et al., 2002), native state isomerization (Andreotti, 2003) and signal transduction (Wulf et al., 2005; Lin and Lechleiter, 2002), additional molecular mechanisms have been reported for the physiological function of PPIases. They can act, for example, as presenter proteins in immunosuppression when they bind low-molecular-weight immunosuppressants such as CsA and FK506. The PPIase-inactive Cyp18/CsA and FKBP12/FK506 complexes are able to bind and subsequently inhibit the role of the protein phosphatase calcineurin (protein phosphatase 2B, CaN) in signal transduction events that lead to T-cell proliferation (Vogel et al., 2001; Liu et al., 1991; McCaffrey et al., 1993; Shibasaki et al., 1996). Remarkably, only the immunosuppressant/PPIase complexes and not the individual PPIases or immunosuppressants are able to display this affinity to CaN in what is called a “gain of function” mechanism. A proline-directed binding function and a holding

function for unfolded polypeptide chains are other reported mechanisms of action of PPIases (Fischer and Aumüller, 2003).

1.1.1. Human FKBPs

A total of 16 different FK506-binding proteins have been reported in human cells (Figure 1). Members of this enzyme family can be found in all human tissues. The majority of them are multidomain proteins, consisting of one or more FKBP domains as well as different signal sequences and protein-interaction domains, such as tetratricopeptide repeat (TPR) domains and calmodulin binding sites (Galat, 2004b). In some FKBPs with multiple FKBP domains, PPIase activity has been found only in the first N-terminal FKBP domain when using the standard PPIase assay (Barent et al., 1998). Common characteristics of all constitutive active human FKBPs are (i) the PPIase activity, (ii) the binding of the macrolide FK506, and (iii) the inhibition of CaN by the formation of the FKBP/FK506/CaN complex (Weiwad et al., 2006).

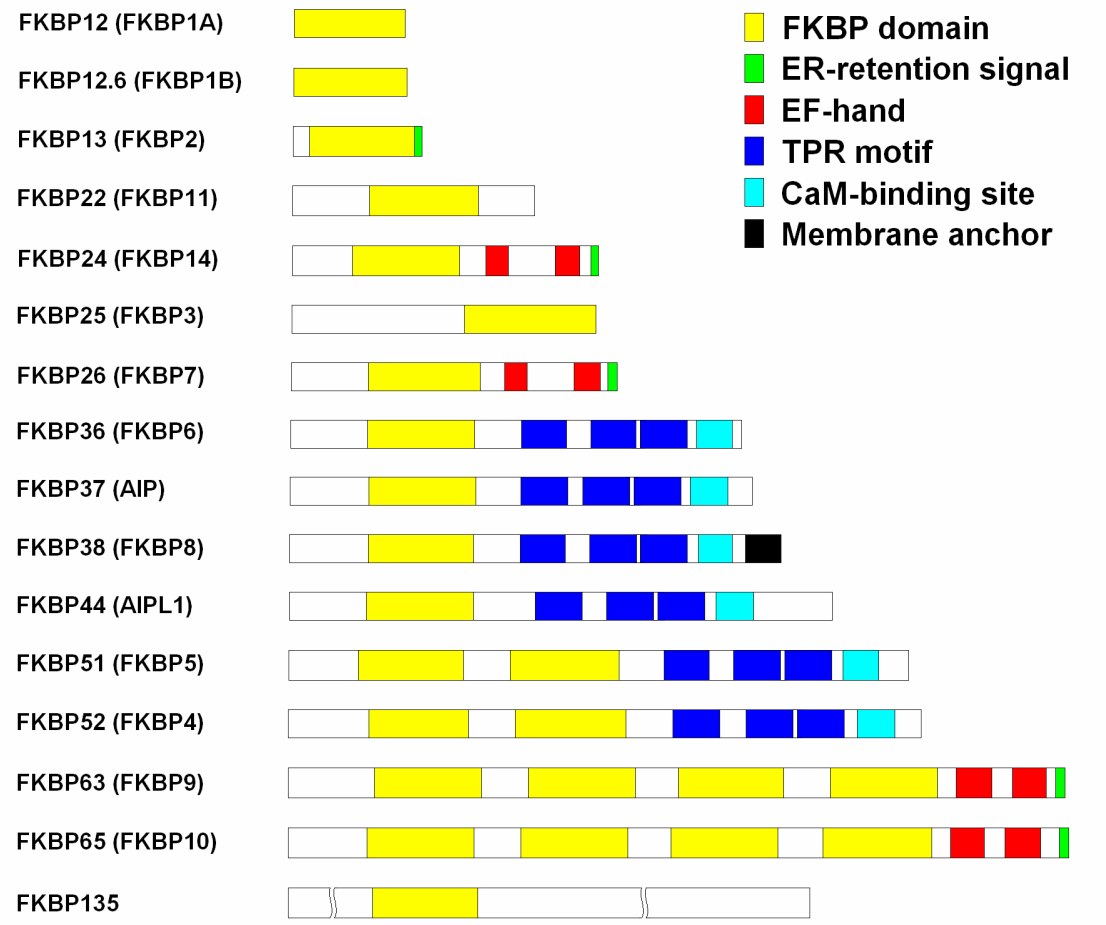

Figure 1. Schematic representation of the human FKBPs and their domain structures. The gene names are shown in the brackets. Kindly provided by Dr. Frank Edlich.

A variety of physiological functions have been assigned to FKBPs. They are involved in

spermatogenesis (Crackower et al., 2003), Ca^{2+} homeostasis (Wehrens et al., 2004) as well as Bcl-2-dependent apoptotic pathways (Edlich et al., 2005) and cytoplasmic receptors (Pratt et al., 1999). Mutations in FKBP genes are related to the occurrence of congenital diseases such as the Williams Beuren syndrome (WBS, OMIM 194050) and the Leber congenital amaurosis (LCA, OMIM 204000) (Meng et al., 1998; Sohocki et al., 2000; Ramamurthy et al., 2003).

Another relevant biological feature of the PPIases concerns the effects of their complexes with the low molecular compounds FK506 and rapamycin (a secondary metabolite from *Streptomyces higroscopicus*) on the signal pathways of cell proliferation. In a fashion similar to the previously described role of the FKBP12/FK506 complex in the inhibition of T-cell proliferation, the complex of FKBP12 and rapamycin inhibits the protein kinase mTOR (mammalian target of rapamycin) (Sabers et al., 1995). This inhibition of mTOR in turn interferes with the activation of the phosphatidylinositol 3-kinase/protein kinase B (PI3K/Akt) signal pathway (Fingar and Blenis, 2004), thus also inhibiting T-cell proliferation.

1.1.2. The human FKBP38

The human FKBP38 (gene name FKBP8) was first characterized as a result of a very pronounced expression of its corresponding mRNA in neuronal cells (Lam et al., 1995). The protein consists of 355 amino acids, which are organized in an N-terminal FKBP domain, a TPR domain consisting of three TPR motifs and an associated putative calmodulin-binding site, and a C-terminal membrane anchor that is unique among human FKBPs and leads to the localization of FKBP38 in the membranes of the endoplasmatic reticulum and the mitochondria (Edlich et al., 2005; Wang et al., 2006). A similar domain organization has also been found in FKBP42 from plants (Kamphausen et al., 2002). The first 34 residues in the FKBP38 sequence, located N-terminal to the FKBP domain, are supposedly non-structured based on secondary structure predictions. A report, however, indicates that FKBP38 derives from a truncated ORF (open reading frame), and that the extended form of this protein would present an extra N-terminal segment of 57 residues, thus comprising 412 amino acids and reaching a molecular weight of 45 kDa (Nielsen et al., 2004).

FKBP38 was originally reported as an inherent calcineurin inhibitor, suggesting that it is the only immunophilin able to inhibit the phosphatase activity of CaN and thus to interfere with the CaN/NFAT pathway in the absence of FK506 (Shirane and Nakayama, 2003). Later reports, however, clearly demonstrated that in the absence of bound FK506 FKBP38 does not inhibit CaN, ruling out a possible role as endogenous CaN inhibitor (Kang et al., 2005; Weiwad et al.,

2005). Only the CaM/Ca^{2+}/FKBP38/FK506 complex can inhibit CaN, but to a much lower extent than FKBP12, FKBP12.6 or FKBP51 (Weiwad et al., 2006). An indirect effect of FKBP38 on the subcellular localization of CaN, which is mediated by typical CaN ligands such as B cell lymphoma protein 2 (Bcl-2), was also reported (Weiwad et al., 2005).

A remarkable property of FKBP38 is the lack of constitutive FKBP activity of its FKBP domain. Thus, this protein cannot bind FK506 or catalyze the peptidyl prolyl *cis/trans* isomerization by itself (Edlich et al., 2005; Kang et al., 2005). Moreover, the enzymatic activity of this protein is regulated by CaM/Ca^{2+}, which is a unique property among human FKBPs. Only the CaM/Ca^{2+}/FKBP38 complex exhibits PPIase activity and is able to bind FK506 (Edlich et al., 2005).

The active form of FKBP38 interacts with Bcl-2, which is known to be a key player in the control of apoptosis. The formation of the Bcl-2/FKBP38/CaM/Ca^{2+} complex interferes with the binding of Bcl-2 to its cellular targets, such as CaN or Bad. Thus, the active form of FKBP38 participates in apoptosis control by inhibition of the anti-apoptotic Bcl-2 function (Figure 2) (Edlich et al., 2005). The formation of the Bcl-2/FKBP38/CaM/Ca^{2+} complex can be prevented by application of low-molecular-weight FKBP38 inhibitors. In fact, the inhibition of FKBP38 by active site-directed ligands or the reduction of cellular FKBP38 levels by FKBP38 RNAi in neuroblastoma cells resulted in a prevention of apoptosis that is induced by etoposide, daunorubicin, camptothecin or ionomycin (Edlich et al., 2005). This result strongly suggests a role of FKBP38 in the regulation of apoptosis in neuronal systems. Moreover, the specific FKBP38 inhibitor N-(N',N'-dimethylcarboxamidomethyl)cycloheximide (DM-CHX) has demonstrated neuroregenerative and neuroprotective properties in a rat model of transient focal cerebral ischemia (Edlich et al., 2006). The fact that FKBP38 also influences the cell size regulation by the human tumor suppressor proteins (TSC) (Rosner et al., 2003) is another indication of the key role of FKBP38 in the regulation of apoptosis in neuronal cells.

A number of results have been published suggesting an anti-apoptotic function of FKBP38 in HeLa cells. Thereby, FKBP38 was suggested to target Bcl-2 to the mitochondria (Shirane and Nakayama, 2003), and to play a role in the folding and stabilization of Bcl-2 (Kang et al., 2005). The interaction of presenilins with FKBP38 was claimed to promote apoptosis by reducing the levels of mitochondrial Bcl-2 (Wang et al., 2005). Furthermore, the down regulation of FKBP38 with siRNA was associated with the activation of caspase-3 dependent apoptosis (Kang et al., 2005). The controversial duality of this protein as both pro-apoptotic and anti-apoptotic regulator has been attributed to the different cell lines used in the different studies (Kang et al., 2005).

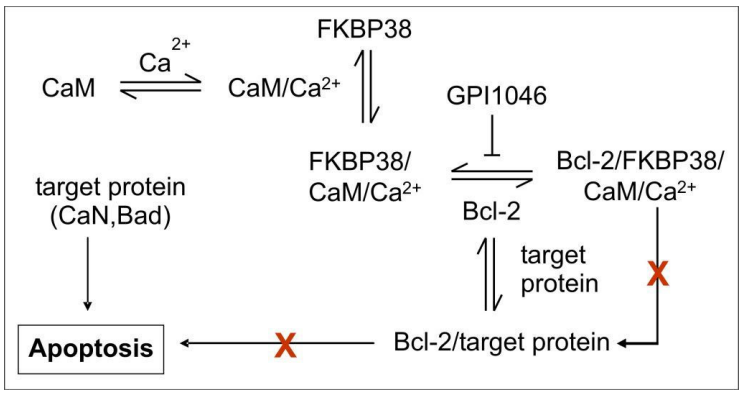

Figure 2. Model of the regulation of apoptosis by FKBP38 in neuroblastoma cells. First, the increase of the cytoplasmatic Ca^{2+}-concentration produces an activation of CaM in form of CaM/Ca^{2+}. Then, the $FKBP38/CaM/Ca^{2+}$ complex is formed, which subsequently inhibits Bcl-2 by the formation of the $Bcl-2/FKBP38/CaM/Ca^{2+}$ complex. In case of apoptosis induction, the inhibited Bcl-2 cannot bind its pro-apoptotic targets, and their activity can therefore lead to apoptosis. The inhibition of Bcl-2 by the $FKBP38/CaM/Ca^{2+}$ complex can be prevented by application of specific FKBP38 inhibitors, such as GPI1046. Kindly provided by Dr. Frank Edlich.

The active form of FKBP38 (i.e. the $FKBP38/CaM/Ca^{2+}$ complex) has furthermore been found to interact with Hsp90 in a similar manner as other FKBPs with TPR domains such as for example FKBP51 (Okamoto et al., 2006; Edlich et al., 2007). This interaction is mediated by the TPR domain of FKBP38 and the C90 domain of Hsp90 (Edlich et al., 2007). However, it leads to the inhibition of the FKBP activity of FKBP38, probably as a consequence of steric hindrance between Hsp90 and the ligands of the FKBP domain.

Finally, an interaction of the hepatitis C non-structural protein NS5A with FKBP38, which leads to the prevention of apoptosis, was recently reported (Wang et al., 2006). A Bcl-2 homology (BH) domain present in NS5A was identified as the one responsible for the interaction with FKBP38.

1.1.3. Three-dimensional structures of FKBPs

1.1.3.1. The prototypic FKBP12

Human FKBP12 (FKBP12; gene name FKBP1A) is the best characterized member of the FKBP enzyme family. This protein represents the minimal amino acid sequence displaying PPIase activity and FK506 binding, and is therefore considered as the prototypic FKBP domain. It folds to a "half β-barrel" that consists of a five-stranded antiparallel β-sheet (with a +3, +1, -3, +1 topology) which wraps around a central α-helix and encloses the active site (Figure 3A). Several three-dimensional structures of this protein and its complexes with FK506, rapamycin and other low-molecular-weight ligands have been solved by means of NMR and X-ray crystallography

(Michnick et al., 1991; Van Duyne et al., 1991a,b; Van Duyne et al., 1993; Wilson et al., 1995; Sich et al., 2000). On the other hand, no structure of an FKBP12 complex with a peptide substrate has been solved up to date.

A **B**

Figure 3. Comparison of the three-dimensional structures of (**A**) FKBP12 and (**B**) the FKBP12/FK506 complex. The FK506 molecule is represented as stick model and colored according to atom type.

No major structural changes arise in FKBP12 upon FK506 binding. In the FKBP12/FK506 complex (Figure 3B), the FK506 molecule binds in a hydrophobic cavity located between the interior side of the β-sheet and the α-helix, flanked by the loops β2-β3 and β5-α1 as well as the bulge disrupting β5. A total of fourteen residues (Tyr26, Phe36, Asp37, Arg42, Phe46, Glu54, Val55, Ile56, Trp59, Ala81, Tyr82, His87, Ile91 and Phe99), many of them highly hydrophobic, show direct contacts (less than 4 Å) with the macrolide (Figure 4A). Hydrogen bonds between FK506 and the residues Asp37, Glu54, Ile56 and Tyr82 provide additional stabilization to the drug/enzyme complex.

Of special interest is the presence of a predominantly aromatic "cage", formed by the side-chains of residues Tyr26, Phe46, Val55, Trp59 and Phe99, at the site where the pipecolinyl moiety of FK506 rests (Figure 4B). This cavity is also the binding site for the five-membered pyrrolidyl ring of 3-(3-pyridyl)-1-propyl(2S)-1-(3,3-dimethyl-1,2-dioxopentyl)-2-pyrrolidinecarboxylate (GPI1046) in the solution structure of the FKBP12/GPI1046 complex (Sich et al., 2000), and has been therefore assumed as the binding site for the prolyl moieties of FKBP12 substrates. Other features of the FKBP12/FK506 structure are (i) that the pipecolinyl-C8 carbonyl bond exhibits a *trans* conformation that does not resemble a twisted amide bond as had been proposed (Rosen et al., 1990) before the complex structure was solved, and (ii) the orientation of the methyl group C35 of the hemiacetal ring towards a hydrophobic cavity formed by the side-chains of residues Phe36, Tyr82, His87, Ile90 and Ile91, which may provide an explanation for the higher catalytic efficiency of this protein in substrates with large hydrophobic residues (i.e. leucine or phenylalanine) in the position before the proline.

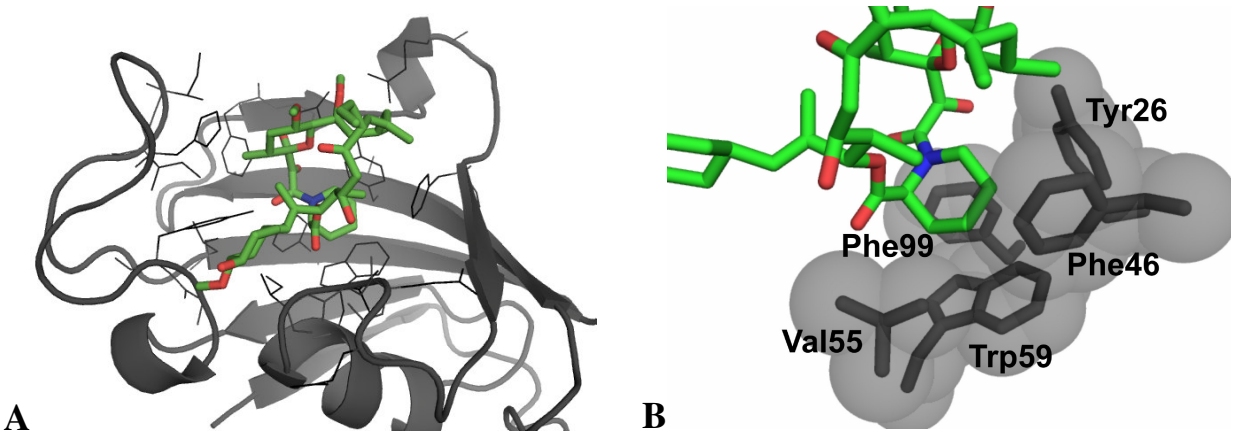

Figure 4. Graphic representations of the FKBP12/FK506 complex structure. (**A**) The FK506 molecule (represented as sticks colored by atom type) rests in a hydrophobic cavity located between the interior side of the β-sheet and the α-helix. The backbone of FKBP12 is represented as a gray ribbon and the side-chains of the protein residues interacting with the FK506 molecule as black lines. (**B**) Close-up of the pipecolinyl moiety of FK506 (sticks colored by atom type) and neighboring FKBP12 residues (gray sticks and spheres).

Although the structure of the FKBP12/FK506 complex provides some insight as to what might be the mechanism of catalysis in the FKBPs, certain experimental findings, such as the low degree of conservation of the amino acid residues interacting with the FK506 molecule (Fanghänel and Fischer, 2004) as well as differences between peptide substrates and FK506 in the fluorescence quenching of the Trp59 ring that is located at the bottom of the binding cavity, raise some doubt about the hypothesis that the FKBP12/FK506 structure mimics the FKBP12/substrate complex (Park et al., 1992).

1.1.3.2. FKBPs with TPR domains: FKBP51, FKBP52 and *At*FKBP42

The human FKBP51 (FKBP54, gene name FKBP5) and FKBP52 (FKBP56, FKBP59, p59, gene name FKBP4) are two very similar FKBPs containing TPR domains. Both present the same overall domain organization: two consecutive FKBP domains, followed by a TPR domain comprising three tetratricopeptide repeats (TPRs), each of which consists of two antiparallel α-helices (α1 to α6), plus an additional α-helix (α7) that contains the calmodulin-binding motif and is structurally associated to the TPR domain. FKBP51 and FKBP52 are both involved, when bound to Hsp90 via their TPR domains, in the formation of high affinity steroid receptor complexes (Pratt et al., 1999). In both proteins, only the first FKBP domain, i.e. the one most similar to FKBP12, exhibits PPIase activity (Barent et al., 1998). The three-dimensional structures of FKBP51 and FKBP52 have been solved recently by X-ray crystallography (Sinars et al., 2003; Wu et al., 2004).

The FKBP42 from *Arabidopsis thaliana* (*At*FKBP42) is another FKBP with a TPR domain of known three-dimensional structure. This protein presents a domain organization similar to that of FKBP51 and FKBP52, except for (i) the presence of only a single FKBP domain, which is inactive like the second domain of both human proteins, and (ii) the addition of a C-terminal membrane anchor. Its TPR domain interacts with *At*Hsp90, resembling the complex between the human proteins FKBP52 and Hsp90 (Kamphausen et al., 2002), while its FKBP domain can interact with the C-terminal nucleotide-binding domains (NBDs) of the plasma membrane-localized ATP-binding cassette (ABC) transporters *At*PGP1 and *At*PGP19 (Geisler et al., 2003). The crystal structures of (i) the FKBP domain (Weiergraber et al., 2005) and (ii) a construct comprising the FKBP and TPR domains (Granzin et al., 2006) of *At*FKBP42 were recently published.

The FKBP activity of the first FKBP domain of both FKBP51 and FKBP52 may be explained by their high degree of sequence similarity to FKBP12 (Figure 5A). In particular the residues involved in the interaction with the ligand FK506 are mostly conserved. The active sites of these domains are therefore structurally very similar to that of FKBP12 (Figure 5B).

On the other hand, the sequence of the FKBP domain of *At*FKBP42 displays some notable differences with respect to that of FKBP12 (Figure 5D). Especially, amino acid insertions in the loops β5-α1 and β2-β3 lead to significant differences between the hydrophobic cleft of *At*FKBP42 and the active site of FKBP12 (Figure 5C). The insertion of one residue in the loop β5-α1 produces a change in the topology of this loop, which partly protrudes into the binding pocket. More precisely, the segment Lys103-Leu106 would overlap with the FK506 molecule of the FKBP12/FK506 complex. Moreover, some hydrogen bonds between FK506 and residues in the β5-α1 loop of FKBP12 cannot be formed in *At*FKBP42. In addition, the insertion of two residues in the loop β2-β3 leads to an extension of this loop above the binding pocket. Consequently, the residues Phe140 and Pro141, while largely not overlapping with the FK506 molecule, close the entrance portal to the hydrophobic cleft of the FKBP domain of *At*FKBP42. All these differences may explain the lack of FKBP activity reported for the FKBP domain of *At*FKBP42 (Weiergraber et al., 2005).

The TPR domains of FKBP51, FKBP52 and *At*FKBP42 display very similar conformations (Figure 6A), as indicated by backbone root-mean-square deviations (RMSDs) of 1.17 Å, 1.04 Å and 0.53 Å (only considering the three TPR motifs) between the superposed structure pairs *At*FKBP42-FKBP51, *At*FKBP42-FKBP52 and FKBP51-FKBP52, respectively. The helix α7 of FKBP52, however, is shifted by more than 30º from the Hsp90 binding surface relative to

FKBP51. These different orientations of helix α7 have been attributed to the presence of Ile400 in the α7 helix of FKBP52 (instead of Ala398 in FKBP51), which would otherwise collide with the phenyl group of Phe369 (Wu et al., 2004).

```
FKBP52D1   DISPKQDEGVLKVIKREGTGTEMPMIGDRVFVH**Y**TGWLLDGTK**FD**SSLD**R**KDK**F**SFDLG
FKBP51D1   DITSKKDRGVLKIVKRVGNGEETPMIGDKVYVH**Y**KGKLSNGKK**FD**SSHD**R**NEP**F**VFSLG
FKBP12     --------GVQVETISPGDGRTFPKRGQTCVVH**Y**TGMLEDGKK**FD**SSRD**R**NKP**F**KFMLG

FKBP52D1   KG**EVI**KA**W**DIAIATMKVGEVCHITCKPEY**AY**GSAG**S**PPK**I**PPNATLV**F**EVELFEFK
FKBP51D1   KG**QVI**KA**W**DIGVATMKKGEICHLLCKPEY**AY**GSAG**S**LPK**I**PSNATLF**F**EIELLDFK
FKBP12     KQ**EVI**RG**W**EEGVAQMSVGQRAKLTISPDY**AY**GATG**H**PGI**I**PPHATLV**F**DVELLKLE
```

A

B

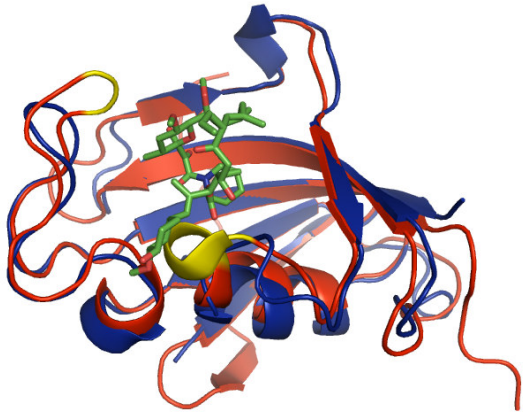

C

```
FKBP42D    KVSKQIIKEGHGSK-PSKYSTCFLHYRAWTKNSQHKFEDTWHEQQPIELVLGK**EKKEL**AG
FKBP12     GVQVETISPGDGRTFPKRGQTCVVHYTGMLEDGK-KFDSSRDRNKPFKFMLGKQ-EVIRG

FKBP42D    LAIGVASMKSGERALVHVGWELAYGKEGNFSF**PN**VPPMADLLYEVEVIGFD
FKBP12     WEEGVAQMSVGQRAKLTISPDYAYGATGHPGI--IPPHATLVFDVELLKLE
```

D

Figure 5. (**A**) Sequence alignment of the first FKBP domain of both FKBP52 and FKBP51 with FKBP12. The residues involved in the interaction with FK506 in the FKBP12/FK506 complex are highlighted in bold. (**B**) Superposition of the first FKBP domain of FKBP52 (red) with FKBP12 (blue). The side-chains of residues interacting with FK506 are shown as lines. (**C**) Superposition of the FKBP domain of *At*FKBP42 (red) with the FKBP12/FK506 complex (blue). The FK506 molecule is represented as stick model colored by atom type. Parts of the loops β2-β3 and β5-α1, which were identified as responsible for the lack of FKBP activity of *At*FKBP42, are highlighted in yellow. (D) Sequence alignment of the FKBP domain of *At*FKBP42 with FKBP12. The segment Glu102-Leu106 in the loop β5-α1, and the insertion Pro141-Asn142 in the loop β2-β3 of *At*FKBP42 are highlighted in bold.

In all three structures the TPR domain adopts a different orientation relative to the preceding FKBP domain (Figure 6B). These arrangements are partially stabilized by polar and hydrophobic interactions. These interactions, however, are likely to occur as a result of crystal packing (Wu et al., 2004; Granzin et al., 2006), considering that the FKBP and TPR domains have been

implicated in a variety of biological processes involving numerous interaction partners that may not be compatible with a fixed domain arrangement.

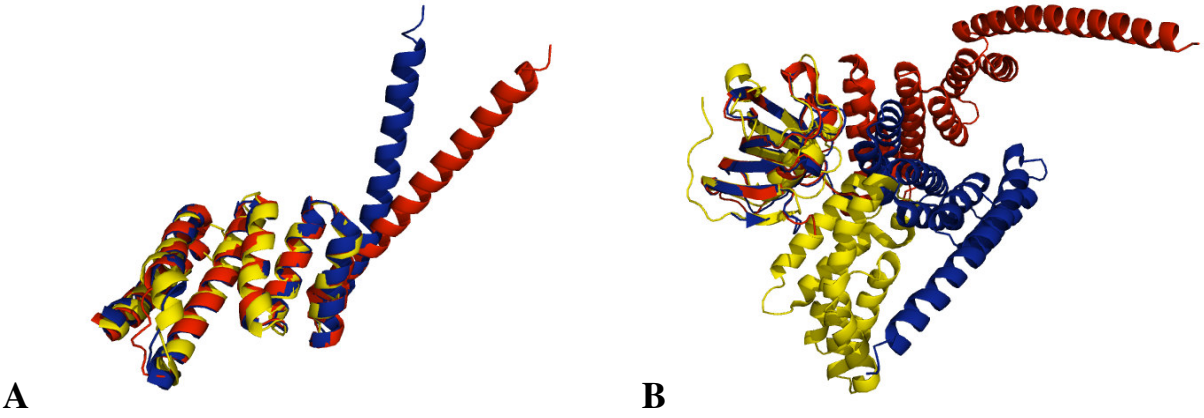

Figure 6. Superpositions of different regions of the FKBP51, FKBP52 and *At*FKBP42 structures. (**A**) The TPR domains of FKBP51 (blue), FKBP52 (red) and *At*FKBP42 (yellow) are superposed, with the exception of the helix α7. (**B**) The second FKBP domain of both, FKBP51 (blue) and FKBP52 (red), as well as the FKBP domain of *At*FKBP42 (yellow) are superposed, while the TPR domains display different orientations.

1.2. Calcium and calcium-binding proteins

The calcium ion (Ca^{2+}) is essential for the physiology of higher organisms, as it is involved in the regulation of diverse cellular processes such as cell proliferation, development, motility, secretion, muscle contraction, as well as in learning and memory (Carafoli, 2002; Berridge et al., 2000; Evenas et al., 1998). In many organisms, the majority of Ca^{2+} occurs as calcium phosphate in the exo- or endoskeletons, which serve as structural scaffolds and also buffer the Ca^{2+} levels within extracellular fluids at 10^{-3} M. The resting concentration of intracellular free Ca^{2+} (~10^{-7} M) is 10^{4} times lower than that outside the cells, providing the potential for its import into the cells, where it acts as a universal second messenger.

The intracellular concentration of Ca^{2+} can be affected by a variety of processes. Thus, various stimuli, such as changes in membrane polarization or the binding of small ligands to membrane receptors, can lead to the influx into the cytosol of either extracellular Ca^{2+} ions via plasma-membrane Ca^{2+} channels or Ca^{2+} ions from intracellular organelles, producing an up to 100-fold increase in the cytosolic Ca^{2+} concentration (Bootman et al., 2001). As soon as the concentration of Ca^{2+} ions increases, the combined action of Ca^{2+}-binding proteins, Ca^{2+} pumps and Na^{+}/Ca^{2+} exchangers sequesters these additional ions either to intracellular storage sites or outside the cell. A complex network of regulatory mechanisms affects the actions of the key proteins involved in the transport of Ca^{2+} ions, leading to oscillations of defined amplitude, frequency and location in

the Ca^{2+} concentration (Berridge, 1990; Meyer and Stryer, 1991). This transient behavior of the intracellular Ca^{2+} concentration itself can activate or regulate a variety of cellular processes, depending on its entry route into the cell, local site of action and pattern of modulation (Berridge et al., 1998; Berridge et al., 2000; Carafoli et al., 2001).

The information encoded in transient intracellular Ca^{2+} signals is deciphered by a number of Ca^{2+}-binding proteins, which convert these signals into a variety of biochemical and cellular changes. Several hundred of these proteins have been identified, most of them sharing a common Ca^{2+}-binding motif: the EF-hand (Ikura, 1996; Nelson and Chazin, 1998; Lewit-Bentley and Rety, 2000). This motif consists of about 30 amino acids organized in a helix-loop-helix topology, where the two helices are arranged similar to the extended thumb and index finger of a hand. In most Ca^{2+}-binding proteins, two EF-hand motifs are forming an EF-hand pair, which consists of a twisted four-helix bundle (Kretsinger, 1996; Chazin, 1995). Two different modes of response to the Ca^{2+} signal are known for these proteins. One group acts as Ca^{2+} buffers or transporters, like parvalbumin and calbindin, and does not show significant conformational changes upon Ca^{2+} binding. The other group, the so-called Ca^{2+} sensors, undergo a Ca^{2+}-induced conformational change (Ikura, 1996; Yap et al., 1999), allowing these proteins to act as Ca^{2+} switches that - once they are activated - regulate downstream effectors (Braunewell, 2005; Chin and Means, 2000; Carafoli et al., 2001).

1.2.1. Calmodulin

Calmodulin (CaM) is the prototypic Ca^{2+} sensor and has been studied extensively. It is a relatively small protein (148 amino acids and 16.8 kDa in vertebrates) that is highly conserved, water soluble and omnipresent in the cytosol of all eukaryotic cells, where it participates in signalling pathways that regulate many crucial cellular processes such as growth, proliferation and movement (Cohen and Klee, 1988; Eldik and Waterson, 1998). It constitutes at least 0.1% of the total protein content in the cell (10^{-6} to 10^{-5} M) and can be expressed at higher levels in rapidly growing cells, especially in those undergoing division and cell differentiation (Chin and Means, 2000). The importance of this protein for mammalian cell survival is also reflected by the presence of multiple CaM genes (e.g. three in both humans and rodents) at separate chromosomes (Toutenhoofd and Strehler, 2000)

CaM comprises four EF-hand motifs. The first two are combined to form a globular N-terminal domain, separated by a short flexible linker from a highly homologous (48% sequence identity and 75% sequence homology) C-terminal domain, which also contains two EF-hand motifs. Its

Ca^{2+} affinities (K_D ~ 5 x 10^{-7} M for the C-terminal domain and ~ 5 x 10^{-6} M for the N-terminal domain) (Gilli et al., 1998; Potter et al., 1983; Ogawa et al., 1984) fall within the range of Ca^{2+} concentrations exhibited by most cells (10^{-7} M to 10^{-5} M), thus allowing this protein to act as an intrinsic Ca^{2+} sensor. Moreover, the difference of about one order of magnitude in the Ca^{2+} affinities between the CaM C- and N-terminal domains provides an additional capability to discriminate the Ca^{2+} signals.

The structures of apo- and holo-calmodulin have been studied extensively by NMR spectroscopy and X-ray crystallography. Consequently, several structures of apo-CaM (Kuboniwa et al., 1995; Finn et al., 1995; Zhang et al., 1995) and holo-CaM (Babu et al., 1985; Babu et al., 1988; Chattopadhyaya et al., 1992; Chou et al., 2001) have been published, providing a deep insight into the biological properties of this protein.

Both apo- and holo-CaM fold into two small, highly similar globular domains connected by a central linker (Figure 7). In holo-CaM, this linker was found to be α-helical in the crystalline state (Babu et al., 1985). NMR relaxation studies that were carried out with both CaM forms, however, demonstrated that this central linker is non-helical and highly flexible in solution (Barbato et al., 1992; Tjandra et al., 1995). Consequently, the N- and C-terminal domains of CaM do not adopt a defined orientation relative to each other in solution. This property is fundamental for the activity of CaM, as it allows its two domains to adopt different relative orientations in order to interact with diverse binding partners.

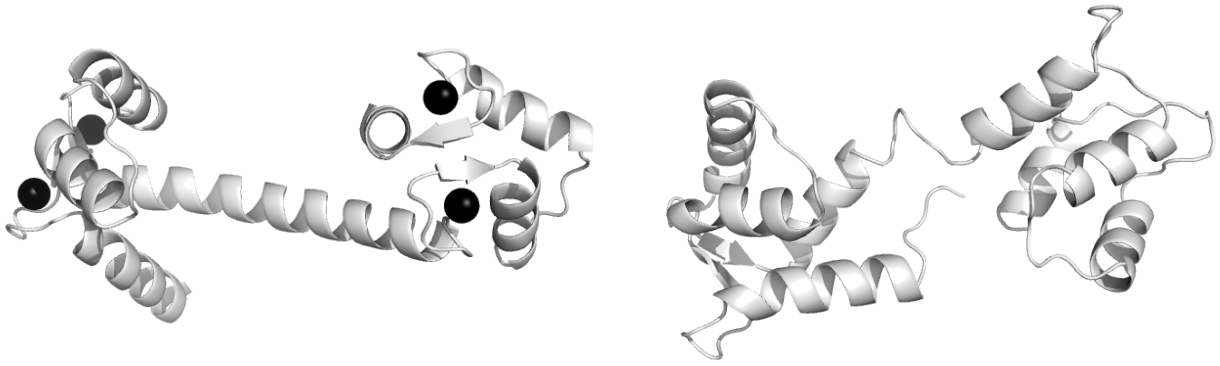

Figure 7. Overall structures of holo- (**left**) and apo-CaM (**right**). The Ca^{2+} ions in holo-CaM are shown as black spheres.

Each CaM domain contains two helix-loop-helix EF-hand motifs, linked by a short and slightly distorted two-stranded antiparallel β-sheet. The four helices of each CaM domain (i.e. A, B, C and D in the N-terminal as well as E, F, G and H in the C-terminal domain) adopt different relative orientations in apo- and holo-CaM (Figure 8A). Thus, in apo-CaM they are tightly packed, adopting nearly antiparallel orientations as indicated by the relative angles between the

helix pairs A-B (138º), C-D (130º), E-F (131º) and G-H (133º) (Figure 8B). Upon Ca^{2+} binding these helices rearrange, adopting perpendicular orientations in holo-CaM as indicated by the interhelical angles A-B (87º), C-D (113º), E-F (84º) and G-H (96º). This gives rise to methionine-rich, highly hydrophobic clefts in holo-CaM (Figure 8C and D), which are responsible for the binding of numerous target proteins. Moreover, the high flexibility and polarizability of methionine side-chains (Gellman, 1991) confers holo-CaM an additional ability to adapt to different target molecules (Zhang et al., 1994; Zhang and Vogel, 1994).

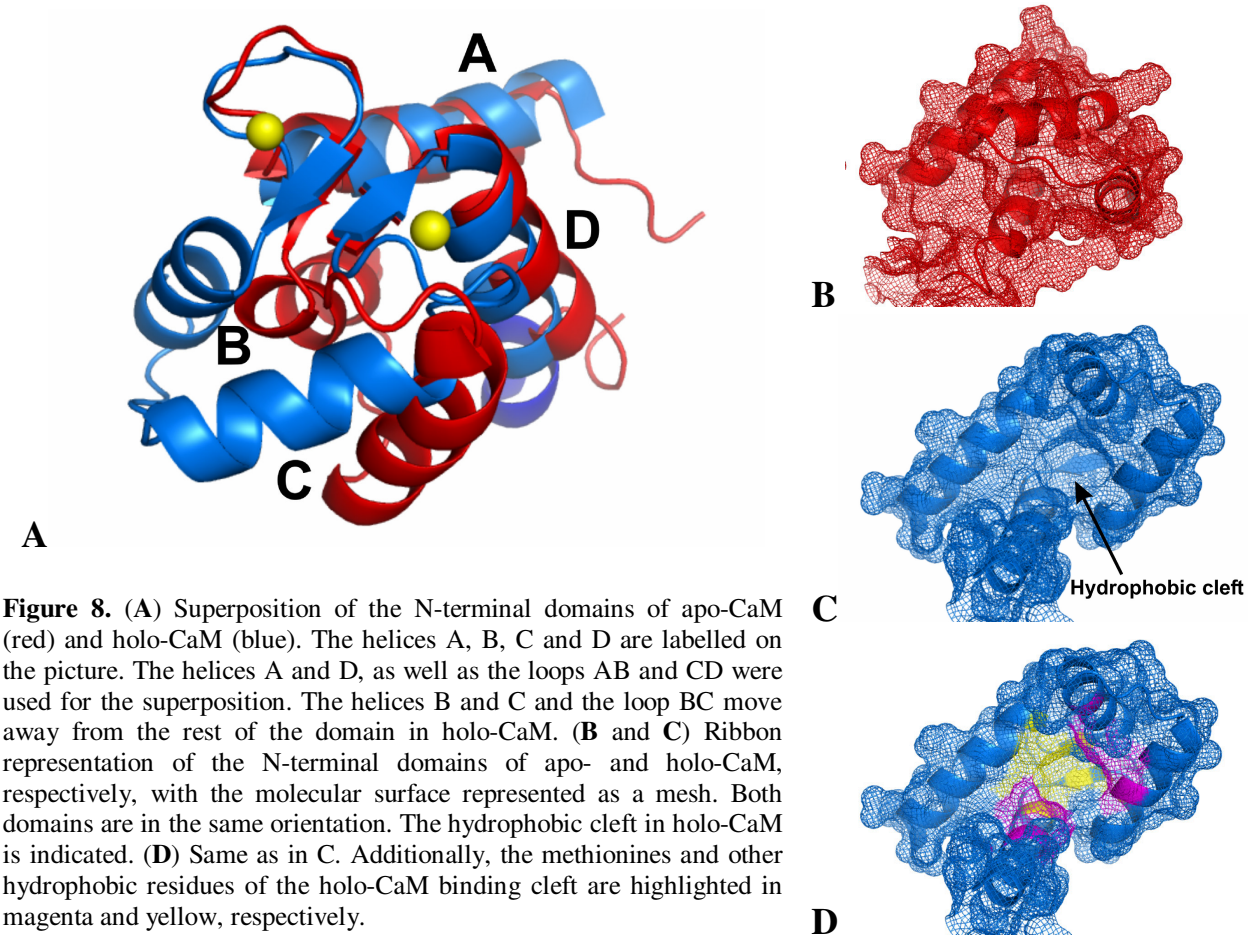

Figure 8. (**A**) Superposition of the N-terminal domains of apo-CaM (red) and holo-CaM (blue). The helices A, B, C and D are labelled on the picture. The helices A and D, as well as the loops AB and CD were used for the superposition. The helices B and C and the loop BC move away from the rest of the domain in holo-CaM. (**B** and **C**) Ribbon representation of the N-terminal domains of apo- and holo-CaM, respectively, with the molecular surface represented as a mesh. Both domains are in the same orientation. The hydrophobic cleft in holo-CaM is indicated. (**D**) Same as in C. Additionally, the methionines and other hydrophobic residues of the holo-CaM binding cleft are highlighted in magenta and yellow, respectively.

1.2.2. Calmodulin binding to target proteins

Calmodulin interacts in cells with a large number of target proteins, which are involved in a variety of cellular processes as diverse as muscle contraction, gene regulation, fertilization, cell proliferation, vesicular fusion and apoptosis (Cohen and Klee, 1988; Eldik and Waterson, 1998). Both, apo- and holo-CaM are able to interact with a large body of proteins (Jurado et al., 1999; Yamniuk and Vogel, 2004; Vetter and Leclerc, 2003). Most of these interactions lead to the activation of the target proteins, whereas others can modulate the action of CaM, for example

regulating its cellular localization (Chin and Means, 2000). Several consensus sequences mediating these interactions have been identified in CaM target proteins (Rhoads and Friedberg, 1997).

The most frequent CaM-binding domains are relatively short polypeptide chains of about 15-30 residues, which do not share a high homology but all have in common the tendency to form a basic, amphiphilic α-helix (Crivici and Ikura, 1995; Rhoads and Friedberg, 1997). They often partially overlap with autoinhibitory domains, as for example in CaM kinase kinase (CaMKK). Furthermore, many of them are close to regulatory phosphorylation sites (e.g. CaM kinase II) or to protein-protein or protein-membrane interaction domains (e.g. MARCKS protein) (Ishida and Vogel, 2006).

Among these numerous target proteins, the family of CaM-dependent serine/threonine kinases is the one best characterized with respect to their structural and functional CaM interaction mechanisms. These proteins are autoinhibited in the absence of Ca^{2+} and CaM, but they become active upon holo-CaM binding to their CaM-binding domains, which removes the autoinhibitory domain from the catalytic site of these enzymes. This activation mechanism also applies to a variety of other enzymes, such as the cerebellar nitric oxide synthase and the plasma membrane Ca^{2+} pump.

The interaction of holo-CaM with all these CaM-binding domains takes place in a similar manner, as revealed by several NMR and X-ray structures of holo-CaM with peptides corresponding to CaM-binding domains (Vetter and Leclerc, 2003; Yamniuk and Vogel, 2004; Ishida and Vogel, 2006). A common feature of all these peptides, in addition to the formation of a basic, amphiphilic α-helix when bound to holo-CaM, is the presence of regularly spaced hydrophobic residues (i.e. Trp, Phe, Ile, Leu or Val), which act as anchors to the hydrophobic cleft of the holo-CaM domains. Most of these peptides fall into one of three groups of CaM-target sequences (i.e. 1-10, 1-14 and 1-16) which are distinguished by the spacing of the two outer hydrophobic residues. The presence of additional hydrophobic amino acids in the middle of these sequences led to the definition of subgroups of CaM-binding motifs (i.e. 1-8-14, 1-5-8-14 and 1-5-10) (Rhoads and Friedberg, 1997). It is important to note, however, that many protein sequences that show no homology to these motifs can also bind CaM.

The typical features of most of the holo-CaM/target-peptide complexes are nicely exemplified in the structure of holo-CaM in complex with the CaM-binding domain from smooth muscle myosin light chain kinase (smMLCK) (Meador et al., 1992), which presents a 1-8-14 CaM-

binding motif. In this structure, the N- and C-terminal domains of CaM wrap around a helical peptide to form a globular complex (Figure 9A). The hydrophobic side-chains of Trp800 and Leu813 serve to anchor the N- and C-terminal ends of the peptide in an antiparallel arrangement to the C- and N-terminal domains of CaM, respectively. The predominantly hydrophobic interactions are further stabilized by salt-bridge formation between acidic side-chains from CaM and basic peptide residues. Interestingly, the conformation of the individual CaM domains remains almost unaffected by the complex formation, as revealed by the essentially unchanged backbone structure of both CaM domains.

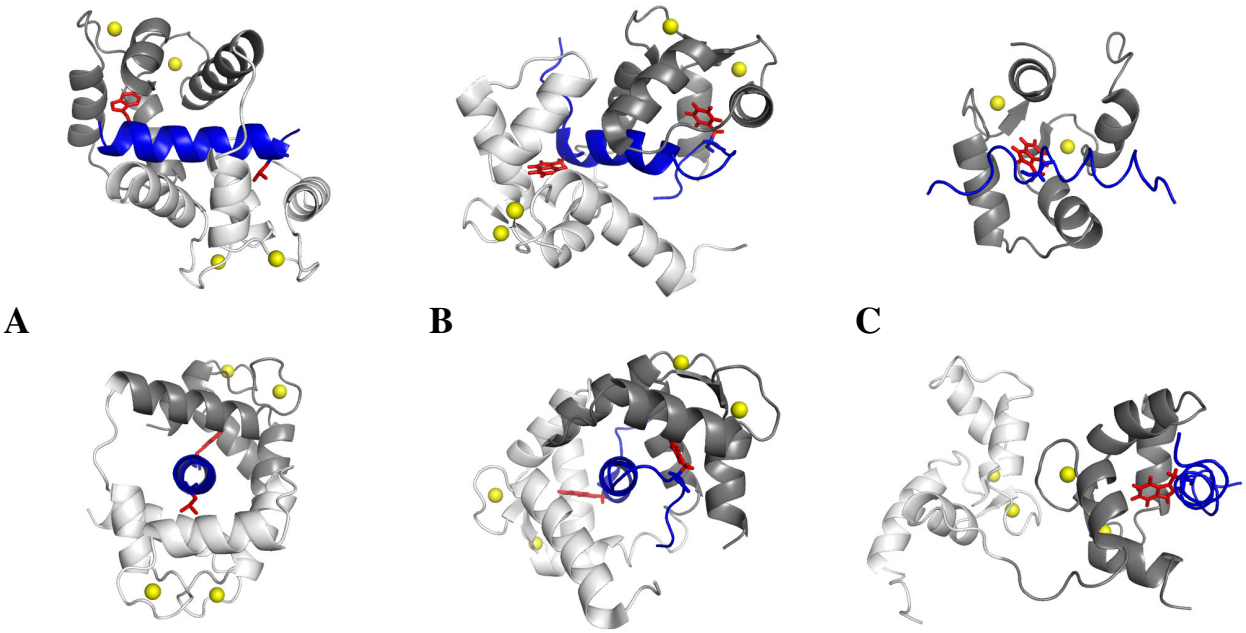

Figure 9. Comparison of the structures of holo-CaM in complex with peptides derived from the CaM-binding domains of (A) smMLCK (PDB ID code 1CDL) (B) CaMKK (PDB ID code 1CKK) and (C) a truncated CaM-binding domain (C20W) from the plasma membrane Ca^{2+} pump (PDB ID code 1CFF). The N-terminal and C-terminal domains of CaM are shown in white and gray, respectively, while the Ca^{2+} atoms are shown as yellow spheres. The CaM-binding domains are represented in blue and the hydrophobic anchors (Trp800 and Leu813 in A, Trp444 and Phe459 in B, and Trp8 in C) as red stick models. In the upper panel, the CaM-binding domains are oriented with the N-terminus on the left side, while in the lower panels the C-terminus is in front.

Significant alterations from this structure are displayed by the complexes with peptides from the auto-inhibitory domains of CaM-dependent kinase kinase (CaMKK) (Osawa et al., 1999) and the plasma membrane Ca^{2+} pump (C20W peptide) (Elshort et al., 1999). Thus, the peptide from CaMKK (Figure 9B) it is (i) bound in an "inverted" parallel orientation and (ii) only partially helical, forming an additional β-hairpin like loop, whereas the peptide from the plasma membrane Ca^{2+} pump is only bound to the C-terminal CaM domain (Figure 9C). These structures indicate the existence of a high degree of variability in the CaM-target peptide binding modes.

New activation mechanisms of CaM-target proteins have been revealed by the elucidation of the crystal structures of CaM in complex with the exotoxin edema factor from *Bacillus anthracis* (Drum et al., 2002) and a fragment from the Ca^{2+}-activated K^+ channel (Schumacher et al., 2001). These structures differ drastically from the CaM complexes with small peptides, thus providing more insight in the interactions of CaM with its target molecules.

The small conductance Ca^{2+}-activated K^+ channel (SK channel) consists of four membrane-spanning α-subunits and is gated by the intracellular Ca^{2+} concentration (Xia et al., 1998). The C-terminal cytosolic region of each α-subunit features one CaM molecule bound constitutively via a domain that shares no similarities with other CaM-binding domains and is not Ca^{2+} dependent. The structure of CaM in complex with a 96-residue fragment corresponding to this C-terminal cytosolic portion of the K^+-channel (Figure 10A) was the first solved structure of CaM bound to a large protein fragment and thus provides interesting insight into the Ca^{2+}-mediated activation of this channel. The CaM-binding domain of the K^+-channel consists of two long antiparallel α-helices, α1 (residues 413-440) and α2 (residues 446-489), connected by a short loop (residues 441-445). Its complex with CaM is a symmetric tetramer, consistent of two molecules of each protein. The central part of the structure is a dimer of two CaM-binding domains that are connected via a side-by-side antiparallel interaction of their helices α2 and α2'. Two CaM molecules are bound each to one edge of the central dimer, interacting simultaneously with three helices of the dimer (i.e. α1, α2 and α2') and covering over 80% of the dimer surface area. Consequently, CaM adopts an almost extended conformation. Remarkably, the C-terminal domain of CaM, which is bound to the helix α1, is free of Ca^{2+} and adopts the semi-open conformation, probably resembling the Ca^{2+}-independent interaction of CaM with IQ-motifs, whereas the N-terminal CaM domain is Ca^{2+} bound and displays an open conformation, binding helix α2' from the second CaM-binding site in a similar manner as in most of the CaM/peptide complexes. The regulation of the SK channel by Ca^{2+} and CaM can be summarized as follows: one CaM molecule is bound constitutively via its C-terminal domain to helix α1 of the cytosolic domain of each SK channel α-subunit. Once the Ca^{2+} concentration increases, the Ca^{2+}-bound N-terminal CaM domain induces the dimerization of the cytosolic domains of two α-subunits, which causes the SK channel to open.

The structure of the CaM complex with the C-terminal fragment (residues 191-280) of the exotoxin edema factor from *Bacillus anthracis* (Figure 10B) is the first example where CaM was successfully crystallized together with a catalytically functional target. Moreover, comparison of the structures with and without CaM, as well as with the substrate analogue 3'-dATP, provided detailed information about the activation mechanism. The edema factor is a soluble adenylyl

cyclase that consists of three globular domains, referred to as CA, CB and helical domain, and three smaller parts (switch-A, -B and -C), which undergo large conformational changes in response to CaM binding. In the complex, CaM displays an extended conformation and is inserted between the CA and helical domains, separating the helical domain from the main structure. The C-terminal CaM domain is Ca^{2+}-bound and adopts an open conformation, thus binding the helical switch-A, which is close to the CA domain of the edema factor. On the other hand, the tight interaction of the helices A and B from the N-terminal CaM domain with the CB domain of the edema factor prevents the rearrangement of these helices, which is required for Ca^{2+}-binding. Thus, the N-terminal CaM domain remains free of Ca^{2+}, displaying a closed conformation similar to that of apo-CaM, which is remarkable considering that the complex was crystallized under excess of Ca^{2+}. The structural rearrangements produced by CaM binding lead to the formation of the active site in a region that is solvent exposed in the CaM-free state. This activation mechanism has therefore been referred to as "active-site remodeling" (Hoeflich and Ikura, 2002).

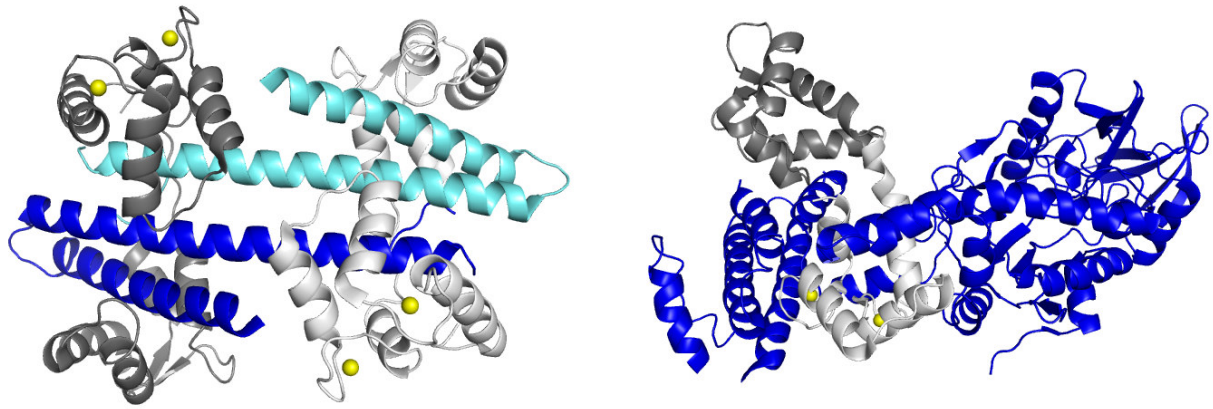

Figure 10. Structures of CaM in complex with (**A**) rat Ca^{2+}-activated K^+ channel (PDB ID code 1G4Y) and (**B**) anthrax adenylyl cyclase (PDB ID code 1K93). In (A), the two CaM molecules are represented in white or gray and the two peptide molecules from the Ca^{2+}-activated K^+ channel in blue or cyan. In (B), the N- and C-terminal domains of CaM are shown in white and gray, respectively, while the anthrax adenylyl cyclase is shown in blue. Ca^{2+} ions, bound to the N-terminal domain of CaM in (A) and to the C-terminal domain of CaM in (B), are shown as yellow spheres.

1.3. Objectives

The human FKBP38 displays a unique property among PPIases, as its FKBP activity is regulated by calmodulin in combination with Ca^{2+}. Moreover, it has been demonstrated that this protein plays an important role in apoptotic pathways. Therefore, the structural characterization of FKBP38, especially of its catalytic domain, as well as the study of the interactions between FKBP38 and CaM, are research topics of particular interest.

The first objective of this thesis is the structural elucidation of the catalytic domain of FKBP38 using high-resolution NMR spectroscopy. No previous work had been done in this direction. Therefore, all the usual stages of structure determination by NMR must be performed: (i) protein cloning, expression and purification, (ii) protein isotope labelling, (iii) complete resonance assignment and, (iv) structure calculation and refinement.

The second objective of this work is the characterization of the interactions between FKBP38 and CaM. NMR chemical shift perturbation mapping has been selected as the method of choice to study these relatively weak interactions. As chemical shift assignments of the two CaM forms under the experimental conditions used in this study have not been previously reported, the first goal is to achieve the backbone amide resonance assignment of both apo- and holo-CaM under these conditions. Next, the NMR chemical shift perturbations study of the interactions of apo- and holo-CaM with the FKBP domain of FKBP38 should be carry out. In addition, the interactions of holo-CaM with the putative CaM-binding-site of FKBP38 should be examined by the same procedure. The information obtained from these chemical shift perturbation measurements can then be used to elucidate the structures of the corresponding complexes. This ought to provide some insight into the activation of FKBP38 by CaM. Furthermore, a model of the overall complex between FKBP38 and CaM shall be derived.

2. Materials and Methods

2.1. Materials

2.1.1. Chemicals and materials

All chemicals used had at least the purity grade “pro analysii”.

Chemical	Distributer
Acetic acid	Merck (Darmstadt)
Agar	AppliChem (Darmstadt)
Agarose	Roth (Karlsruhe)
Ammonium sulfate	Merck (Darmstadt)
5-Bromo-4-chloro-3-indolyl-β-D-galactoside	Roth (Karlsruhe)
Bromophenolblue	Serva (Heidelberg)
Calcium chloride	Merck (Darmstadt)
Chloramphenicol	Sigma (Deisenhofen)
Coomassie Brilliant Blue	Serva (Heidelberg)
Crystal Screen™	Hampton Research Corp. (Aliso Viejo, USA)
Crystal Screen 2™	Hampton Research Corp. (Aliso Viejo, USA)
Deuterium oxide (99.9%)	VEB Berlin Chemie (Berlin)
2,2-Dimethyl-2-silapentane-5-sulfonate	Cambridge Isotope Laboratories (Andover, USA)
dNTP	PeqLab (Erlangen)
EDTA	Roth (Karlsruhe)
EGTA	Sigma (Deisenhofen)
Ethanol	Fluka (Neu Ulm)
Ethidium bromide	Roth (Karlsruhe)
Glycerol	Roth (Karlsruhe)
Glycine	Fluka (Neu Ulm)
HEPES	AppliChem (Darmstadt)
Hydrochloric acid	Merck (Darmstadt)
IPTG	AppliChem (Darmstadt)
JBScreen Classic 1-4	Jena Bioscience (Jena)

Kanamycin	AppliChem (Darmstadt)
Magnesium chloride	Merck (Darmstadt)
Magnesium sulfate	Invitrogen (Karlsruhe)
MES	Serva (Heidelberg)
^{15}N-enriched "rich growth OD2" medium	Silantes (München)
PEG4000	Serva (Heidelberg)
Peptone	Fluka (Buchs, Switzerland)
Phosphoric acid	Laborchemie Apolda (Apolda)
Potassium chloride	Merck (Darmstadt)
Regenerated cellulose tubular membrane	Roth (Karlsruhe)
SDS	Serva (Heidelberg)
Sodium azide	Merck (Darmstadt)
Sodium chloride	Merck (Darmstadt)
Sodium hydroxide	Merck (Darmstadt)
Tetracycline	Sigma (Deisenhofen)
TRIS	Serva (Heidelberg)
Vivaspin® (5 kDa cut-off)	Sartorius (Göttingen)
Yeast extract	Serva (Heidelberg)

2.1.2. Enzymes

Restriction endonucleases	New England Biolabs (Beverly, USA)
Pfx DNA-polymerase	Invitrogen (Karlsruhe)
Taq DNA-polymerase	New England Biolabs (Beverly, USA)
T4 DNA-ligase	New England Biolabs (Beverly, USA)

2.1.3. Plasmids and templates

pSTBlue-1	Novagen (Madison, USA)
pET28a	Novagen (Madison, USA)
Template for FKBP38	Provided by Dr. Frank Edlich (MPG, Halle)

2.1.4. PCR primers

FKBP38$^{35\text{-}153}$-5'	5'-GACTTCATGAGAAGAGTGGCTGGACATTCTG-3'
FKBP38$^{35\text{-}153}$-3'	5'-GACTAAGCTTTCACTCCAGGTCAGGCCCG -3'

2.1.5. *Escherichia coli* cells

BL21(DE3) Rosetta	Novagen (Madison, USA)
DH5α	Invitrogen (Karlsruhe)

2.1.6. Proteins and peptides

Calmodulin	Provided by Dr. Frank Edlich (MPG, Halle)
^{15}N-labelled Calmodulin	Provided by Dr. Frank Edlich (MPG, Halle)
C-terminal Calmodulin	Provided by Dr. Frank Edlich (MPG, Halle)
FKBP38$^{290\text{-}313}$	Provided by Dr. Günther Jahreis (MPG, Halle)
Partially ^{15}N-labelled FKBP38$^{290\text{-}313}$	Provided by Dr. Günther Jahreis (MPG, Halle)

2.1.7. Chromatography columns

Fractogel EMD-DEAE-650(M)	Merck (Whitehouse Station, USA)
HiLoad 16/60 Superdex 200 pg column	GE Healthcare (Waukesha, USA)

2.1.8. Standards

100 bp DNA standard	New England Biolabs (Beverly, USA)
1 kb DNA standard	New England Biolabs (Beverly, USA)
10 kDa protein standard	Fermentas (St. Leon-Rot)

2.1.9. Kits

High Pure® PCR product purification	Roche Diagnostics (Mannheim)
Perfectly Blunt cloning kit	Novagen (Madison, USA)
QIAquick® Gel extraction kit	Qiagen (Hilde)
QIAprep® Spin miniprep kit	Qiagen (Hilde)

The kits were used according to the recommendations of the manufacturers.

2.1.10. Buffers, media and stock solutions

Application buffer for agarose gel: 1x TAE buffer, 20% glycerol, 5 mM bromophenol blue.
SDS-PAGE buffer: 25 mM TRIS/HCl (pH 8.8), 150 mM glycine, 0.01% (w/v) SDS.
50 x TAE buffer (1l): 40 mM TRIS/HCl (pH 8.0), 57.1 ml acetic acid, 0.05 M EDTA, H_2O.

LB medium: 10 g/l peptone, 5 g/l yeast extract, 5 g/l NaCl (pH 7.5).

Stock solutions (all stored at -20 ºC and applied in a volume ratio 1:1000):

IPTG: 238 mg/ml (1 M) in H_2O
Chloramphenicol: 34 mg/ml in ethanol
Kanamycin: 50 mg/ml in H_2O
Tetracyclin: 5 mg/ml in ethanol (applied in a volume ratio 1:500)

2.1.11. Equipment

Avance-700 NMR spectrometer	Bruker (Rheinstetten)
Chromatography system	Amersham Pharmacia (Uppsala, Sweden)
DRX500 NMR spectrometer	Bruker (Rheinstetten)
Electrophoresis and blot apparatus	Biometra (Göttingen)
French® Press	SLM Aminco (Rochester, USA)
GeneQuant II spectrophotometer	Amersham Pharmacia (Uppsala, Sweden)
Heraeus Biofuge 22R centrifuge	Kendro (Hanau)
Heraeus Biofuge Stratos centrifuge	Kendro (Hanau)
HP-8453 diode array spectrophotometer	Hewlett Packard (Böblingen)
InoLab pH 720 pH-meter	WTW (Weilheim)
Optima® LE-80 K ultracentrifuge	Beckman Coulter (Krefeld)
PCR thermocycler	Biometra (Göttingen)
Sorval M120GX ultracentrifuge	Kendro (Hanau)

2.2. Methods

2.2.1. Molecular biology methods

2.2.1.1. Polymerase chain reaction

The polymerase chain reaction (PCR) technique (Mullis and Faloona 1987; Saiki et al. 1988) was used for the preparation and amplification of DNA for subcloning of recombinant human $FKBP38^{35\text{-}153}$.

The 5' PCR primer was designed with a splice site for the restriction endonuclease *Bsp*HI, and the 3' primer with a stop codon and a splice site for the restriction endonuclease *Hind*III.

Several PCR trials were made with two different DNA-polymerases (*Taq* and *Pfx*) as well as different concentrations of $MgSO_4$ and polymerase enhancer. The best results were obtained with the protocol shown in Table 1.

Table 1. Description of the PCR experiment displaying the best results.

PCR solution		PCR program
Pfx DNA-polymerase (1U/µl)	0.5 µl	1) 3 min 95 ºC
Pfx polymerase buffer (1U/µl)	5 µl	2) 20 sec 95 ºC
Primer 3' (100 pmol/µl)	0.5 µl	3) 30 sec 54 ºC 33 x
Primer 5' (100 pmol/µl)	0.5 µl	4) 1 min 72 ºC
DNA-template (150 µg/ml)	0.5 µl	5) 5 min 72 ºC
dNTP-mix (10 mM)	0.5 µl	
$MgSO_4$ (50 mM)	2 µl	
Distilled water	40.5 µl	

The DNA thus obtained was subsequently verified by agarose gel electrophoresis, restriction analysis and DNA sequencing.

2.2.1.2. Agarose gel electrophoresis

The amplified DNA from the PCR was applied, together with 1/10 volume of application buffer, to a 1% (w/v) agarose gel containing 0.5 µg ethidium bromide per ml of gel (Telford et al. 1977). The DNA was separated at 6-10 V/cm in 1 x TAE buffer. The DNA bands were detected with a UV lamp at 312 nm. Afterwards, the DNA was isolated with the *QIAquick*® kit.

2.2.1.3. DNA quantification

The DNA concentration was measured in 10 mm quartz cells with a GeneQuant II spectrophotometer working at 260 nm. An OD = 1.0 corresponds to 50 µg/ml of double-stranded DNA.

2.2.1.4. Enzymatic modification of DNA

The purified DNA product was subcloned into a pSTBlue-1 vector, digested with *Bsp*HI/*Hind*III, and then ligated into a pET28a vector.

Ligation: 50-200 ng of the DNA fragment, 5-fold excess of the vector DNA, 1 U of T4 DNA ligase (0.5 µl), and 1 µl of 10 x T4 buffer were incubated in a total volume of 10 µl at 25 ºC for 30 minutes. The blind end ligation was carried out with the *Perfectly Blunt cloning* kit.

DNA splicing: 0.5-10 µg of DNA, 1.5 U of each restriction enzyme (0.75 µl), and 1 µl of 10 x enzyme buffer were incubated in a total volume of 10 µl at 37 ºC for 3 hours.

2.2.1.5. Plasmid mini-preparation

5 ml of an overnight *E. coli* cell culture were centrifuged at 15.000 x g for 5 minutes. The resulting cell pellet was processed with the *QIAprep*® kit.

2.2.1.6. Transformation into competent *Escherichia coli* cells

0.1-20 µg of plasmid were added to 50 µl of competent cells. The cells were incubated in ice for 30 minutes, and afterwards submitted to a heat shock at 42 ºC for 45 seconds. Next, 300 µl of LB medium were added and the cells were incubated at 37 ºC for 1 hour. Finally, the entire cell solution was applied to an agar plate containing the adequate antibiotics for selection of the transformed cells and incubated overnight at 37 ºC.

2.2.1.7. Culturing of *Escherichia coli* cells

The *Escherichia coli* (*E. coli*) cells were grown in LB medium (containing the adequate antibiotics for selection) at 37 ºC and 220 rpm.

For the preparation of glycerol stocks, 700 µl of overnight cell culture were added to 300 µl of glycerol, frozen with liquid nitrogen, and stored at -80 ºC.

2.2.2. Preparative methods

2.2.2.1. Overexpression tests

500 µl of overnight cell culture and the required amount of antibiotic were added to 5 ml of LB medium in a test tube. The cells were grown for 3 hours at 37 ºC and 220 rpm before protein expression was induced with 50 µl of 0.1 M isopropyl-β-D-thiogalactoside (IPTG) and subsequent incubation for 4 hours under the same conditions. Afterwards, 1 ml of cell culture was centrifuged and the resulting bacterial pellet lysed by ultrasonication for 30 seconds in 25 mM TRIS buffer (pH 7.5). After centrifugation for 15 minutes at 15,000 x g, the protein content in the cell lysate was analyzed by SDS-PAGE.

2.2.2.2. Expression of recombinant FKBP38$^{35\text{-}153}$

Recombinant expression of FKBP38$^{35\text{-}153}$ in 6 l of LB medium at 37 °C was induced when OD_{600} was ~ 0.8 by adding IPTG to a final concentration of 1 mM and subsequent incubation for another 4 hours. Next, cells were harvested by centrifugation for 15 minutes at 4 °C and 5,000 × g.

For ^{15}N-labelling, the cells were grown and expressed in a fully ^{15}N-enriched "rich growth OD2" medium according to the recommendations of the supplier.

2.2.2.3. Lysis of *Escherichia coli* cells

The bacterial pellet from a 6 l culture was resuspended in 200 ml lysis buffer (10 mM MES pH 6.0, 150 mM NaCl) and cracked three times in a French® press at 10,000 PSI. The supernatant was centrifuged for 45 minutes at 4 °C and 100,000 × g.

2.2.2.4. Purification of FKBP38$^{35\text{-}153}$

The soluble cell lysate was applied to a Fractogel EMD DEAE-650 column, equilibrated with 10 mM MES buffer (pH 6.0, 150 mM NaCl). The protein was eluted from the DEAE-650 column with 1 M NaCl and the fractions were analyzed by sodium dodecylsulfate polyacrylamide gel electrophoresis (SDS-PAGE) as described in section 2.2.3.1. The fractions containing FKBP38$^{35\text{-}153}$ were dialyzed against 10 mM HEPES buffer (pH 7.8, 1.5 mM $MgCl_2$, 150 mM KCl) and loaded on a HiLoad 16/60 Superdex 200 pg column according to the recommendations of the supplier. The protein fractions were analyzed by SDS-PAGE. The purified FKBP38$^{35\text{-}153}$ was subsequently analyzed by MALDI-TOF mass spectrometry and N-terminal protein sequencing, thereby confirming the identity of the protein.

2.2.3. Analytical methods

2.2.3.1. SDS-PAGE

The proteins were separated according to size by means of SDS-PAGE. The discontinuous method of Laemmli (Laemmli, 1970) was applied for the separation in 15% (w/v) gels. The resolved protein bands were detected with Coomassie blue.

2.2.3.2. Protein quantification

The concentrations of purified proteins were determined by means of UV-VIS spectroscopy at 280 nm. The extinction coefficients for the Lambert-Beer equation were calculated according to the method of Gill and von Hippel (Gill and von Hippel, 1989) using the internet program ProtParam tool (www.expasy.ch).

2.2.3.3. Internet-based programs

The program *Webcutter*2.0 was used for the analysis of the splice sites for restriction endonucleases. The properties of the PCR primers were calculated and analyzed with the program *Oligonucleotide Properties Calculator*. The search for homologue protein sequences was carried out with the corresponding *BLAST* program of the NCBI (Altschul et al., 1990). *ClustalW* (Thompson et al., 1994) was used for the comparison of protein sequences. A variety of protein properties (e.g. molecular weight, pI, extinction coefficients) were calculated with the ProtParam tool of the Expasy proteomics server (www.expasy.ch). Binding motifs for calmodulin were analyzed with the *Calmodulin Target Database*, accessible at http://calcium.uhnres.utoronto.ca/ctdb. Part of the three-dimensional structure analysis was carried out with the program Pymol (DeLano Scientific LLC, 2006) accessible at www.pymol.org.

2.2.4. NMR spectroscopy

2.2.4.1. Structural study of FKBP38$^{35\text{-}153}$

2.2.4.1.1. Sample preparation

The NMR structural determination of FKBP38$^{35\text{-}153}$ was carried out with samples consisting of either non-labelled or ^{15}N-enriched FKBP38$^{35\text{-}153}$ (1.3-1.4 mM) dissolved in 20 mM sodium phosphate buffer (pH 6.7, 0.05% (w/v) NaN_3, 5% (v/v) D_2O) at 298 K. Under these conditions, the protein was stable for about one week.

2.2.4.1.2. NMR experiments

All NMR data were collected with Avance-700 (University of Leipzig) and DRX500 spectrometers operating at 500.13 and 700.13 MHz proton resonance frequencies respectively. Both spectrometers were equipped with 5 mm inverse triple-resonance ($^{1}H/^{13}C/^{15}N$) probes with XYZ-gradient coils. Several homonuclear two-dimensional (2D) spectra ($^{1}H/^{1}H$-TOCSY and $^{1}H/^{1}H$-NOESY), as well as ^{15}N-edited multidimensional spectra (2D $^{1}H/^{15}N$-HSQC, 2D $^{1}H/^{15}N$-HTQC, 3D $^{1}H/^{15}N$-TOCSY-HSQC and 3D $^{1}H/^{15}N$-NOESY-HSQC) were acquired. The TOCSY experiments were performed with spin-lock times of 80 ms. In addition, a 2D $^{1}H/^{1}H$-TOCSY with a spin-lock time of 6 ms was acquired in order to obtain COSY-type information with less spectral overlap. A mixing time (τ_m) of 150 ms was used in the NOESY experiments. The water signal suppression in the homonuclear one- and two-dimensional ^{1}H experiments was achieved by selective presaturation during the relaxation delay, with the carrier placed in the center of the spectrum on the water resonance. All heteronuclear experiments made use of pulsed field gradients for coherence selection and artifact suppression, and utilized gradient sensitivity enhancement schemes wherever appropriate (Muhandiram and Kay, 1994). All NMR experiments were acquired in a phase-sensitive mode at 298 K. The States-TPPI or echo/antiecho method was used to obtain quadrature detection in the indirectly-detected dimension. The chemical shifts were referenced to external 2,2-dimethyl-2-silapentane-5-sulfonate in order to ensure consistency among all spectra (Wishart et al., 1995).

All NMR spectra were processed on a Silicon Graphics O2 workstation using the XWINNMR 3.5 software package (Bruker, Rheinstetten). A 90° phase-shifted squared sine-bell function was used for apodization in all dimensions. After Fourier transformation, polynomial base-line correction was applied to the processed spectra in the directly-detected dimension. Peak picking and data analysis of the transformed spectra were performed using the AURELIA 2.5.9 (Bruker, Rheinstetten) and FELIX 2000 (Accelrys Inc., San Diego, U.S.A.) software packages.

2.2.4.1.3. Resonance assignment

The sequence-specific ^{1}H and ^{15}N resonance assignments of $FKBP38^{35-153}$ were determined according to the classical assignment strategy (Wüthrich, 1986), using the experiments from section 2.2.4.1.2.

2.2.4.1.4. Structure calculation and refinement

For the structure calculation, NOE-derived distance restraints were determined from 2D $^{1}H/^{1}H$-NOESY and 3D $^{1}H/^{15}N$-NOESY-HSQC spectra. The NOE peaks were first automatically assigned on the basis of chemical shift values with the program *nmr2st* (Pristovšek et al., 2000). An internal calibration was used to set the upper distance limits, based on the intensities of characteristic intra- and inter-strand NOEs within the β-sheet structure as well as of sequential and medium-range NOEs within the α-helix. The integrated peak intensities were converted into approximate inter-proton distances by normalizing against the calibrated intensities. The upper distance limits were subsequently classified into different categories of 2.5, 3.5, 4.5 and 6.0 Å. A pseudo-atom correction was applied for magnetically equivalent protons (Wüthrich et al., 1983). No hydrogen bond constraints were used in the structure calculation.

The structures were calculated on a Silicon Graphics O2 workstation with the program DYANA 1.5 (Güntert et al., 1997), which uses a simulated annealing algorithm combined with torsion angle dynamics. Starting *ab initio*, 100 conformers were calculated in 8000 annealing steps each. For the structure refinement an iterative strategy was used; after each round of structure refinement, the newly computed NMR structures were employed to (i) assign ambiguous NOE cross-peaks, (ii) correct erroneous assignments, and (iii) loosen the NOE distance bounds if spectral overlap was deduced. In the last stages of the structure calculation, the stereospecific assignment of prochiral groups was carried out, also in an iterative manner, with the program GLOMSA (Güntert et al., 1991). At the end, nearly all prochiral amide (6), isopropyl (26) and methylene (76) groups were stereospecifically assigned.

In the last run of calculation the structures were computed using 1585 meaningful distance restraints, obtained out of a total of 2191 NOE assignments. The 20 best DYANA conformers were subsequently submitted to a restrained energy minimization (i.e. with NOE-derived distance restraints), carried out with the DISCOVER module of the INSIGHT 2000 software package (Accelrys, San Diego, U.S.A.). For the restrained energy minimization, the consistent valence force field (Dauber-Osguthorpe et al., 1988) was used, with a dielectric constant equal to r (distance in Å). A force constant of 20 kcal $Å^{-2}$ mol^{-1} was applied in the NOE restraint terms. The 20 final selected $FKBP38^{35-153}$ conformers were analyzed with PROCHECK-NMR (Laskowski et al., 1996).

2.2.4.2. Study of the interactions of FKBP38$^{35-153}$ with Ca^{2+} and Mg^{2+}

For the study of the interactions of FKBP38$^{35-153}$ with Ca^{2+}, a sample consisting of 0.4 mM ^{15}N-enriched FKBP38$^{35-153}$, dissolved in 10 mM MES (pH 6.8) and 100 mM KCl, was titrated with a 1 M $CaCl_2$ solution, to obtain Ca^{2+} concentrations of 0, 0.14, 3.7 and 7.3 mM. At each of the titration points, a ^{1}H/^{15}N-HSQC spectrum was collected, processed and analyzed as described in section 2.2.4.1.2.

A 0.8 mM solution of non-labelled FKBP38$^{35-153}$ was also titrated with 1 M $CaCl_2$, under the same conditions as in the previously described experiment. In this case, Ca^{2+} concentrations of 0, 1, 2, 3, 6, 9 and 12 mM were obtained. During this titration, one-dimensional ^{1}H spectra were collected and processed using standard procedures.

To study the interaction of FKBP38$^{35-153}$ with Mg^{2+}, a 0.1 mM solution of non-labelled FKBP38$^{35-153}$, dissolved in 10 mM MES (pH 6.8) and 100 mM KCl, was titrated with 1 M $MgCl_2$, to obtain Mg^{2+} concentrations of 0, 10 and 20 mM. In the course of this titration, one-dimensional ^{1}H spectra were collected and processed using standard procedures.

As a control experiment, a 0.2 mM solution of ^{15}N-labelled FKBP12 was titrated with 1 M $CaCl_2$ to a Ca^{2+} concentration of 7.3 mM. ^{1}H/^{15}N-HSQC spectra of FKBP12 were collected before and after the addition of $CaCl_2$. Data acquisition, processing and analysis were carried out as described in section 2.2.4.1.2.

2.2.4.3. Study of the interactions between FKBP38 and CaM

2.2.4.3.1. Resonance assignments of apo-CaM, holo-CaM and FKBP38$^{290-313}$

All NMR data were acquired and processed as described in section 2.2.4.2.2., using a DRX500 spectrometer (Bruker, Rheinstetten) that operated at 500.13 MHz proton resonance frequency and was equipped with a 5 mm inverse triple-resonance (^{1}H/^{13}C/^{15}N) probe with XYZ-gradient coils.

No previous assignments of apo- and holo-CaM under the experimental conditions used in this study have been reported. Moreover, the construct of CaM used in this study contained an N-terminal His-tag. Therefore, the amide resonances of apo- and holo-CaM had to be newly assigned.

For apo-CaM, a complete resonance assignment of CaM from *Xenopus laevis* (100% identical to human CaM) at 23 ºC and pH 6.3 was kindly provided by Dr. Ad Bax (NIH, Bethesda, USA) and served as starting point. The assignment of the holo-CaM amide resonances was carried out starting from a previous assignment of holo-CaM from *Drosophila melanogaster* (presenting three amino acids substitutions, i.e. Y99F, D129N and Q143T, with respect to human CaM), which had been performed at 47 ºC and pH 6.3 (Ikura et al. 1990). However, in order to account for chemical shift differences due to (i) the experimental conditions and (ii) alterations in the amino acid sequence, a full set of 2D $^{1}H/^{15}N$-HSQC, 3D $^{1}H/^{15}N$-TOCSY-HSQC and 3D $^{1}H/^{15}N$-NOESY-HSQC spectra was collected for both apo- and holo-CaM to obtain sequence-specific resonance assignments at the chosen conditions.

The resonance assignment of FKBP38$^{290-313}$ was performed with a partially ^{15}N-labelled sample, were the residues Leu292, Ala297, Ala305 and Leu311 as well as the N^{ε} of Gln299 were ^{15}N-labelled. For this assignment, 2D ^{15}N-decoupled $^{1}H/^{1}H$-TOCSY and $^{1}H/^{1}H$-NOESY as well as 2D $^{1}H/^{15}N$-HSQC, 3D $^{1}H/^{15}N$-TOCSY-HSQC and 3D $^{1}H/^{15}N$-NOESY-HSQC spectra were collected and assigned.

2.2.4.3.2. Chemical shift perturbation experiments

The chemical shift perturbation experiments (CSP) were carried out at two different conditions in order to determine the interactions of FKBP38$^{35-153}$ with (i) apo- and (ii) holo-CaM. The interactions with apo-CaM were measured in 20 mM sodium phosphate buffer (pH 6.8, 0.05% (w/v) NaN_3 and 5% (v/v) D_2O), whereas the interactions with holo-CaM were measured in 10 mM MES buffer (pH 6.8, 100 mM KCl, 6 mM $CaCl_2$, 0.05% (w/v) NaN_3 and 5% (v/v) D_2O). In all experiments the protein concentrations were in the range 0.5-0.7 mM ^{15}N-labelled protein and 1.5-2.1 mM non-labelled protein, in order to obtain a 1:3 molar ratio. To ensure identical conditions in each CSP experiment, the samples were prepared according to the following procedure:

1) Two 0.5 ml solutions, each containing the required amount of FKBP38$^{35-153}$ and CaM (one protein ^{15}N-labelled and the other non-labelled), were dialyzed twice against 3 l buffer (containing all the above-mentioned components except D_2O).

2) The required amount of D_2O was added to the solution of the ^{15}N-labelled protein and a $^{1}H/^{15}N$-HSQC spectrum of the resulting sample, representing the “free” protein, collected.

3) The second (non-labelled) protein was added, the mixture of both proteins washed in a concentrator once with buffer, and then reduced to a final volume of 0.5 ml.

4) The required amount of D_2O was added again, the pH value checked (and corrected if necessary), and a $^{1}H/^{15}N$-HSQC spectrum of the resulting "complexed" protein was acquired.

Finally, the two $^{1}H/^{15}N$-HSQC spectra were compared, and the resulting alterations in the ^{1}H and ^{15}N chemical shift values used to calculate the combined chemical shift perturbation for each residue according to the following equation (Mulder et al., 1999):

$$\Delta\delta = [(\Delta\delta_{1H})^2 + (\Delta\delta_{15N} / 6.5)^2]^{½}$$

As control experiments, 0.2 mM solutions of ^{15}N-labelled FKBP12 were titrated with 3-fold excess of either apo- or holo-CaM by following the same procedure.

2.2.4.3.3. Docking calculations

The three-dimensional structures of the FKBP38$^{35-153}$/apo-CaM, FKBP38$^{35-153}$/holo-CaM and FKBP38$^{290-313}$/holo-CaM complexes were determined with the program HADDOCK (High Ambiguity Driven protein-protein DOCKing) (Dominguez et al., 2003), which is implemented in the CNS program suite (Brunger et al., 1998) and uses python scripts derived from ARIA (Linge et al., 2001) for automation. HADDOCK makes use of biophysical interaction data, such as chemical shift perturbations provided by NMR titration experiments, which are introduced into the structure calculation as ambiguous interaction restraints (AIRs) to drive the docking process. In the present work, the following independent sets of amide chemical shift perturbations were available:

For the FKBP38$^{35-153}$/apo-CaM complex:

- ^{15}N-labelled FKBP38$^{35-153}$ titrated with non-labelled apo-CaM
- ^{15}N-labelled apo-CaM titrated with non-labelled FKBP38$^{35-153}$

For the FKBP38$^{35-153}$/holo-CaM complex:

- ^{15}N-labelled holo-CaM titrated with non-labelled FKBP38$^{35-153}$
- The titration of ^{15}N-labelled FKBP38$^{35-153}$ with non-labelled holo-CaM led to a fairly rapid denaturation of FKBP38$^{35-153}$ and consequently no observable chemical shift changes. Hence, no CSP data could be obtained. In this case, the CSP data from the equivalent experiment with apo-CaM were used for the HADDOCK calculations.

For the FKBP38$^{290-313}$/holo-CaM complex:

- Partially ^{15}N-labelled FKBP38$^{290-313}$ (where the residues Leu292, Ala297, Ala305 and Leu311 as well as the N$^{\varepsilon}$ of Gln299 are ^{15}N-labelled) titrated with the non-labelled C-terminal domain of holo-CaM.
- Partially ^{15}N-labelled FKBP38$^{290-313}$ titrated with non-labelled holo-CaM.
- ^{15}N-labelled holo-CaM titrated with non-labelled FKBP38$^{290-313}$.

From each independent data set, the residues with (i) the most pronounced chemical shift perturbations or (ii) relaxation properties displaying a considerable change upon binding (i.e. changes in signal line-widths that subsequently lead to either appearance or disappearance of peaks upon binding) were selected as "active AIRs" for the HADDOCK calculations, as long as their relative surface accessibilities were higher than 20%. In the case of the FKBP38$^{290-313}$/holo-CaM complex, the cut-off for the surface accessibility was not applied, as the FKBP38 segment was found to bind to the inner cavity of the C-terminal holo-CaM domain.

The following atomic coordinates were used to (i) calculate the surface accessibilities with the program NACCESS (Hubbard and Thornton, 1993) and (ii) perform the subsequent docking calculations:

For the FKBP38$^{35-153}$/apo-CaM complex:
- NMR structure of FKBP38$^{35-153}$ (PDB ID code 2F2D, 20 conformers)
- NMR structure of apo-CaM (Kuboniwa et al. 1995; PDB ID code 1CFD, minimized average structure)

For the FKBP38$^{35-153}$/holo-CaM complex:
- NMR structure of FKBP38$^{35-153}$ (PDB ID code 2F2D, 20 conformers)
- Crystal structure of holo-CaM (Babu et al., 1988; PDB ID code 3CLN)

For the FKBP38$^{290-313}$/holo-CaM complex:
- FKBP38$^{290-313}$ segment of the simulated FKBP38$^{35-313}$ structure (see section 2.2.5.)
- Crystal structure of holo-CaM (Babu et al., 1988; PDB ID code 3CLN)

For the docking calculations of the FKBP38$^{35-153}$/apo-CaM and FKBP38$^{35-153}$/holo-CaM complexes, 400 structures each were first calculated using the rigid body docking protocol of HADDOCK. Next, the 20 structures showing the lowest AIR violations were submitted to a semi-flexible simulated annealing in torsion angle space, where the side-chains of the residues forming the protein-protein interface were left flexible. The resulting structures were finally refined in an 8 Å shell of explicit TIP3P (Jorgensen et al., 1983) water molecules. The same

procedure was used for the calculation of the FKBP38$^{290-313}$/holo-CaM complex, but only 100 structures were calculated in the first stage of the calculation, and the 20 best structures further refined.

2.2.5. Molecular dynamics simulations

The initial structures for the MD simulations of FKBP38$^{35-313}$, holo-CaM and the FKBP38$^{35-313}$/CaM complexes were created from structures available at the RCSB database by using the INSIGHT II module of the INSIGHT 2000 software package (Accelrys, San Diego, U.S.A.).

The initial structure for the simulation of FKBP38$^{35-313}$ was created by combining the NMR structure of its FKBP domain obtained in this work (PDB ID code 2F2D, conformer 1) and the backbone structure of FKBP51 (Sinars et al., 2003; PDB ID code 1KT1). The segment Pro382-Lys386, which is missing in the FKBP51 structure, was taken from the structure of FKBP52 (Wu et al., 2004; PDB ID code 1P5Q). After superposing the backbone atoms of FKBP38$^{35-153}$ and the second FKBP domain of FKBP51, several ϕ and ψ angles in the loop connecting the FKBP and TPR domains of FKBP51 were modified in order to account for differences in the length of this loop between the two proteins. The same procedure was applied in other loops of the TPR domain wherever required. Afterwards, amino acid substitutions were applied to adjust the TPR domain to the FKBP38 sequence. The thus obtained structure combines the TPR domain backbone structure of FKBP51, as well as its relative FKBP-TPR domain orientation, with the structure of FKBP38$^{35-153}$.

The starting structures for the simulation of holo-CaM with a flexible linker were created from the crystal structure of holo-CaM (Babu et al., 1988; PDB ID code 3CLN). Two starting structures with extended linkers were produced, one with a linker from Glu78 to Ser81 and another with a linker from Met76 to Ser81. To achieve this, the ψ angles of the residues forming the linker were modified to values in the β-sheet region, thus producing extended backbone conformations.

For the simulation of the FKBP38$^{35-313}$/holo-CaM complex, the starting structure was created from the FKBP38$^{290-313}$/holo-CaM complex, which had been obtained by docking calculations with HADDOCK as described in section 2.2.4.3.3., as well as from one MD structure each of FKBP38$^{35-313}$ and holo-CaM. First, the MD structures of holo-CaM and FKBP38$^{35-313}$ were superposed to the C-terminal domain of holo-CaM and FKBP38$^{290-313}$ in the FKBP38$^{290-313}$/holo-CaM complex, respectively. Afterwards, the C-terminal domain of the holo-CaM MD structure

and the segment FKBP38$^{290-313}$ of the FKBP38$^{35-313}$ structure were deleted.

In an analogous manner, the starting structure for the simulation of the FKBP38$^{35-313}$/holo-CaM complex was combined with the NMR solution structure of apo-CaM (Kuboniwa et al., 1995; PDB ID code 1CFD, minimized average structure) to obtain a starting structure for the simulation of the FKBP38$^{35-313}$/semiloaded-CaM complex, where the N-terminal domain of CaM is free of Ca^{2+}. This structure was obtained by replacing the N-terminal CaM domain in the FKBP38$^{35-313}$/holo-CaM complex with the N-terminal domain of the apo-CaM structure.

The MD simulations were performed using the GROMACS 3.3 program package (van der Spoel et al., 2005; www.gromacs.org) and the gromos96 (43a1) force field (van Gunsteren et al., 1996) provided by GROMACS. In all simulations, the simulated system consisted of either a single protein molecule or a protein/protein complex, 100 mM NaCl and SPC water molecules (Berendsen et al., 1981) in a cubic box. The box dimensions were set more than 3 Å longer than the protein or protein/protein complex diameter. Prior to the MD simulations, the starting geometries were optimized by molecular mechanics (MM) using the steepest descent algorithm (1000 steps) to remove tight contacts at the protein-solvent and ion-solvent interfaces.

The MD simulations were performed at constant temperature (coupling the system to a Berendsen thermostat set to 300 K, bath relaxation time 0.1 ps) and pressure (isotropic coupling to 1 bar at a relaxation time of 1 ps) (Berendsen et al., 1984) with periodic boundary conditions. The leapfrog algorithm was used for time propagation with a time step of 0.002 ps. For the calculation of the van der Waals interactions, a twin range cut-off radius of 1 Å was used. The neighbor list was updated every 20 steps within a cut-off radius of 1 Å. The Fast Particle-Mesh Ewald method (Darden et al., 1993; Essmann et al., 1995) was applied to calculate the electrostatic interactions, with a maximum grid spacing of 0.12 nm for the fast Fourier transformation grid and 4th order interpolation. All bond lengths were constrained with the LINCS algorithm (Hess et al., 1997). In all simulations involving Ca^{2+}-bound forms of CaM, additional distance restraints of 2.59 Å were imposed between the Ca^{2+} ions and the protein atoms coordinating Ca^{2+}, analogous to the NMR structure determination of CaM/target peptide complexes (Elshort et al., 1999). The protein geometries were recorded every 500 time steps (1 ps). All simulations were performed on an Intel Pentium 4 3.20 GHz processor, with effective calculation times ranging from 4 to 7 days per nanosecond.

At the beginning of the MD simulations, atomic velocities were generated at 290 K with a Maxwellian distribution. Next, three short consecutive position-restrained MD runs were

performed for equilibration, each consisting of 10,000 time steps of 0.0005, 0.001 and 0.002 ps, respectively. Finally, unrestrained MD simulations were performed for 5 ns in the case of holo-CaM and 9 ns in the case of FKBP38$^{35\text{-}313}$.

For the simulation of the FKBP38$^{35\text{-}313}$/holo-CaM and FKBP38$^{35\text{-}313}$/semiloaded-CaM complexes, three consecutive restrained MD runs were performed after the equilibration runs, with incorporation of small sets of distance restraints obtained from the HADDOCK structures of the FKBP38$^{35\text{-}153}$/holo-CaM complex (for the FKBP38$^{35\text{-}313}$/holo-CaM complex simulation), the FKBP38$^{35\text{-}153}$/apo-CaM complex (for the FKBP38$^{35\text{-}313}$/semiloaded-CaM complex simulation), and the FKBP38$^{290\text{-}313}$/holo-CaM complex (for both simulations). In these restrained MD simulations, the restraints were used in a fashion typical for NMR-based structure calculations (i.e. in form of (i) quadratic potentials below a specified lower bound and between two specified upper bounds and (ii) linear potentials beyond the largest bound). The force constant for the distance restraints was progressively increased in the three runs, from 200 to 500 to 1000 kJ mol^{-1} nm^{-2}, in order to produce a smooth trajectory towards the final structure. The simulation time for these MD runs was 0.5 ns each (i.e. 1.5 ns in total).

2.2.6. Crystal structure analysis of FKBP38$^{35\text{-}153}$

The crystallization of FKBP38$^{35\text{-}153}$ was performed using the sitting-drop vapor diffusion method. First, the protein was screened with the crystallization kits JBScreen Classic 1-4 and Crystal Screen^{TM} 1-2 (96 crystallization conditions each), employing protein concentrations of 5, 10 and 20 mg/ml. Small crystals were found in both plates at the same condition, where the protein (at a concentration of 20 mg/ml) was crystallized with a reservoir solution consisting of 30% PEG4000, 0.2 M $MgCl_2$ and 0.1 M TRIS (pH 8.5). In order to improve the quality of the crystals, a screening around this condition was carried out, with PEG4000 concentrations of 10, 20 and 30%, as well as pH values of 7.5, 8.0, 8.5 and 9.0. Furthermore, a second set of conditions was tested, where $MgCl_2$ was substituted by $CaCl_2$. The crystals displaying the best diffraction results (Figure 11) were finally obtained with a reservoir solution consisting of 30% PEG4000, 0.2 M $CaCl_2$ and 0.1 M TRIS (pH 7.5).

X-ray diffraction measurements were performed at the PSF beamline of the BESSY synchrotron facility (Berlin), where the crystals were cooled to 100 K. The beamline was tuned to a wavelength of 0.95373 Å and a MAR-225 MOSAIC CCD detector was used at a crystal-to-detector distance of 100 mm. The data were collected in a range of 0º to 180º, applying 1º steps

that amounted to a total of 180 images (3 sec collection time each).

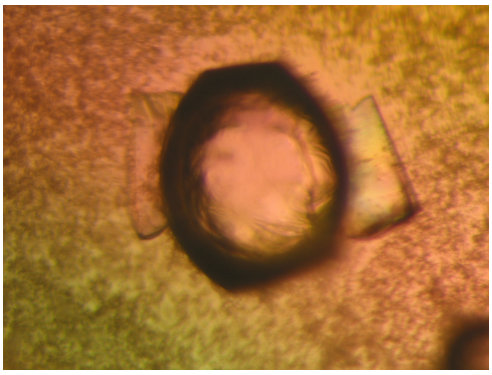

A

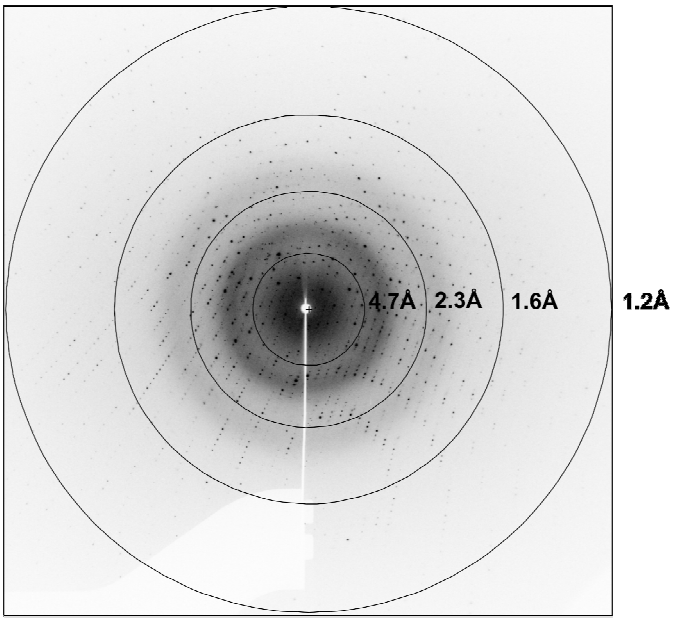

B

Figure 11. (**A**) Picture of the FKBP38$^{35\text{-}153}$ crystals displaying the best diffraction results, growing at the interface with an air bubble. (**B**) Diffraction image of one of these FKBP38$^{35\text{-}153}$ crystals, which was used for the structure determination.

Data processing was carried out with the programs MOSFLM (Leslie, 1994) and SCALA, which is part of the CCP4 software package (Collaborative computational project, 1994). The FKBP38$^{35\text{-}153}$ structure was determined by molecular replacement using the program PHASER and a previously determined X-ray structure of FKBP38$^{31\text{-}148}$ as search model. Structure refinement was performed with the program REFMAC5 of the CCP4 package. Statistics about the data collection and refinement are presented in Table 2.

Table 2. X-ray data collection and refinement statistics.

Data collection		Refinement	
Space group	$P2_1$	Resolution (Å)	60.3-1.1
Cell dimensions		No. reflections (work/test)	18,643/2,118
a, *b*, *c* (Å)	29.06, 60.29, 30.84	R_{work} / R_{free}	13.3/15.3
α, β, γ (°)	90, 97.59, 90	No. atoms	
Resolution (Å)	1.05	Protein	900
R_{merge}	4.3 (11.8)	Water	279
I / σI	20.1 (5.6)	*B*-factors	
Completeness (%)	90.4 (52.4)	Protein	8.65
Redundancy	3.3 (2.1)	Water	22.88
		R.m.s deviations:	
		Bond lengths (Å)	0.011
		Bond angles (°)	1.55

The values in parentheses are for the highest-resolution shell (1.05-1.11 Å).

3. Results and discussion

3.1. NMR assignment of the ^{1}H and ^{15}N resonances of FKBP38$^{35-153}$

The sequential assignment of the ^{1}H and ^{15}N resonances of FKBP38$^{35-153}$ (Figure 12) was carried out using the classical assignment strategy (Wüthrich, 1986), whereby the spins systems corresponding to the different amino acids are first identified by means of scalar connectivities (from TOCSY and COSY experiments) and then sequentially assigned via NOE connectivities (from NOESY experiments, Figure 13). Spectral overlap arising from amide protons resonances with similar chemical shifts is overcame by the measurement of heteronuclear experiments on ^{15}N-labelled protein, which allow the introduction of an additional ^{15}N dimension displaying higher spectral dispersion. Thus, three-dimensional ^{15}N-edited TOCSY and NOESY experiments ($^{1}H/^{15}N$-TOCSY-HSQC and $^{1}H/^{15}N$-NOESY-HSQC) were used for the sequential assignment (Figure 13B). Nearly all backbone and side-chain ^{15}N and ^{1}H resonances, with the exception of the backbone amide groups of the two cloning artifacts Met33 and Arg34, were assigned (Table 3). The assignment has been deposited at the BioMagResBank data base under accession number BMRB-6902.

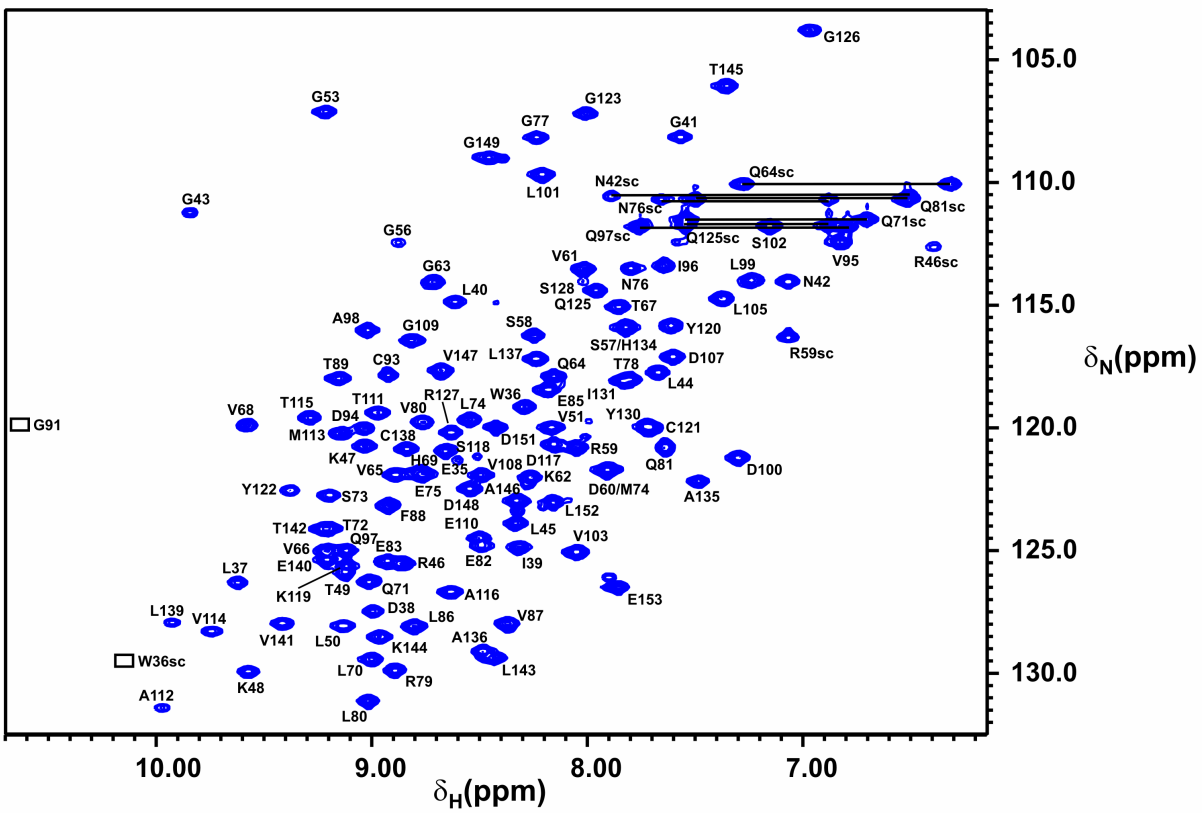

Figure 12. Two-dimensional $^{1}H/^{15}N$-HSQC spectrum of FKBP38$^{35-153}$ recorded at 500.13 MHz. The sequence-specific assignment of the amide resonances is indicated. Boxes indicate signals that appear below the plot level. Side-chain resonances are marked with the suffix sc. Arginine side-chain signals are folded in the nitrogen dimension. Horizontal lines connect signals that belong to NH_2 groups.

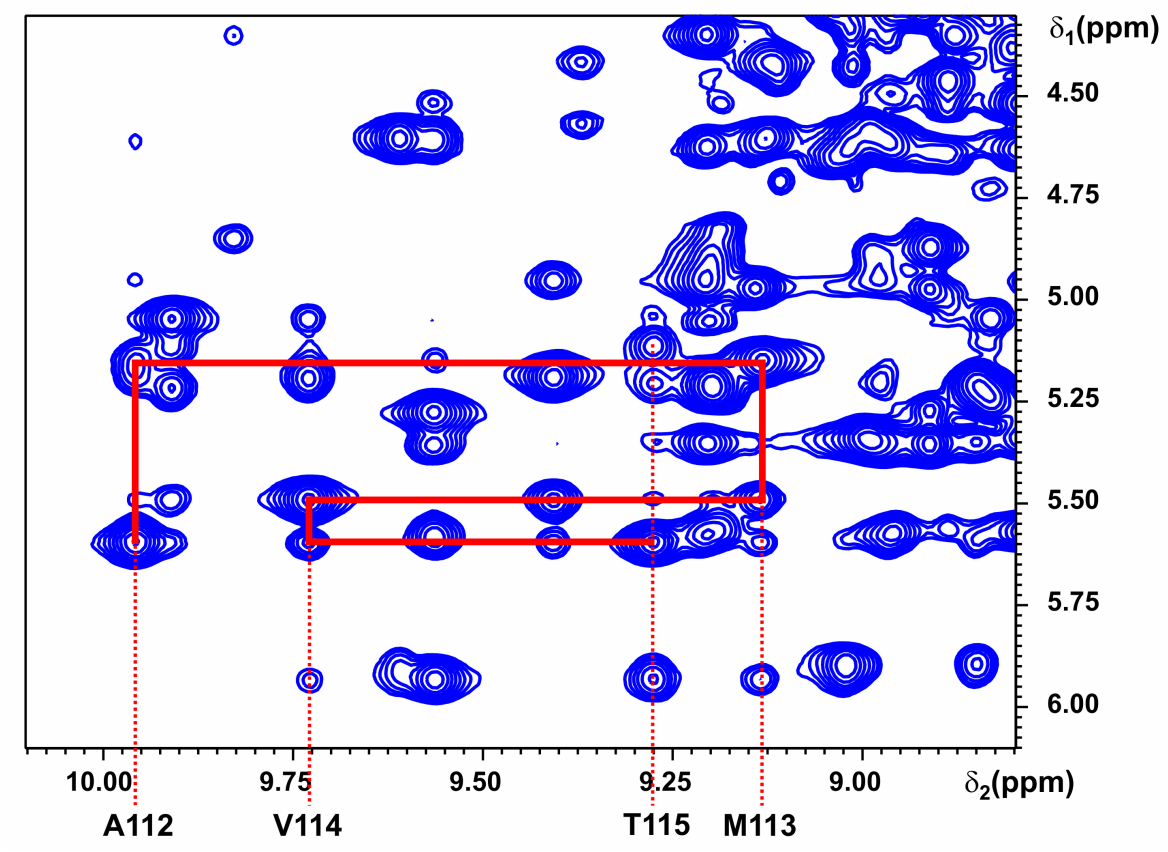

A

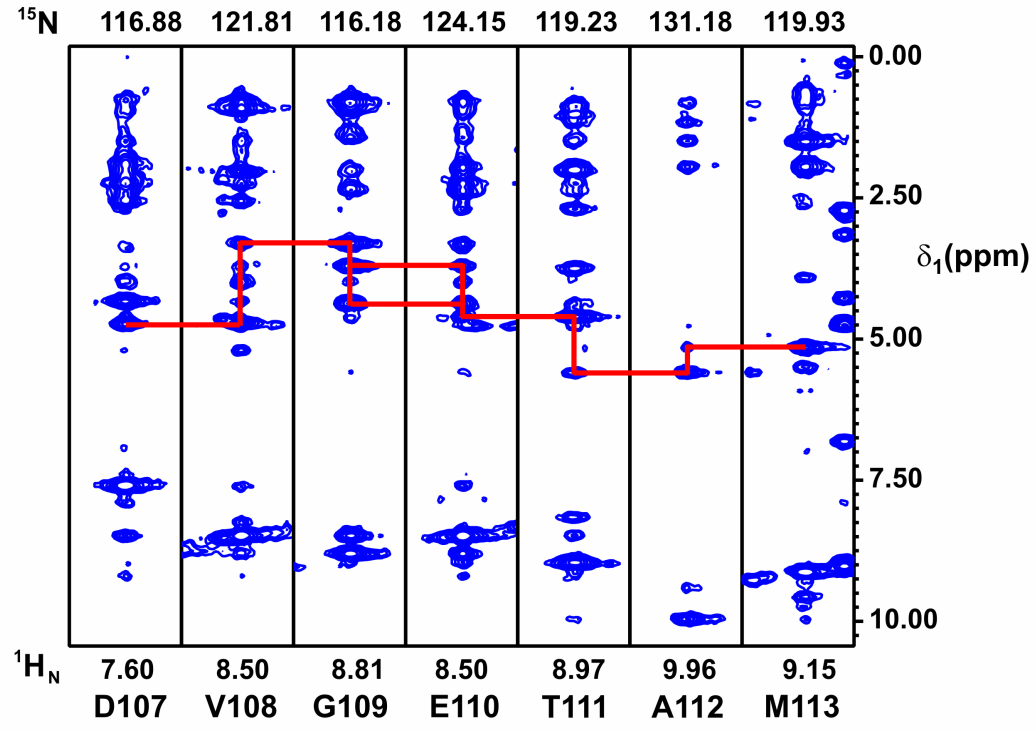

B

Figure 13. (**A**) Section of the NOESY spectrum (recorded at 700.13 MHz) of FKBP38$^{35\text{-}153}$, showing part of the fingerprint region. The H_N-H_α resonances corresponding to the segment Ala112-Thr115 are sequentially assigned via $H^N(i)$-$H^\alpha(i\text{-}1)$ NOE connectivities. (**B**) Selection of ^{15}N slices from the 3D $^1H/^{15}N$-NOESY-HSQC of FKBP38$^{35\text{-}153}$ recorded at 500.13 MHz. The H_N-H_α resonances corresponding to the segment Asp107-Met113 are assigned sequentially via $H^N(i)$-$H^\alpha(i\text{-}1)$ NOE-connectivities.

Table 3. ^{1}H and ^{15}N resonance assignments (in ppm) of FKBP38$^{35-153}$ at 298 K and pH 6.7. Stereospecific assignments are indicated by IUPAC numbering.

AA	*N*	H^N	H^α	*Other H*	*Other N*
M33	n.a.	n.a.	3.93	2.11β, 2.06β, 2.60γ, 2.10ε	
R34	n.a.	n.a.	4.37	1.90β, 1.77β, 1.68γ, 1.63γ, 3.22δ, 3.20δ	
E35	121.3	8.60	4.25	2.06β2, 1.95β3, 2.26γ, 2.09γ	
W36	119.2	8.29	4.63	3.09β2, 2.87β3, 7.33δ1, 10.15ε1, 7.22ε3, 7.45ζ2, 7.00ζ3, 7.00η2	129.5ε1
L37	126.3	9.62	4.60	1.71β2, 1.94β3, 1.48γ, 0.99δ, 0.95δ	
D38	127.4	9.00	4.78	3.12β, 2.57β	
I39	124.9	8.33	3.47	1.60β, 1.79γ1, 0.77γ2, 0.73δ1	
L40	114.9	8.62	4.60	1.80β, 1.60β, 1.35γ, 0.81δ1, 0.58δ2	
G41	108.2	7.58	4.12, 3.60		
N42	114.0	7.07	4.86	2.77β2, 3.29β3, 6.51δ21, 7.89δ22	110.6δ2
G43	111.3	9.84	4.05α2, 3.47α3		
L44	117.7	7.68	4.37	1.69β2, 1.95β3, 1.57γ, 0.94δ1, 0.83δ2	
L45	123.9	8.33	5.22	1.68β, 1.27γ, 0.79δ1, 0.50δ2	
R46	125.5	8.86	5.90	1.78β, 1.32γ, 2.74δ, 6.40ε	82.6ε
K47	120.8	9.04	5.95	1.79β, 1.75β, 1.36γ, 1.44δ2, 1.49δ3, 2.61ε, 2.55ε	
K48	129.9	9.58	4.62	0.60β2, 0.57β3, 0.10γ, 0.64δ2, 0.72δ3, 2.17ε2, 2.37ε3	
T49	125.9	9.13	3.93	3.80β, 1.02γ2	
L50	128.1	9.14	4.43	1.45β, 1.57γ, 0.82δ1, 0.72δ2	
V51	120.0	8.17	4.49	2.07β, 1.05γ1, 0.89γ2	
P52	n.a.	-	4.37	2.30β, 2.02γ2, 1.91γ3, 3.57δ2, 3.78δ3	
G53	107.2	9.22	3.43α2, 4.01α3		
P54	n.a.	-	4.71	2.34β, 2.10γ, 1.97γ, 3.74δ	
P55	n.a.	-	4.37	2.30β, 1.87β, 2.12γ, 2.01γ, 3.58δ2, 3.85δ3	
G56	112.5	8.88	4.17, 3.73		
S57	115.9	7.83	4.34	4.05β, 3.95β, 6.01γ	
S58	116.2	8.26	4.77	3.79β2, 3.87β3	
R59	120.8	8.05	5.21	1.52β2, 1.91β3, 1.54γ2, 1.76γ3, 3.06δ2, 3.18δ3, 7.07ε	86.3ε
P60	n.a.	-	4.67	1.63β, 1.69γ, 4.03δ2, 3.70δ3	
V61	113.6	8.02	4.45	2.03β, 0.91γ1, 0.76γ2	
K62	122.0	8.27	3.61	1.82β2, 1.68β3, 1.33γ2, 1.50γ3, 1.75δ, 1.69δ, 3.03ε	
G63	114.1	8.71	4.44α2, 3.49α3		
Q64	117.9	8.16	4.48	2.26β, 2.24β, 2.50γ, 7.28ε21, 6.32ε22	110.1ε2
V65	121.9	8.89	4.25	1.79β, 0.63γ1, 0.91γ2	
V66	125.0	9.22	5.06	1.69β, 0.67γ1, 0.02γ2	
T67	115.1	7.86	5.29	4.00β, 1.06γ2	
V68	119.9	9.58	5.57	2.19β, 0.94γ1, 1.07γ2	
H69	121.8	8.79	5.34	3.16β2, 3.08β3, 7.01δ2, 7.92ε1	
L70	129.4	9.00	5.37	1.21β2, 1.87β3, 1.47γ, 0.93δ1, 0.83δ2	
Q71	126.3	9.01	4.92	2.13β, 2.09β, 2.21γ2, 2.32γ3, 7.55ε21, 6.73ε22	111.5ε2
T72	124.1	9.20	4.84	3.96β, 1.18γ2	
S73	122.8	9.20	5.57	3.69β, 6.04γ	
L74	119.7	8.55	4.74	1.98β, 1.95β, 1.79γ, 0.95δ1, 1.05δ2	
E75	121.9	8.76	3.96	2.06β, 2.01β, 2.21γ2, 2.28γ3	
N76	113.5	7.80	4.55	3.31β2, 2.87β3, 6.89δ21, 7.66δ22	110.7δ2
G77	108.2	8.24	4.39, 3.77		
T78	118.0	7.81	4.05	4.05β, 1.19γ2	
R79	129.9	8.89	4.54	1.82β, 1.61γ2, 1.67γ3, 3.20δ, 7.17ε	83.8ε
V80	119.8	8.76	4.34	2.09β, 0.92γ1, 0.76γ2	

Q81	120.8	7.64	4.45	1.90β, 2.21γ, 7.52ε21, 6.54ε22	110.7ε2
E82	124.8	8.49	4.87	2.02β, 1.92β, 2.24γ	
E83	125.4	8.93	4.88	2.12β2, 1.98β3, 2.22γ	
P84	n.a.	-	4.06	2.13β, 2.00β, 1.89γ, 3.91δ2, 3.60δ3	
E85	118.4	8.18	4.51	1.97β2, 1.77β3, 2.06γ	
L86	128.1	8.81	4.65	1.38β2, 1.94β3, 1.60γ, 0.94δ1, 0.78δ2	
V87	128.0	8.38	5.37	1.89β, 0.76γ1, 0.97γ2	
F88	123.2	8.92	4.99	3.14β, 6.95δ, 7.15ε, 6.83ζ	
T89	118.0	9.14	4.64	4.14β, 1.00γ2	
L90	131.1	9.02	4.36	1.44β2, 1.92β3, 1.60γ, 1.01δ1, 0.75δ2	
G91	119.9	10.63	3.92α2, 4.29α3		
D92	121.7	7.93	4.83	2.89β2, 2.73β3	
C93	117.8	8.92	4.31	3.18β, 3.15β	
D94	120.0	9.04	4.67	2.78β2, 2.71β3	
V95	112.4	6.83	4.23	1.78β, 0.34γ1, 0.13γ2	
I96	113.4	7.65	4.03	2.11β, 1.25γ12, 1.14γ13, 0.23γ2, 0.70δ1	
Q97	125.0	9.12	4.00	2.25β, 2.50γ2, 2.65γ3, 7.78ε21, 6.80ε22	111.8ε2
A98	116.0	9.02	3.84	1.11β	
L99	114.0	7.24	4.21	1.27β2, 1.54β3, 1.37γ, 0.75δ	
D100	121.2	7.31	4.56	2.41β2, 2.58β3	
L101	109.7	8.21	4.27	1.59β2, 1.17β3, 1.80γ, 0.67δ1, 0.83δ2	
S102	111.8	7.16	4.45	3.62β2, 3.53β3, 5.26γ	
V103	125.1	8.06	3.95	2.30β, 1.28γ1, 1.01γ2	
P104	n.a.	-	4.32	2.43β, 2.12γ2, 1.80γ3, 3.12δ2, 3.62δ3	
L105	114.8	7.38	4.35	1.74β, 1.70β, 1.60γ, 0.96δ, 0.85δ	
M106	121.7	7.91	4.35	2.09β, 2.49γ, 2.10ε	
D107	117.1	7.61	4.74	2.27β2, 2.58β3	
V108	121.9	8.50	3.32	2.05β, 0.83γ1, 0.95γ2	
G109	116.4	8.81	3.73α2, 4.39α3		
E110	124.5	8.50	4.63	2.04β, 1.98β, 2.40γ2, 2.24γ3	
T111	119.4	8.98	5.62	3.77β, 6.57γ1, 1.18γ2	
A112	131.4	9.97	5.16	1.51β	
M113	120.2	9.14	5.50	1.90β2, 2.00β3, 2.66γ2, 2.50γ3, 2.12ε	
V114	128.3	9.74	5.61	2.03β, 0.85γ2, 0.91γ3	
T115	119.6	9.29	5.13	4.12β, 1.12γ2	
A116	126.7	8.64	5.37	1.11β	
D117	120.7	8.16	4.48	2.98β2, 2.49β3	
S118	121.0	8.66	3.94	3.60β2, 3.51β3	
K119	125.6	9.12	3.99	1.65β2, 1.28β3, 0.55γ2, 0.93γ3, 1.39δ, 1.37δ, 2.75ε	
Y120	115.9	7.62	4.73	2.58β2, 3.26β3, 6.92δ, 6.69ε	
C121	119.9	7.71	4.43	3.22β2, 2.33β3, 2.60γ	
Y122	122.6	9.37	4.59	2.64β2, 3.16β3, 7.17δ, 6.67ε	
G123	107.2	8.01	4.16α2, 3.61α3		
P124	n.a.	-	3.32	2.30β2, 1.92β3, 2.08γ2, 1.99γ3, 3.60δ2, 3.96δ3	
Q125	114.4	7.98	4.14	2.16β2, 2.31β3, 2.57γ2, 2.44γ3, 7.55ε2, 6.89ε2	111.8ε2
G126	103.8	6.98	3.69, 3.59		
R127	120.2	8.63	4.24	0.57β, 1.13γ2, 1.28γ3, 2.72δ2, 2.82δ3, 7.04ε	
S128	118.1	7.84	4.34	3.83β, 3.73β	
P129	n.a.	-	4.73	1.99β, 1.65β, 0.54γ2, 1.58γ3, 3.16δ2, 3.40δ3	
Y130	119.9	7.73	4.70	2.95β2, 3.27β3, 7.15δ, 6.88ε	
I131	118.1	7.84	4.74	1.72β, 0.91γ1, 1.02γ2, 0.78δ1	
P132	n.a.	-	3.72	1.97β, 2.05γ, 3.68δ, 3.53δ	
P133	n.a.	-	4.33	2.03β, 1.93β, 1.57γ2, 2.25γ3, 3.60δ	
H134	115.9	7.82	3.86	3.25β, 3.19β, 6.91δ2, 7.80ε1	
A135	122.2	7.49	4.48	1.35β	

A136	129.1	8.49	4.62	1.46β	
L137	117.2	8.24	5.25	1.90β, 1.41γ, 1.05δ1, 0.89δ2	
C138	120.9	8.84	5.06	2.70β2, 2.90β3	
L139	127.9	9.92	5.23	1.89β2, 1.66β3, 1.27γ, 0.94δ1, 0.69δ2	
E140	125.3	9.21	5.20	2.03β, 1.94γ	
V141	128.0	9.42	4.96	1.96β, 0.84γ1, 0.82γ2	
T142	124.1	9.22	5.58	4.07β, 1.03γ2	
L143	129.4	8.44	4.66	1.92β, 1.44γ, 0.88δ1, 0.76δ2	
K144	128.5	8.98	4.30	1.67β2, 1.85β3, 1.38γ2, 1.53γ3, 1.73δ, 1.63δ, 2.95ε	
T145	106.1	7.36	4.52	4.06β, 5.53γ1, 1.10γ2	
A146	123.0	8.33	5.02	1.11β	
V147	117.7	8.68	4.66	2.19β, 0.91γ1, 0.82γ2	
D148	122.5	8.55	4.66	2.77β2, 2.57β3	
G149	109.0	8.45	4.22α2, 3.98α3		
P150	n.a.	-	4.41	1.92β2, 2.25β3, 1.97γ2, 2.00γ3, 3.63δ, 3.56δ	
D151	120.0	8.43	4.60	2.58β2, 2.74β3	
L152	123.0	8.16	4.36	1.63β, 1.63γ, 0.91δ, 0.86δ	
E153	126.5	7.86	4.09	1.90β2, 2.03β3, 2.20γ	

n.a. Not assigned

3.2. Three-dimensional structure of FKBP38$^{35\text{-}153}$

The solution structure of FKBP38$^{35\text{-}153}$ was determined from a set of 1585 distance restraints, derived from a total of 2191 NOE assignments. The atomic coordinates were deposited at the RCSB database under PDB ID code 2F2D. A superposition of the final 20 energy-minimized conformers is shown in Figure 14A. The NOE connectivity pattern between the backbone protons was used to determine the secondary structure elements of the protein. A large number of strong sequential $d_{\alpha N}$(i, i+1) NOE connectivities indicated predominantly β-strand elements. Additional inter-strand NOEs revealed an antiparallel β-sheet structure consisting of 6 β-strands: Leu37-Asp38 (βA), Leu45-Thr49 (βB), Gln64-Leu74 (βC), Thr78-Leu90 (βD), Glu110-Asp117 (βE) and Ala136-Asp148 (βF). The fourth β-strand βD, however, is interrupted by two bulges at residues Val80 and Pro84; in addition, β-strand βF shows a bulge at residue Lys144. Furthermore, based on a series of strong sequential d_{NN}(i, i+1), weaker $d_{\alpha N}$(i, i+1), as well as a dense network of medium-range d_{NN}(i, i+2), $d_{\alpha N}$(i, i+2), $d_{\alpha N}$(i, i+3), $d_{\alpha\beta}$(i, i+3) and $d_{\alpha N}$(i, i+4) connectivities, an α-helix element spanning residues Gln97-Pro104 has been identified between β-strands βD and βE, with a slight kink at residue Val103. A helical loop was found in the segment Ser118-Tyr122. The presence of a strong sequential $d_{\alpha\alpha}$(i, i+1) NOE connectivity between Ser128 and Pro129 (located in the extended loop βD-βE) revealed that this peptide bond is in *cis* conformation; all other proline residues are *trans* forms, as indicated by the observation of strong NOE connectivities between the proline C_δ protons and the respective H_α of the preceding residue (Wüthrich, 1986).

A **B**

Figure 14. Representation of the FKBP38$^{35\text{-}153}$ structure. (**A**) Stereo view showing the C$^{\alpha}$ traces of the 20 selected FKBP38$^{35\text{-}153}$ conformers. (**B**) Ribbon diagram displaying the secondary structure elements of a single FKBP38$^{35\text{-}153}$ conformer. The helical segments are colored in red, while β-strands are represented as blue arrows.

Table 4. Structural statistics of the final 20 energy-minimized FKBP38$^{35\text{-}153}$ conformers.

NOE-derived distance restraints:	1585
Intraresidual ($i = j$)	288
Sequential ($\|i - j\| = 1$)	521
Medium-range ($1 < \|i - j\| \leq 4$)	194
Long-range ($\|i - j\| > 4$)	582
Restraint violations	
Total number of restraint violations >0.3 Å	0
Total number of restraint violations >0.2 Å	6
Maximal restraint violation (Å)	0.23
Ramachandran plot (%)	
Most favored regions	69.8
Additionally allowed regions	25.5
Generously allowed regions	2.7
Disallowed regions	2.0
Structural precision (Å)	
Backbone atom[a] RMSD (residues 36-149)	1.73 ± 0.22
Heavy atom RMSD (residues 36-149)	2.25 ± 0.23
Backbone atom[a] RMSD (residues 36-117, 136-149)	1.48 ± 0.18
Heavy atom RMSD (residues 36-117, 136-149)	1.99 ± 0.22
Backbone atom[a] RMSD (secondary structure elements)	1.08 ± 0.13
Heavy atom RMSD (secondary structure elements)	1.77 ± 0.25

[a] N, C$^{\alpha}$, C' and O.

The overall structure of the 20 energy-minimized FKBP38$^{35\text{-}153}$ conformers shows a backbone RMSD for the non-terminal residues (Trp36-Gly149) of 1.73 ± 0.22 Å and only few violations of the experimental constraints (Table 4). A six-stranded antiparallel β-sheet with a +1, +3, +1, -3, +1 topology curves around the central helix, thus forming a so-called "half β-barrel". Excluding the long Ser118-Ala135 loop, which covers the proposed FK506-binding pocket and shows a fairly high conformational variability, the RMSD of the backbone structure drops down to 1.48 ± 0.18 Å; excluding all loops structures, the backbone RMSD of only the secondary structure

elements (one α-helix and six β-strands) decreases further to 1.08 ± 0.13 Å. The analysis of the backbone dihedral angles ϕ and ψ, displayed in the Ramachandran diagram (Figure 15), shows that 98% of all non-glycine/non-proline residues in FKBP38$^{35\text{-}153}$ fall within the allowed regions of the conformational space.

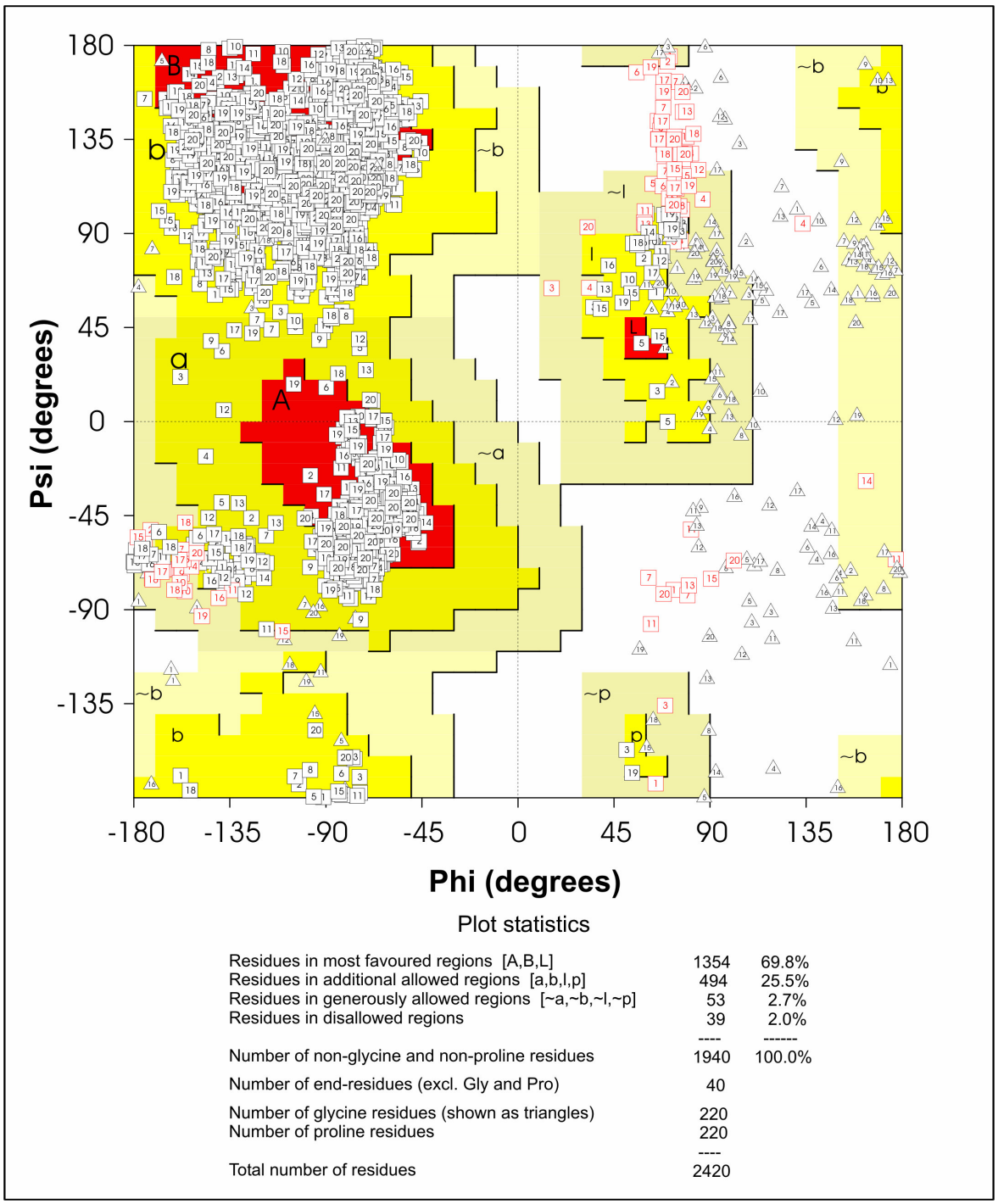

Figure 15. Ramachandran diagram of the final 20 energy-minimized FKBP38$^{35\text{-}153}$ conformers.

The overall structure of FKBP38$^{35\text{-}153}$ (Figure 14B) resembles the typical fold of FKBP domains, although this particular domain exhibits no PPIase activity and is not able to bind the low-molecular-weight inhibitor FK506 in the absence of CaM. A comparison with the crystal

structure of the immunosuppressive FKBP12/FK506 complex (PDB ID code 1FKJ) (Figure 16A) shows no major structural differences, as reflected by an average backbone RMSD of 1.70 ± 0.19 Å between the structure of FKBP12 and the 20 FKBP38$^{35\text{-}153}$ conformers (more precisely: segments Leu45-Gly53, Gly56-Gly77, Val95-Thr115 and Ala136-Leu143), which is comparable to the value obtained for the NMR ensemble itself (Table 4). The main structural difference between both structures is observed in β-strand βD of FKBP38$^{35\text{-}153}$ (β5 of FKBP12) within the segment Glu83-Leu86 (Ser39-Phe46 in FKBP12) (Figure 16A). In the case of FKBP38$^{35\text{-}153}$, β-strand βD is interrupted by only a small bulge affecting the positions of residues Pro84 and Glu85, whereas FKBP12 exhibits a larger loop (Arg40 – Pro45) with 4 additional residues. As a consequence, the side-chain of Glu83 in FKBP38$^{35\text{-}153}$ takes on a different orientation than the corresponding Ser39 side-chain in FKBP12, thereby extending into the putative FK506-binding site of FKBP38$^{35\text{-}153}$ in a similar orientation as Arg42 in FKBP12, but getting much closer to the FK506 molecule than the Arg42 side-chain (Figure 16B). In addition, the long βE-βF loop, which shows a high degree of conformational variability in the 20 conformers of the FKBP38$^{35\text{-}153}$ solution structure, is slightly closer to the binding site than in FKBP12. Residue His87 of FKBP12, located in this loop, is replaced by the larger side-chain of Arg127 in FKBP38$^{35\text{-}153}$, which also shows a high degree of conformational variability and reaches into the putative binding pocket in 80% of the conformers, possibly blocking the access to the binding site (Figure 16C). Moreover, Arg127 apparently can form salt bridge contacts inside the binding pocket with both Glu83 and Asp94 (either separately or simultaneously), as observed in several of the NMR conformers (Figure 16D); these salt bridge interactions (centroid distances between the guanidinium and carboxylate groups < 4 Å) might stabilize a “closed conformation” of the FKBP38$^{35\text{-}153}$ entry portal region in contrast to FKBP12. Nevertheless, an R127A mutant of FKBP38$^{35\text{-}153}$ showed no constitutive FKBP activity (Moutty, 2006), indicating that such salt bridge interactions cannot be the only reason for the inactivity of this FKBP domain. Hence, the lack of FKBP activity of FKBP38$^{35\text{-}153}$ may be better explained by a combination of factors: (i) an active site closed by the βE-βF loop and (ii) the orientation of the Glu83 and Arg127 side-chains towards the putative FK506-binding site. Moreover, some amino acid replacements around the putative active site (i.e., FKBP38 segments Val80-Phe88, Gly91-Ile96 and Tyr120-Ile131) indicate a clear change in the net surface charge from +2 (or +3 if His87 is in the protonated state) in FKBP12 to -4 in FKBP38 (Figure 17). This charge difference of 6 (or 7) units in the surface potentials around the entry portal of the two related FKBP domains may be important for substrate discrimination, especially in the case of charged polypeptide substrates, and could therefore be an explanation for their distinct functional behaviors.

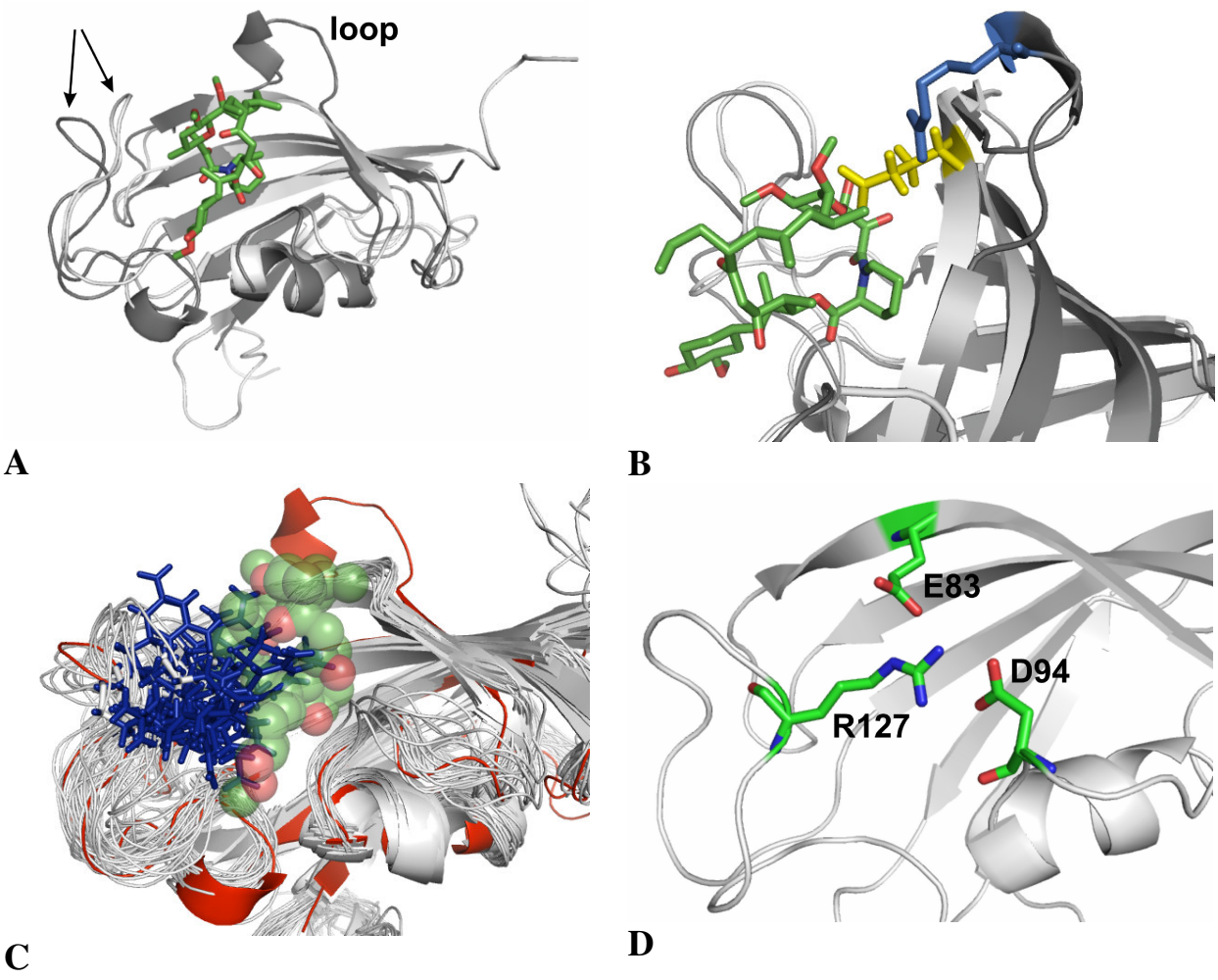

Figure 16. Structural features of FKBP38$^{35\text{-}153}$. (**A**) Superposition of FKBP38$^{35\text{-}153}$ (one conformer, represented as light gray ribbon) and the FKBP12/FK506 complex (dark gray ribbon with ligand as stick model colored by atom type; PDB ID code 1FKJ). The FKBP38$^{35\text{-}153}$ βE-βF loop and the corresponding FKBP12 β2-β3 loop, which differ in their positions relative to the active site, are indicated by arrows. The additional loop Arg40-Pro45 in FKBP12 is labelled. (**B**) Close-up of (A) with the side-chains of Glu83 (FKBP38$^{35\text{-}153}$) and Arg42 (FKBP12) displayed as yellow and blue sticks, respectively. (**C**) Superposition of the 20 selected FKBP38$^{35\text{-}153}$ conformers (represented as gray ribbon) with the FKBP12/FK506 complex (red ribbon with ligand as transparent spheres colored by atom type). The Arg127 side-chains of the FKBP38$^{35\text{-}153}$ conformers, which partially overlap with the FK506 ligand, are represented as blue sticks. (**D**) Close up of the FKBP38$^{35\text{-}153}$ structure. The side-chains the residues Arg127, Glu83 and Asp94, forming two salt bridges in this conformer, are shown as stick models.

It had been reported that FKBP38 supposedly acts as an intrinsic inhibitor of the Ser/Thr protein phosphatase CaN (Shirane and Nakayama, 2003). This would implicate that the FKBP domain of FKBP38 can mimic the FKBP12/FK506 complex, which is an inhibitor of CaN. On the other hand, more recent reports indicate that FKBP38 cannot inhibit CaN in absence of bound FK506 (Kang et al., 2005; Weiwad et al., 2005). The interaction of the FKBP12/FK506 complex with CaN is mediated by the FK506 molecule and several FKBP12 residues surrounding this ligand (Figure 18), in particular the segments Lys34-Phe46 (corresponding to the β5 strand) and His87-Ile90 (part of the β2-β3 loop), which interact with CaN at the contact region between its two subunits (Griffith et al., 1995; Kissinger et al., 1995). The rather small structural differences between FKBP38$^{35\text{-}153}$ and FKBP12 as well as the fact that no side-chains of FKBP38$^{35\text{-}153}$, with

the exception of Arg127, would overlap with the outer part of the bound FK506 ligand, are a clear indication that FKBP38$^{35\text{-}153}$ by itself cannot mimic the immunosuppressive FKBP12/FK506 complex. Hence, the structure of FKBP38$^{35\text{-}153}$ supports the observation that FKBP38 in fact cannot bind CaN in the absence of bound FK506.

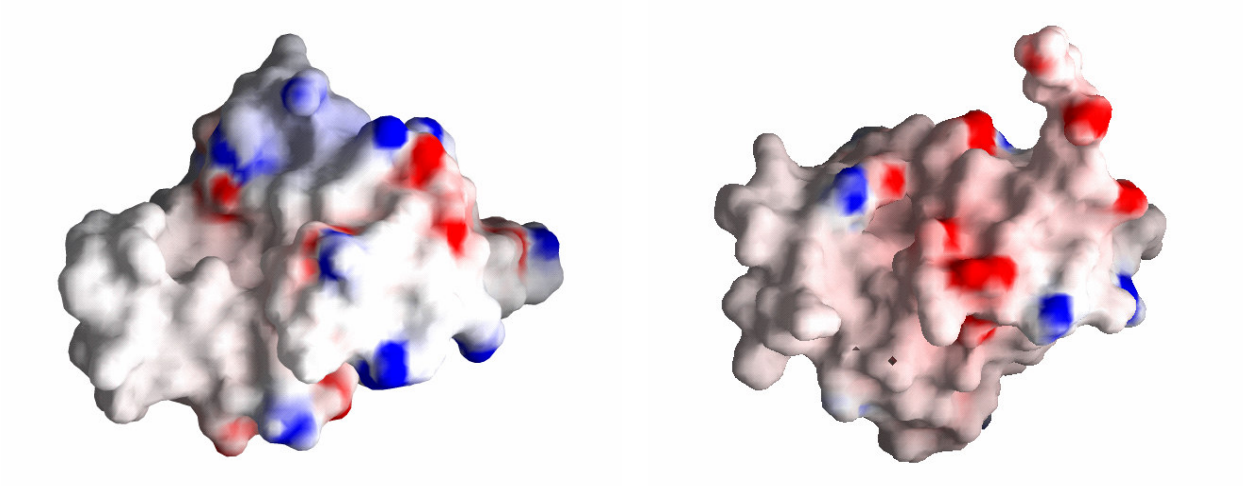

Figure 17. Surface potentials of FKBP12 (**left**) and FKBP38$^{35\text{-}153}$ (**right**). Both proteins are presented in the same orientation.

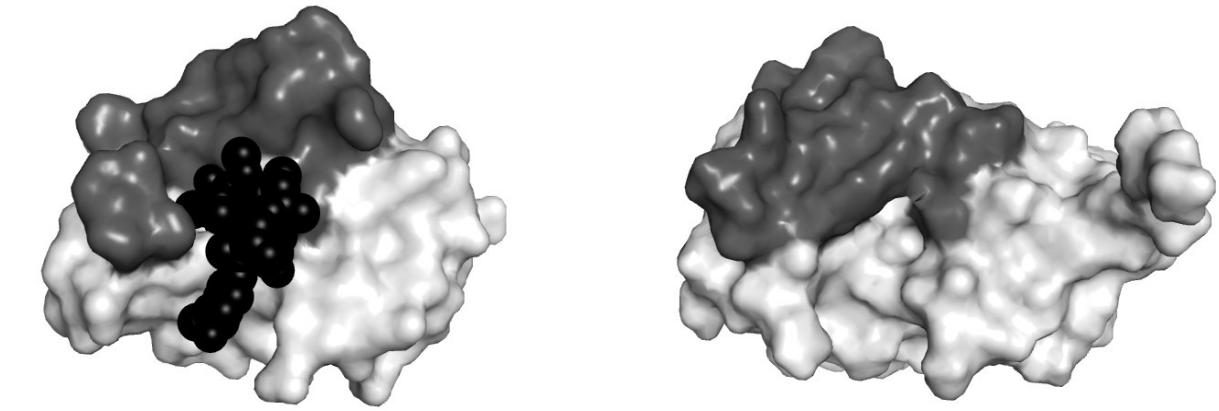

A **B**

Figure 18. (**A**) Molecular surface of the FKBP12/FK506 complex. The segments of FKBP12 involved in the interaction with CaN, i.e. Lys34-Phe46 and His87-Ile90, are colored in dark gray. The FK506 molecule is represented as black spheres. (**B**) Molecular surface of FKBP38$^{35\text{-}153}$, in the same orientation as the FKBP12/FK506 complex. The segments Thr78-L86 and Arg127-Tyr130, equivalent to those of FKBP12 interacting with CaN, are represented in dark gray.

3.3. Interaction of FKBP38$^{35\text{-}153}$ with Ca^{2+} and Mg^{2+}

During the study of the interaction between FKBP38$^{35\text{-}153}$ and both CaM forms (see section 3.4), the $^{1}H/^{15}N$-HSQC spectra of ^{15}N-labelled FKBP38$^{35\text{-}153}$ were collected under two different conditions, namely 20 mM NaH_2PO_4 (pH 6.8) for the study of the interaction with apo-CaM as well as 10 mM MES, 100 mM KCl and 6 mM $CaCl_2$ (pH 6.8) for the study of the interaction

with holo-CaM. The $^{1}H/^{15}N$-HSQC spectrum of FKBP38$^{35\text{-}153}$ does not change significantly with the buffer conditions, except for prominent shifts of the amide resonances in the segment comprising residues Leu90-Ile96, which forms the βC-α1 loop. As this part of the protein is essentially negatively charged due to the presence of the residues Asp92, Asp94 and Asp100 (Figure 19), these shift changes suggest the presence of an interaction site for calcium in this region of FKBP38$^{35\text{-}153}$.

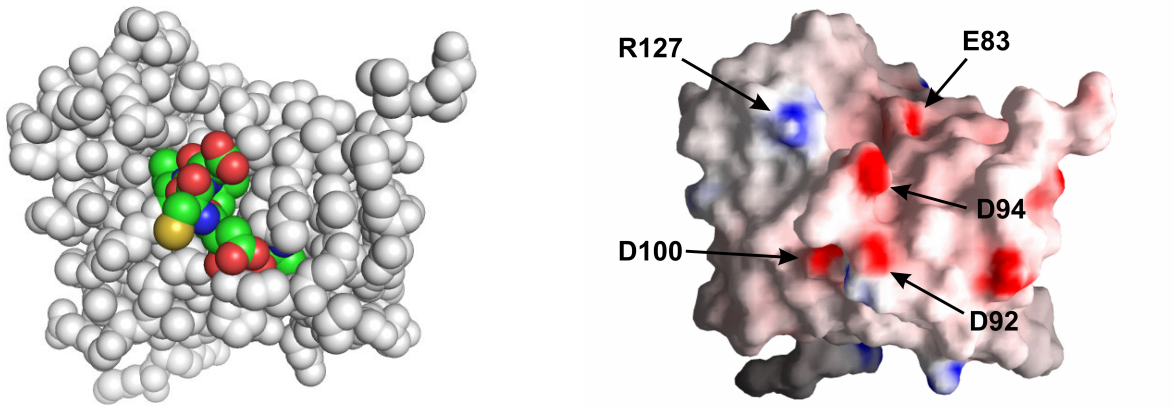

Figure 19. (**A**) Atomic model of FKBP38$^{35\text{-}153}$. The amino acids of the segment Leu90-Ile96, which were affected by the presence of Ca^{2+}, are colored according to atom type. (**B**) Potential energy surface of FKBP38$^{35\text{-}153}$ in the same orientation. Side-chains of acidic residues possibly relevant for the interaction with Ca^{2+}, as well as those of Glu83 and Arg127, are labelled.

The interaction with Ca^{2+} was confirmed by a titration of the protein (dissolved in a buffer consisting of 10 mM MES, 100 mM KCl, pH 6.8) with $CaCl_2$, which resulted in a shift of the same above-mentioned resonances in the $^{1}H/^{15}N$-HSQC spectrum during the course of the titration (Figure 20). For example, the H^N resonance of Asp94 experienced a chemical shift increase of 0.059 ppm upon Ca^{2+} addition and the N resonance of Val95 a decrease of 0.406 ppm. The sequence-specific chemical shift perturbations produced by the addition of Ca^{2+} are summarized in Figure 21A. As a control experiment, a ^{15}N-labelled sample of FKBP12 was titrated with an excess of $CaCl_2$, but no significant chemical shift perturbations were observed (Figure 21B). In fact, the highest chemical shift changes are 10-fold lower than those observed in FKBP38$^{35\text{-}153}$. This is a clear indication that FKBP12 does not interact with Ca^{2+}.

The interaction between FKBP38$^{35\text{-}153}$ and Ca^{2+} was also detected in the 1D ^{1}H-NMR spectrum of FKBP38$^{35\text{-}153}$, where the resonances belonging to H^N of Gly91 (displaying a very broad signal in the $^{1}H/^{15}N$-HSQC spectrum) and $H^{\gamma 2}$ of Val95 display noticeable chemical shift changes upon addition of Ca^{2+} (Figure 22). Another physiologically relevant ion, Mg^{2+}, was found to interact with FKBP38$^{35\text{-}153}$ in the same manner, as its addition to FKBP38$^{35\text{-}153}$ produces the same effects

as Ca^{2+} in the 1D ^{1}H-NMR spectrum of the protein (Figure 22).

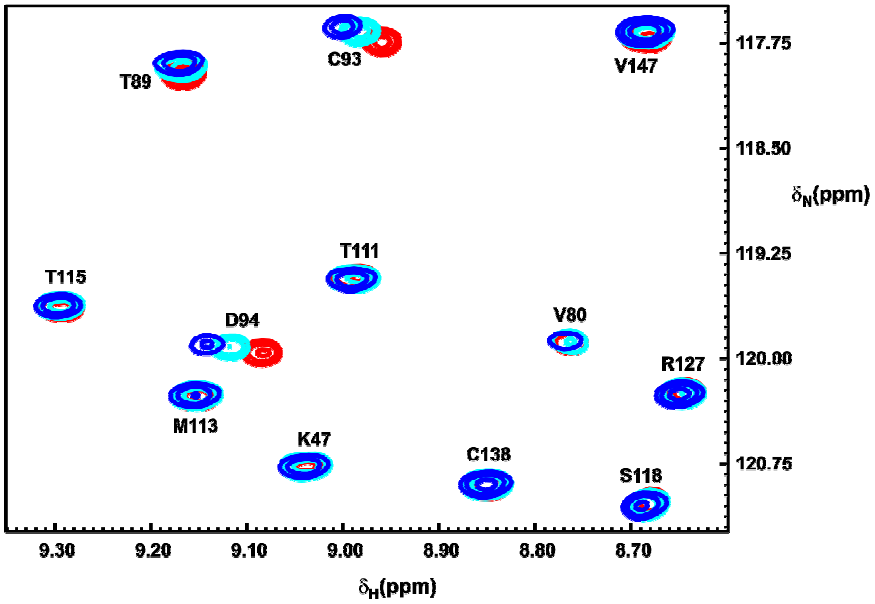

Figure 20. Superposition of a section from the $^{1}H/^{15}N$-HSQC spectrum of $FKBP38^{35-153}$, showing shifts of certain backbone amide resonances during the titration with Ca^{2+}. The spectra in red, cyan and blue correspond to Ca^{2+} concentrations of 0, 3.7 and 7.3 mM, respectively.

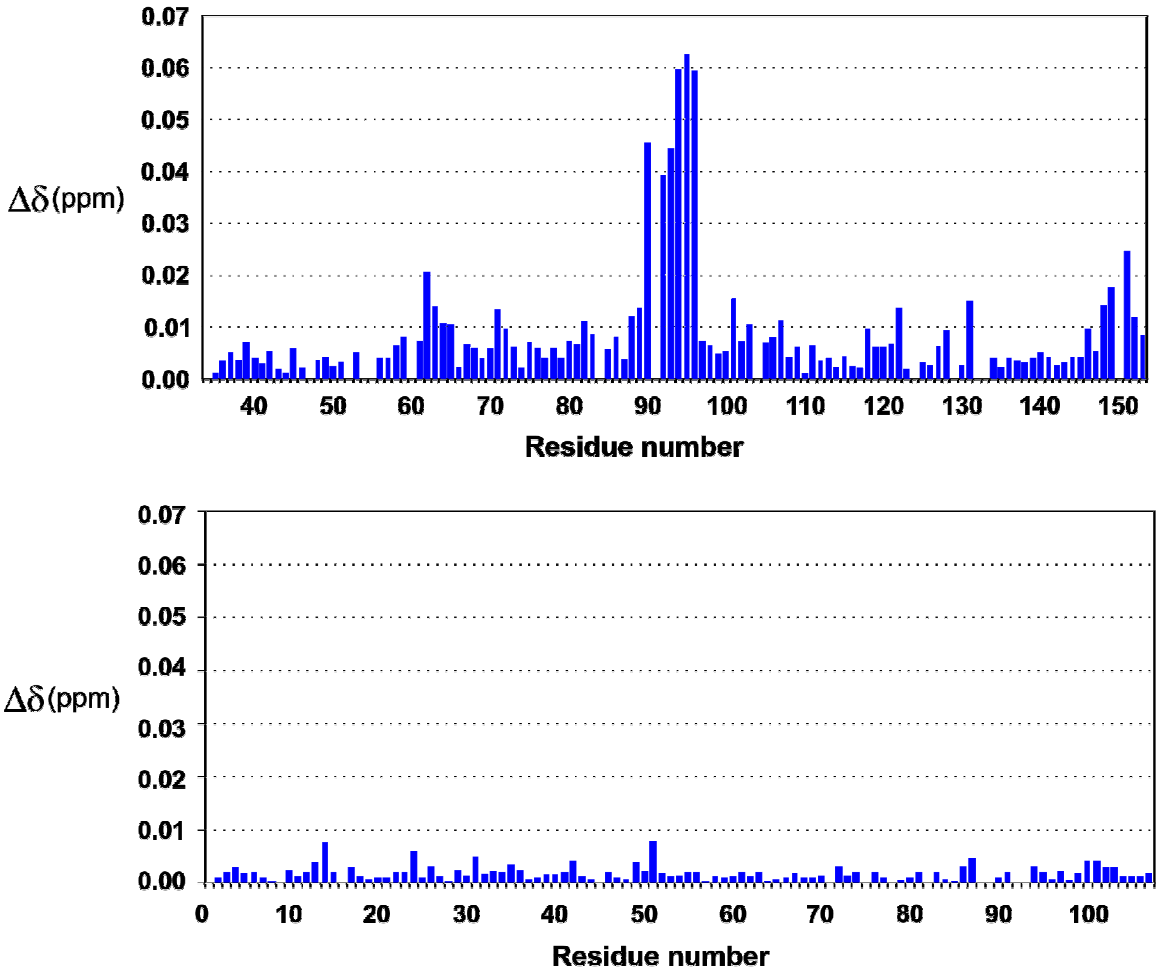

Figure 21. (**A**) Chemical shift perturbations produced by the addition of 7.3 mM $CaCl_2$ to a 0.4 mM solution of $FKBP38^{35-153}$. (**B**) Control experiment with FKBP12 under identical conditions.

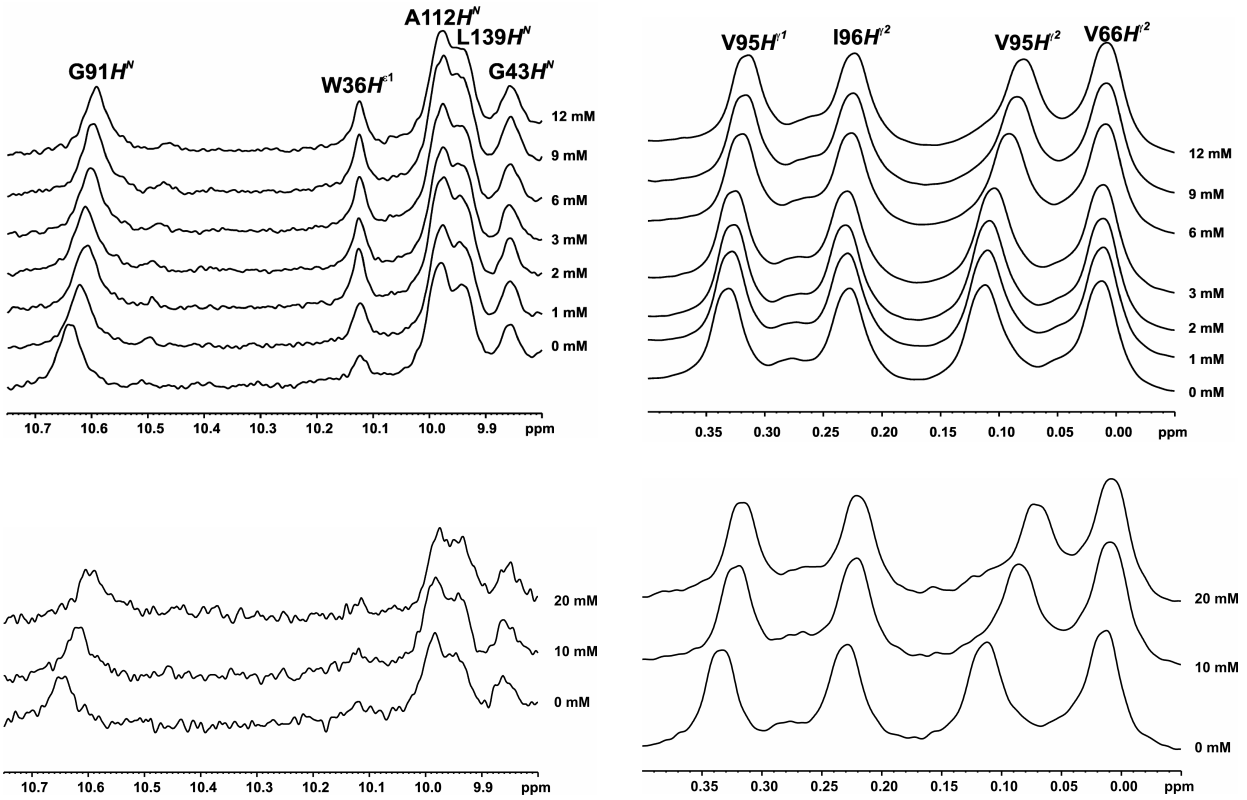

Figure 22. Sections from the 1D ^{1}H-NMR spectrum of FKBP38$^{35\text{-}153}$, showing the shift of certain amide (Gly91H^{N}, **left**) and methyl (V95H$^{\gamma 2}$, **right**) protons during the course of titration with either $CaCl_2$ (**upper panel**) or $MgCl_2$ (**lower panel**).

Although the chemical shift perturbation data indicated a surface-accessible region with 2 or 3 possible Ca^{2+}-coordinating groups (Asp92, Asp94 and Asp100) as interaction site, the precise structural arrangement between FKBP38$^{35\text{-}153}$ and the divalent cation could not be determined by NMR. The protein was therefore crystallized in a buffer containing $CaCl_2$. A high quality X-ray structure of FKBP38$^{35\text{-}153}$ was subsequently obtained with a resolution of 1.05 Å, but no Ca^{2+} ions were found to be bound to the protein. However, the negatively-charged side-chains of Asp92 and Asp94, both part of the loop that displayed chemical shift changes upon Ca^{2+} addition, showed hydrogen-bond contacts to the positively-charged guanidinium group of Arg34 from a neighboring FKBP38$^{35\text{-}153}$ molecule in the crystal (Figure 23). Apparently, this arrangement leads to an alternative charge compensation that could mimic the electrostatic interactions of the Asp92 and Asp94 side-chains with Ca^{2+}.

Fluorescence spectroscopy and isothermal titration calorimetry (ITC) experiments have also confirmed the interaction of Ca^{2+} and Mg^{2+} with FKBP38$^{35\text{-}153}$ (Dr. Frank Edlich, unpublished results). Fluorescence spectroscopy measurements showed a reduction of the fluorescence intensity of FKBP38$^{35\text{-}153}$ upon addition of either $CaCl_2$ or $MgCl_2$. Moreover, titrations with $CaCl_2$, $MgCl_2$ and KCl, carried out with fluorescence detection, clearly showed a higher binding

affinity of FKBP38$^{35\text{-}153}$ for Ca^{2+} than for Mg^{2+}, yet no detectable interactions with K^{+}. ITC experiments with Ca^{2+} and FKBP38$^{35\text{-}153}$ revealed the formation of a 1:1 complex, with a K_D of 17 ± 3 μM, which is close to the range of Ca^{2+} concentrations found in most cells (0.1 to 10 μM). This might allow in case of extremely high local Ca^{2+} concentrations - as for example after Ca^{2+} release by the endoplasmic reticulum - that this FKBP domain senses the Ca^{2+} stimuli. Certainly, the binding of Ca^{2+} to FKBP38$^{35\text{-}153}$ is rather weak, which explains why it was not observed in the X-ray structure. But the chemical shift perturbation experiments clearly demonstrate an interaction, which could implicate that - in addition to the CaM/Ca^{2+} regulation of FKBP38 - the interaction of Ca^{2+} itself with the FKBP domain of this protein might play a regulatory role in the activity of FKBP38.

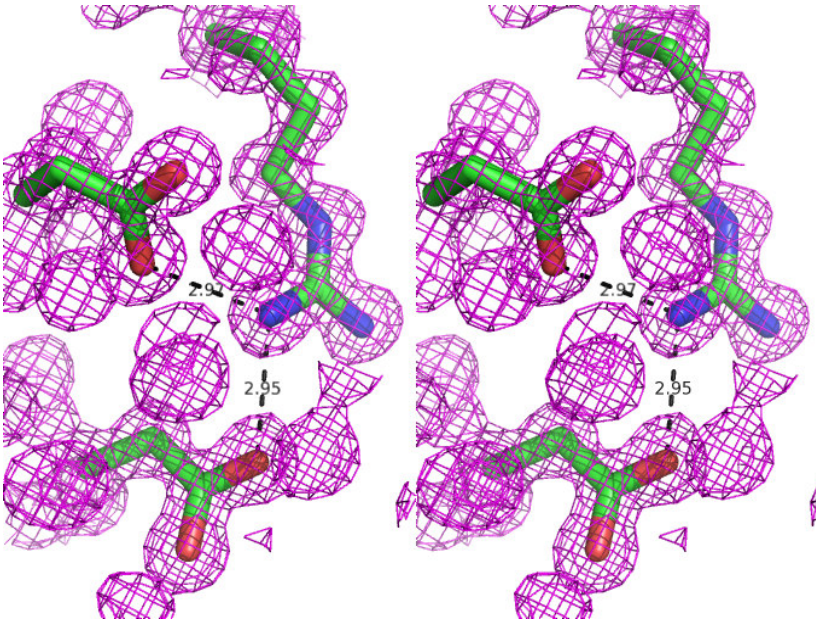

Figure 23. Section of the FKBP38$^{35\text{-}153}$ X-ray structure. Side-chain atoms are represented as stick models colored by atom type, and the electron densities are shown in magenta. The side-chains of residues Asp92 and Asp94 form hydrogen bonds to the side-chain of Arg34 that belong to an adjacent FKBP38$^{35\text{-}153}$ molecule in the crystal.

Based on the structure of FKBP38$^{35\text{-}153}$, two different explanations can be envisioned for the regulation of this domain by Ca^{2+}. First, a change in the net charge around the active site from -4 to -2 after Ca^{2+}-binding, which could affect considerably the binding of charged ligands such as polypeptide chains, probably leading to a negative regulation of the FKBP38 activity when it interacts with positively-charged ligands. On the other hand, it was already mentioned that salt-bridges connecting the side-chains of Asp94 and Glu83 with Arg127 can be formed in FKBP38, possibly leading to the stabilization of a "closed active site". The binding of Ca^{2+} to the side-chain of Asp94, in a manner similar to that shown in Figure 23, would destabilize these salt-bridges, probably leading to an opening of the active site and thus producing a positive regulation of the FKBP38 activity.

3.4. Interaction of FKBP38$^{35-153}$ with calmodulin

The most interesting feature of FKBP38 is its activation upon complex formation with CaM. In addition to the Ca^{2+}-dependent interaction of FKBP38 with CaM, which is due to the putative CaM-binding site located at the end of the TPR domain, a Ca^{2+}-independent interaction between the catalytic FKBP domain and CaM has been identified, which causes an activation of the FKBP domain (Edlich et al., in preparation).

In order to obtain structural information about the complex between FKBP38$^{35-153}$ and CaM, 2D $^{1}H/^{15}N$-HSQC spectra comparing the free and the complexed state of each protein were collected. Employing ^{15}N-labelled protein samples, changes in the chemical shift values of certain amide resonances, which occur as a result of the addition of a 3-fold excess of the non-labelled binding partner, reveal the residues involved in (or affected by) the complex formation.

Once these residues are determined, a docking calculation of the protein/protein complex can be performed, using the program HADDOCK (Dominguez et al., 2003). This program overcomes the hurdle posed by the lack of specific intermolecular distance restraints, as it transforms the residues at each contact surface into a set of Ambiguous Interaction Restraints (AIRs) that drives the docking calculation towards a final structure where the contact surfaces of both proteins face each other. The structures with the lowest intermolecular energies (i.e. the sum of van der Waals, electrostatic and AIR energy terms) are selected as output of the structure calculation. This docking approach is especially well suited for transient protein/protein interactions (like the ones presented here), where the collection of intermolecular NOEs can be extremely difficult or even impossible.

3.4.1. NMR assignments of the backbone amide resonances of apo- and holo-calmodulin

A reliable backbone amide resonance assignment is a fundamental precondition for a successful chemical shift perturbations study. For both forms of CaM, no previous resonance assignments under the conditions selected for the present study had been reported in the literature. However, ^{1}H, ^{13}C and ^{15}N resonance assignments of apo-CaM from *Xenopus laevis* (african frog) at 23 ºC and pH 6.3 (kindly provided by Dr. Ad Bax; ^{1}H and ^{15}N assignments reported by Tjandra et al., 1995) and of holo-CaM from *Drosophila melanogaster* at 47 ºC and pH 6.3 (Ikura et al., 1990) were available. These assignments could be used as starting points to determine the chemical shifts of the amide resonances of apo- and holo-CaM at the here applied conditions. This was achieved with ^{15}N-labelled protein samples by using the classical assignment strategy (Wüthrich,

1986).

In the case of apo-CaM, the relatively small differences in the experimental conditions and the fact that the human CaM is 100% identical to that of *Xenopus laevis* facilitated the assignment of the amide resonances, resulting in a set of chemical shifts very similar to the one reported by Tjandra (Table 5, Figure 24). A systematic ~0.4 ppm up-field shift of the ^{15}N resonances was found, possibly arising from (i) the different reference systems used for the chemical shifts and (ii) the difference in temperature. Only the resonances belonging to the segment Asp22-Ile27 were not found in the present spectra, due to their special dynamic behavior (Tjandra et al., 1995). Additional resonances arose from the additionally introduced C-terminal His-tag used. The close agreement of this apo-CaM assignment with the one previously reported by Tjandra furthermore confirms that CaM is free of Ca^{2+} under the experimental conditions chosen in the present study.

Table 5. ^{1}H and ^{15}N backbone amide resonance assignments (in ppm) of apo-CaM at 298 K and pH 6.8.

AA	H^N	***N***	***AA***	H^N	***N***	***AA***	H^N	***N***
Ala1	n.a.	n.a.	Met51	7.97	119.5	Ser101	8.94	117.5
Asp2	n.a.	n.a.	Ile52	8.49	118.8	Ala102	8.78	124.8
Gln3	8.20	118.7	Asn53	8.30	117.7	Ala103	8.28	119.4
Leu4	8.33	122.2	Glu54	7.59	117.6	Glu104	7.75	120.7
Thr5	8.79	113.2	Val55	7.67	113.3	Leu105	8.21	120.8
Glu6	9.04	120.4	Asp56	8.47	122.4	Arg106	8.07	117. 5
Glu7	8.76	119.6	Ala57	8.14	125.4	His107	7.77	119.4
Gln8	7.75	120.8	Asp58	8.43	114.9	Val108	8.12	119.9
Ile9	8.25	118.7	Gly59	7.91	109.2	Met109	8.14	115.4
Ala10	7.93	120.6	Asn60	9.20	120.0	Thr110	7.93	110.9
Glu11	7.81	120.5	Gly61	10.08	110.7	Asn111	7.62	120.0
Phe12	8.83	120.6	Thr62	7.59	110.9	Leu112	7.73	120.3
Lys13	9.26	121.8	Ile63	8.97	119.5	Gly113	8.31	108.5
Glu14	8.08	120.7	Asp64	8.58	125.0	Glu114	8.08	120.5
Ala15	7.67	121.1	Phe65	8.67	118.9	Lys115	8.25	120.7
Phe16	8.56	118.1	Pro66	-	n.a.	Leu116	7.82	121.5
Ser17	8.47	111.4	Glu67	8.13	117.9	Thr117	9.10	113.7
Leu18	7.39	121.4	Phe68	8.49	122.8	Asp118	8.85	121.2
Phe19	7.39	114.8	Leu69	8.49	119.0	Glu119	8.60	118.3
Asp20	7.33	122.8	Thr70	7.75	115.8	Glu120	7.83	120.8
Lys21	8.02	123.7	Met71	7.74	121.6	Val121	8.21	120.8
Asp22	n.a.	n.a.	Met72	8.03	117.8	Asp122	8.37	119.4
Gly23	n.a.	n.a.	Ala73	8.31	121.4	Glu123	7.93	119.4
Asp24	n.a.	n.a.	Arg74	7.49	117.1	Met124	7.87	118.6
Gly25	n.a.	n.a.	Lys75	7.74	118.5	Ile125	8.33	118.4
Thr26	n.a.	n.a.	Met76	7.97	118.3	Arg126	7.97	119.5
Ile27	n.a.	n.a.	Lys77	7.77	121.0	Glu127	7.89	117.5
Thr28	8.32	110.9	Asp78	8.36	122.4	Ala128	7.64	121.4
Thr29	8.33	112.7	Thr79	8.17	115.3	Asp129	8.35	120.1
Lys30	7.66	119.2	Asp80	8.47	123.4	Ile130	7.83	121.4
Glu31	7.53	117.8	Ser81	8.44	117.5	Asp131	8.63	124.6

Leu32	7.38	121.1	Glu82	8.43	122.1	Gly132	8.39	108.6
Gly33	8.82	105.8	Glu83	8.15	118.8	Asp133	8.33	119.4
Thr34	7.53	118.4	Glu84	8.02	119.4	Gly134	8.60	110.1
Val35	7.96	123.0	Ile85	7.96	120.7	Gln135	8.34	119.6
Met36	8.47	118.9	Arg86	8.37	119.7	Val136	9.46	120.0
Arg37	8.52	119.6	Glu87	8.41	117.2	Asn137	8.86	125.7
Ser38	8.11	119.3	Ala88	7.55	121.6	Tyr138	7.88	118.7
Leu39	7.34	121.5	Phe89	7.56	114.6	Glu139	8.45	120.7
Gly40	7.93	107.4	Arg90	8.22	118.2	Glu140	7.90	119.7
Gln41	7.78	118.1	Val91	7.21	116.9	Phe141	8.03	117.2
Asn42	8.70	116.9	Phe92	7.35	116.0	Val142	8.13	118.2
Pro43	-	n.a.	Asp93	7.85	121.9	Gln143	7.87	118.1
Thr44	8.81	113.6	Lys94	8.33	124.4	Met144	8.21	125.7
Glu45	8.87	120.7	Asp95	8.67	116.2	Met145	7.98	119.4
Ala46	8.35	121.3	Gly96	7.96	110.6	Thr146	8.38	115.2
Glu47	7.76	119.2	Asn97	9.01	119.2	Ala147	7.59	123.1
Leu48	8.36	120.4	Gly98	10.14	111.0	Lys148	7.77	117.9
Gln49	8.07	117.8	Tyr99	7.90	118.7	Leu149	8.02	119.1
Asp50	7.86	119.2	Ile100	8.61	113.3	Glu150	n.a.	n.a.
						His151-His156	8.18	125.4

n.a. Not assigned

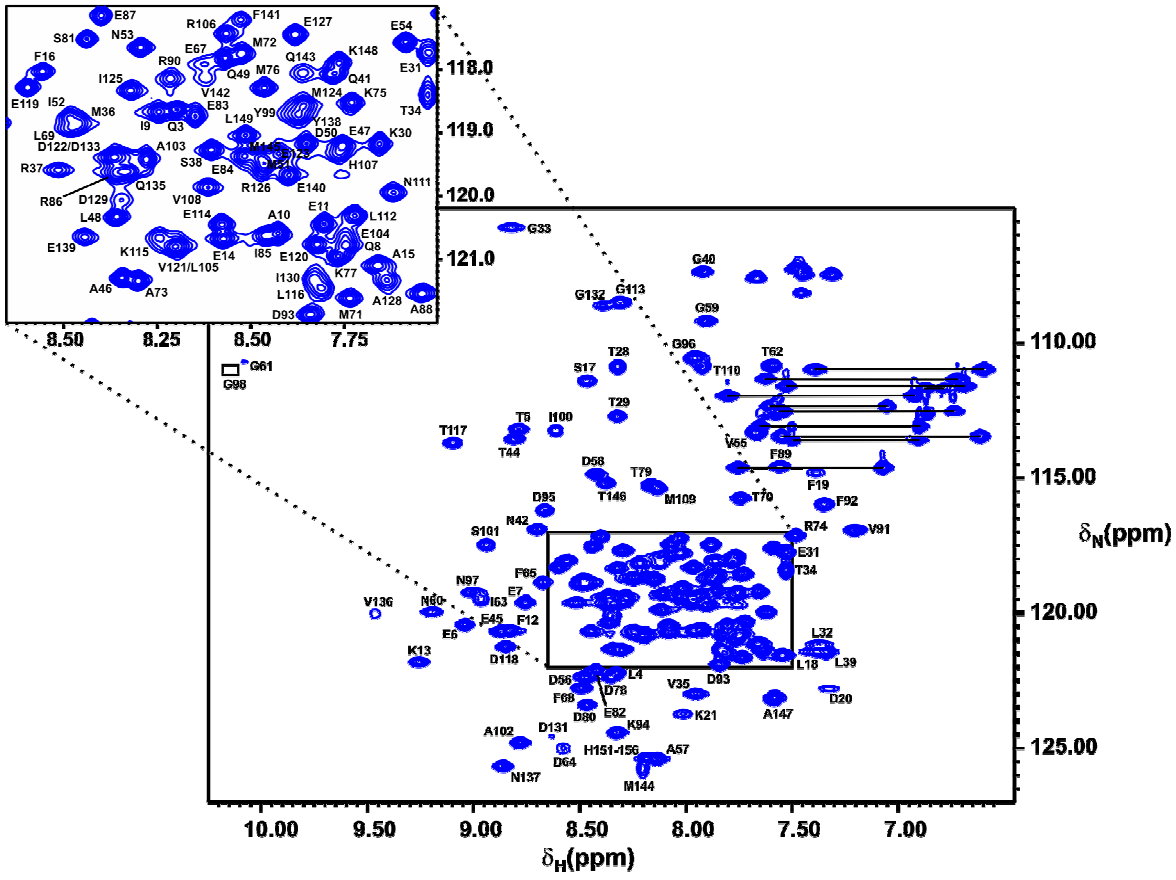

Figure 24. Two-dimensional $^{1}H/^{15}N$-HSQC spectrum of apo-CaM recorded at 500.13 MHz. The sequence-specific assignment of the backbone amide resonances is indicated. Boxes mark signals that appear below the plot level.

In case of the holo-CaM assignment, the combination of (i) a larger temperature difference, (ii) the presence of three amino-acids substitutions (Y99F, D129N and Q143T) and (iii) the presence

of the above-mentioned additional His-tag produced some major chemical shift differences to the previous reported assignment (Ikura et al., 1990). Nevertheless, nearly all backbone amide resonances could be assigned (Table 6, Figure 25).

Table 6. ^{1}H and ^{15}N resonance assignments (in ppm) of holo-CaM at 298 K and pH 6.8.

AA	***H^N***	***N***	***H^a***	***Other H***	***AA***	***H^N***	***N***	***H^a***	***Other H***
Ala1	n.a.	n.a.	n.a.	n.a.	Lys77	121.0	7.89	4.34	1.87, 1.75, 1.47
Asp2	n.a.	n.a.	n.a.	n.a.	Asp78	122.0	8.36	4.73	2.73
Gln3	119.8	8.37	4.41	2.00, 2.08, 2.36	Thr79	114.7	8.14	4.32	4.75, 1.22
Leu4	123.3	8.36	4.70	1.75, 1.53	Asp80	123.4	8.48	4.74	2.78
Thr5	113.3	8.80	4.47	1.36	Ser81	117.6	8.50	4.44	4.00
Glu6	120.5	9.08	3.99	2.08, 2.41	Glu82	122.4	8.45	4.19	2.14, 2.34
Glu7	119.7	8.79	4.08	2.31, 2.01	Glu83	119.9	8.26	4.09	2.11, 2.38
Gln8	120.6	7.80	3.88	2.35	Glu84	119.1	8.23	4.18	2.17, 2.39
Ile9	119.7	8.42	3.71	n.a.	Ile85	122.1	8.05	3.98	2.15, 1.10
Ala10	121.3	8.02	4.15	1.53	Arg86	121.9	8.44	4.20	2.03, 1.55, 6.58
Glu11	120.0	7.83	4.17	2.11, 1.99, 2.41	Glu87	119.0	8.21	4.21	2.12, 2.38
Phe12	120.4	8.65	5.05	3.49	Ala88	122.0	8.00	4.23	1.79
Lys13	123.6	9.24	4.02	1.93	Phe89	118.5	8.52	3.26	7.30, 7.01, 6.58
Glu14	120.5	7.83	4.17	2.26, 2.36	Arg90	115.7	7.68	3.92	1.97, 1.70
Ala15	122.7	8.02	4.33	1.96	Val91	118.1	7.72	3.52	2.07, 0.97, 0.57
Phe16	119.4	8.86	3.30	2.96	Phe92	116.5	7.76	4.30	2.68, 7.40
Ser17	112.7	7.99	4.14	n.a.	Asp93	118.3	7.86	4.60	2.42
Leu18	121.0	7.47	4.02	1.74, 1.57	Lys94	126.0	7.71	3.93	1.88
Phe19	115.3	7.35	4.27	2.68	Asp95	114.0	8.18	4.61	3.08, 2.67
Asp20	118.1	7.77	4.58	2.39	Gly96	109.4	7.79	3.82	
Lys21	124.4	7.74	3.99	1.89	Asn97	119.3	8.29	4.68	3.41, 2.68
Asp22	114.2	8.12	4.62	3.08, 2.65	Gly98	113.2	10.64	4.04, 3.44	
Gly23	109.5	7.74	3.87		Tyr99	115.8	7.61	5.14	2.51
Asp24	120.8	8.43	4.56	3.07, 2.47	Ile100	127.3	10.05	4.96	1.95, 0.95
Gly25	113.4	10.62	4.38, 3.72		Ser101	123.9	8.96	4.84	
Thr26	112.9	8.12	5.36	3.88, 1.05	Ala102	123.0	9.20	3.93	1.50
Ile27	125.9	9.70	n.a.	0.35	Ala103	118.6	8.29	4.03	1.43
Thr28	116.1	8.48	4.87	1.31	Glu104	119.3	7.83	4.15	2.54
Thr29	112.8	9.07	3.81	4.73	Leu105	121.6	8.79	4.09	1.65, 1.89
Lys30	120.9	7.71	4.16	1.84	Arg106	118.1	8.51	3.83	n.a.
Glu31	121.3	7.69	4.10	2.41	His107	118.4	7.74	4.38	3.36
Leu32	120.9	8.65	4.12	n.a.	Val108	119.6	7.91	3.30	2.05, 0.83, 0.51
Gly33	105.8	8.70	3.99, 3.56		Met109	116.3	8.23	4.34	2.17
Thr34	118.2	7.91	3.94	4.30, 1.27	Thr110	115.8	8.21	4.16	4.26, 1.28
Val35	122.3	7.67	3.50	1.99, 0.67, 0.44	Asn111	122.5	7.94	4.53	2.84
Met36	118.7	8.50	4.13	2.70	Leu112	118.8	7.82	4.34	1.81, 1.70, 0.82

Arg37	119.3	8.57	4.83	1.93	Gly113	107.0	7.89	4.24, 3.77	
Ser38	119.0	7.96	4.43	4.14	Glu114	120.3	7.93	4.45	1.73, 2.01, 2.16
Leu39	120.8	7.39	4.54	1.87	Lys115	124.5	8.65	4.40	1.71, 1.36
Gly40	107.1	7.92	4.27, 3.80		Leu116	125.0	8.15	4.80	1.51, 0.81
Gln41	118.6	7.82	4.50	2.22, 1.66	Thr117	114.8	9.30	4.48	1.37
Asn42	116.5	8.76	5.22	2.81, 2.53	Asp118	121.3	8.95	4.22	2.58, 2.75
Pro43	n.a.	-	n.a.	n.a.	Glu119	119.4	8.74	4.12	2.05, 2.38
Thr44	113.3	8.81	4.47	n.a.	Glu120	120.8	7.81	4.03	1.90, 2.40
Glu45	120.8	8.86	4.00	2.36, 2.07	Val121	121.6	8.14	3.61	2.24, 0.98
Ala46	121.0	8.32	4.15	1.42	Asp122	119.9	8.06	4.36	2.78, 2.66
Glu47	118.9	7.74	4.04	2.34, 1.89	Glu123	119.6	7.90	4.10	2.13
Leu48	120.7	8.25	4.11	1.32, 0.89	Met124	119.8	7.85	4.05	2.06, 2.30
Gln49	118.5	8.22	3.86	2.19, 2.48	Ile125	118.7	7.95	3.53	2.14, 0.76
Asp50	120.1	8.12	4.45	2.75	Arg126	118.4	8.09	4.02	1.88, 1.63
Met51	119.5	7.89	4.07	2.31, 2.03	Glu127	116.2	8.01	4.00	2.06, 2.27, 2.43
Ile52	118.6	7.80	3.52	1.95, 0.72	Ala128	119.0	7.45	4.39	1.45
Asn53	117.8	8.59	4.39	2.92	Asp129	117.4	7.79	4.55	2.87, 2.54
Glu54	116.6	7.60	4.07	2.09, 2.20, 2.45	Ile130	127.7	8.42	3.94	2.03, 0.97, -0.32
Val55	108.8	7.30	4.50	0.89	Asp131	116.7	8.30	4.59	3.10, 2.67
Asp56	122.1	7.75	4.69	2.78	Gly132	108.7	7.61	3.98, 3.86	
Ala57	131.4	8.46	4.21	1.54	Asp133	120.9	8.36	4.51	2.98, 2.51
Asp58	113.9	8.18	4.66	3.04, 2.67	Gly134	113.1	10.40	4.07, 3.44	
Gly59	108.6	7.63	3.93, 3.83		Gln135	115.8	7.98	4.85	1.94, 1.68
Asn60	118.6	8.16	4.70	2.69	Val136	125.2	9.11	5.25	2.39, 1.28, 0.96
Gly61	113.3	10.62	4.38, 3.72		Asn137	128.8	9.49	5.20	n.a.
Thr62	109.4	7.70	4.80	n.a.	Tyr138	118.5	8.51	4.13	6.32
Ile63	123.6	8.96	5.16	n.a.	Glu139	118.6	8.18	3.70	2.11, 2.37
Asp64	128.0	8.83	5.40	2.58, 2.90	Glu140	120.0	8.81	4.09	2.57
Phe65	118.9	8.95	4.00	3.14, 2.88, 7.25, 7.04, 6.76	Phe141	124.4	9.08	4.03	3.47, 3.26, 7.00
Pro66	n.a.	-	n.a.	n.a.	Val142	119.9	8.60	3.20	1.89, 0.78, 0.58
Glu67	117.8	8.00	4.12	2.55, 2.03	Gln143	118.7	7.49	3.98	2.15, 2.46
Phe68	123.7	8.86	3.97	3.50, 3.20, 6.71, 6.98, 7.19	Met144	119.8	8.03	4.09	2.09, 2.32
Leu69	119.0	8.39	3.36	1.61, 1.19, 1.06, 0.66	Met145	116.5	8.34	4.23	1.65
Thr70	115.9	7.55	3.83	4.35, 1.23	Thr146	114.7	7.99	3.91	4.19, 1.18
Met71	122.0	7.81	3.80	2.17	Ala147	122.9	7.70	4.24	1.43
Met72	116.9	8.11	4.04	1.86, 1.44	Lys148	117.0	7.72	4.23	1.86, 1.44
Ala73	122.5	8.22	4.11	1.42	Leu149	119.4	7.96	4.22	1.71, 1.57, 0.83
Arg74	117.0	7.59	4.10	1.84, 1.68	Glu150	119.7	7.99	4.12	1.97, 2.20
Lys75	118.8	7.67	4.24	1.84, 1.48	His151	117.6	8.13	4.54	3.12

Met76	118.8	7.89	4.39	2.13, 2.68	His152-His156	125.4	8.18	4.49	3.10, 3.19

n.a. Not assigned

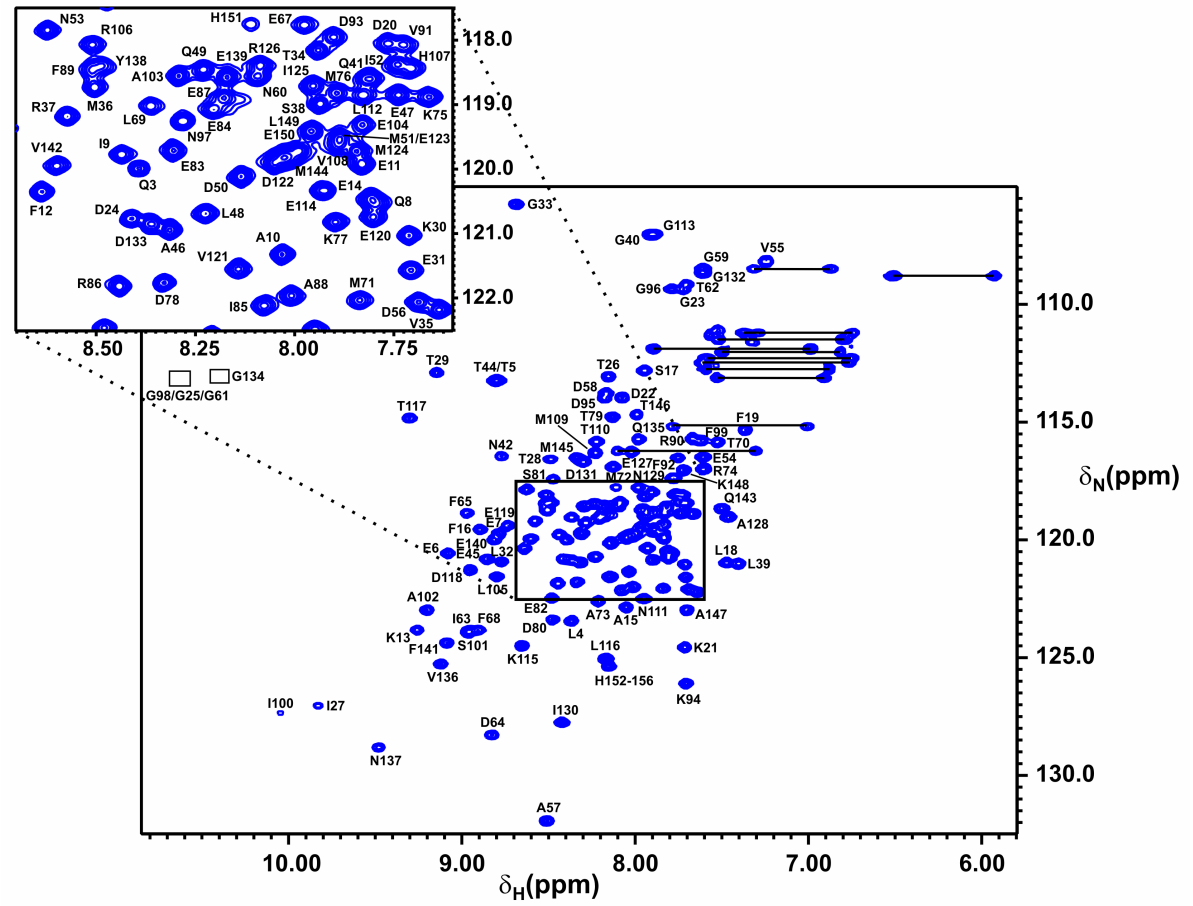

Figure 25. Two-dimensional $^{1}H/^{15}N$-HSQC spectrum of holo-CaM recorded at 500.13 MHz. The sequence-specific assignment of the amide resonances is indicated. Boxes mark signals that appear below the plot level.

3.4.2. Interaction of FKBP38$^{35-153}$ with apo-calmodulin

Although the non-labelled binding partner was added in excess to shift the equilibrium toward the complex, the chemical shift perturbations of the amide resonances of ^{15}N-labelled FKBP38$^{35-153}$ were rather small upon addition of apo-CaM (Figure 26), as expected for a complex with a relatively low binding constant. The calculated combined chemical shift perturbations Δδ (Figure 27) exhibited an average value of 0.004 ppm, whereas the highest chemical shift perturbation (Glu35) reached 0.026 ppm. Several amide resonances were affected by more than 0.005 ppm, such as the segments Leu74-Gln81 (with the exception of Thr78), which comprises the βC-βD loop, and Ser128-Ile131 (located in the N-terminal part of the long βE-βF loop), as well as the residues His69 and Gln71, which are both located at the outer surface of the βC strand. The majority of these residues form a well-defined surface centered at the βC-βD loop (Figure 28). The most pronounced of these chemical shift changes, however, were found close to the N-

terminus. In particular, the above-mentioned Glu35 together with Trp36, Leu37 and Lys48 seem to be affected by a small change in the orientation of the aromatic Trp36 side-chain. This conclusion is supported by the observation of a 4 nm red-shift and an 8.5% loss of intensity in the fluorescence spectrum of FKBP38$^{35\text{-}153}$ upon binding to apo-CaM (Edlich et al., in preparation), which is consistent with a change in the local environment of the Trp36 indol ring (the only tryptophan in FKBP38$^{35\text{-}153}$).

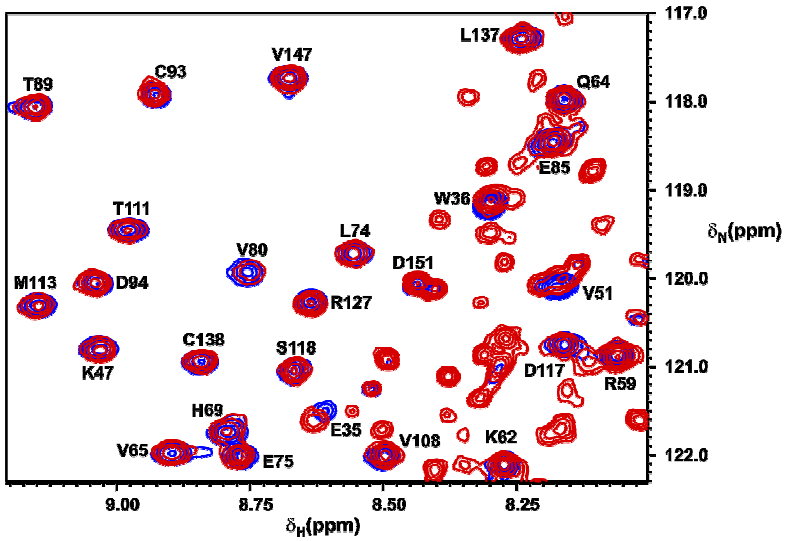

Figure 26. Section from the $^{1}H/^{15}N$-HSQC spectrum of ^{15}N-labelled FKBP38$^{35\text{-}153}$, showing the changes caused in the backbone resonances by the complex formation with apo-CaM. The blue signals correspond to the free form of FKBP38$^{35\text{-}153}$, while the red signals correspond to the FKBP38$^{35\text{-}153}$/apo-CaM complex. Additional small sharp signals in the complex spectrum are due to denatured FKBP$^{38\text{-}153}$.

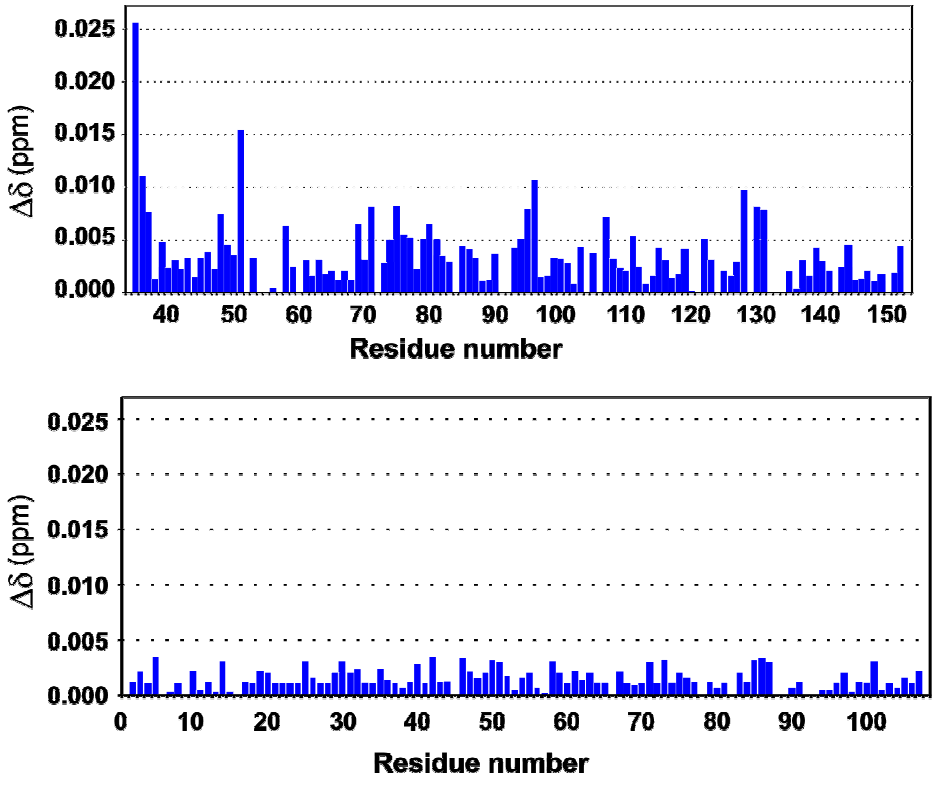

Figure 27. (**A**) Overview of the combined chemical shift changes (Δδ) observed for ^{15}N-labelled FKBP38$^{35\text{-}153}$ upon addition of a 3-fold molar excess of apo-CaM. (**B**) Control experiment with FKBP12 under similar conditions.

The residues Asp94, Val95, Ile96 and Tyr122, also displaying considerable chemical shift changes, are located in the contact region between the loops βE-βF and βD-α1. Most of them (with exception of Asp94) are not solvent accessible and therefore unlikely to be involved in the direct interaction with apo-CaM. These chemical shift perturbations could be attributed to a secondary binding effect, presumably as a result of a small rearrangement of the long βE-βF loop, which is seemingly directly involved in the interaction (see above). The chemical shift changes observed in the residues Ser58 and Asp107, located at the opposite side of the protein, are most likely secondary effects as well.

Hence, the contact surface thus derived is centered at the βC-βD loop, also comprising parts of the extended βE-βF loop (which blocks the access to the binding site) and the external side of the β-sheet. This result may provide an explanation for the observed activation of this FKBP domain upon complex formation with CaM (Edlich et al., in preparation), as (i) the active site does not seem to be occupied by apo-CaM and (ii) the interaction with the βE-βF loop could produce a change in its conformation that results in an opening of the active site. The secondary effects observed at the βD-α1 loop, also bordering the active site, support the last hypothesis.

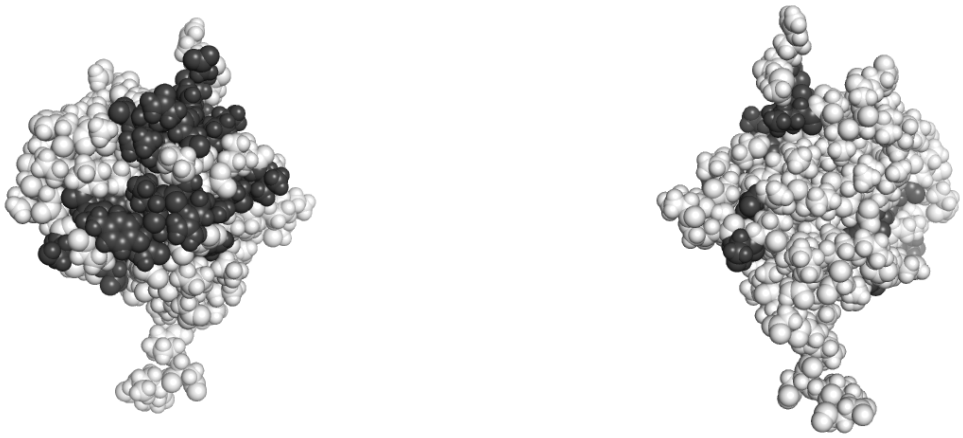

Figure 28. Atomic model of FKBP38$^{35\text{-}153}$. The residues affected by the interaction with apo-CaM are shown in dark gray.

The complex formation of ^{15}N-labelled apo-CaM with FKBP38$^{35\text{-}153}$ produced more pronounced chemical shift perturbations (Figure 29) than the reverse experiment. More precisely, the calculated combined chemical shift perturbations Δδ (Figure 30) exhibit an average value of 0.009 ppm, more than twice as that observed for FKBP38$^{35\text{-}153}$, while the highest chemical shift perturbation of 0.054 ppm was found for Ile63. The most pronounced chemical shift perturbations (i.e. those higher than 0.02 ppm) were all observed in the N-terminal domain of apo-CaM, especially in the segment Asn60-Asp64, which is part of the central loop of the second EF-hand motif (Figure 31). Furthermore, the resonances that correspond to the segment

comprising residues Asp22-Ile27, which is part of the central loop of the first EF-hand motif, were observed only in the complexed form (Figures 29 and 30), indicating a change in the backbone dynamics of these resonances as a result of the binding process. This may be explained by a reduction of (i) the backbone dynamics or (ii) the amide hydrogen exchange rate of these residues upon binding to FKBP38$^{35\text{-}153}$. Increased backbone dynamics within the segment Lys21-Gly25 (characterized by higher than normal amplitudes for the rapid internal motions of the backbone atoms, $S^2 < 0.8$) as well as a fast amide hydrogen exchange ($\tau_{exch} < 200$ s) were already reported for these residues based on NMR relaxation studies of apo-CaM (Tjandra et al., 1995; Kuboniwa et al., 1995). The interaction of the first EF-hand motif with FKBP38$^{35\text{-}153}$ is corroborated by the observation of considerable chemical shift perturbations of other signals that belong to this loop, namely Lys21 and Thr29. Interestingly, the affected central loops of both EF-hand motifs are spatially very close; in fact, parts of them (Thr62-Ile63 and Thr26-Ile27) even form a small antiparallel β-sheet.

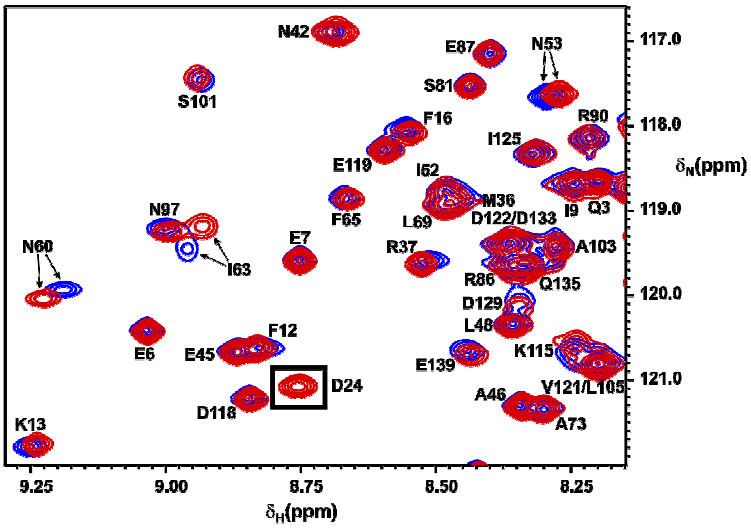

Figure 29. Section from the $^{1}H/^{15}N$-HSQC spectrum of ^{15}N-labelled apo-CaM, showing the changes in the backbone resonances caused by the complex formation with FKBP38$^{35\text{-}153}$. The blue signals correspond to the free form of apo-CaM, while the red signals correspond to the FKBP38$^{35\text{-}153}$/apo-CaM complex. The resonance belonging to Asp24, shown in a black box, is visible only in the spectrum of the FKBP38$^{35\text{-}153}$/apo-CaM complex.

Other residues of the N-terminal apo-CaM domain also showed significant chemical shift perturbations upon complex formation with FKBP38$^{35\text{-}153}$, in particular Ser17, Phe19, Thr34, Asn53 and Ala57, which are located in the helices A (Ser17 and Phe19), B (Thr34) and C (Asn53 and Ala57), respectively, and thus fairly close to the two loops affected by the interaction with FKBP38$^{35\text{-}153}$. Nevertheless, these residues apparently play only a minor role (or even none) in the interaction, since they are located in peripheral positions at the protein surface compared to the rest of the affected amino acids. Hence, the region involved in the interaction with FKBP38$^{35\text{-}153}$ should be centered at the central loops of both EF-hand motifs of the N-terminal apo-CaM domain.

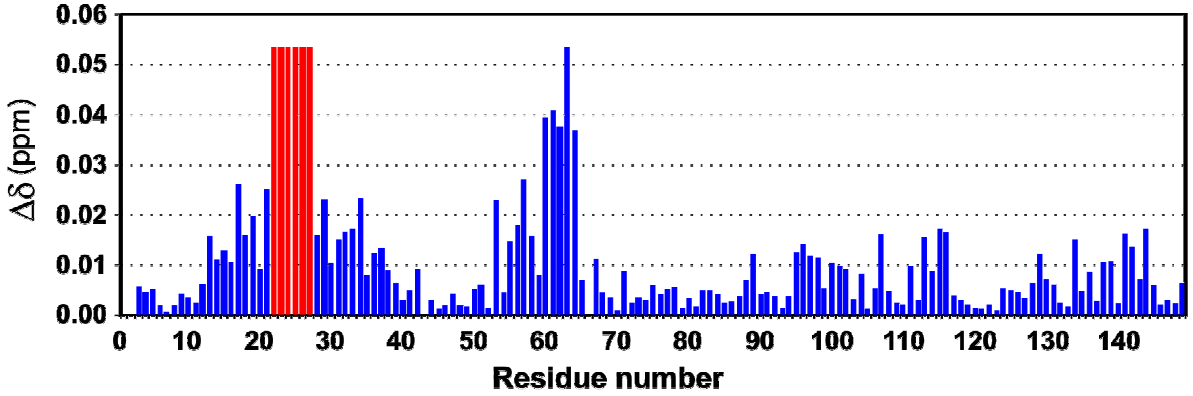

Figure 30. Overview of the combined chemical shift changes (Δδ) observed for ^{15}N-labelled apo-CaM upon addition of a 3-fold molar excess of FKBP38$^{35\text{-}153}$. Residues showing changes in the backbone dynamics (i.e. signals observed only in the complexed form) were arbitrarily assigned with the maximal chemical shift perturbation value (represented by red bars).

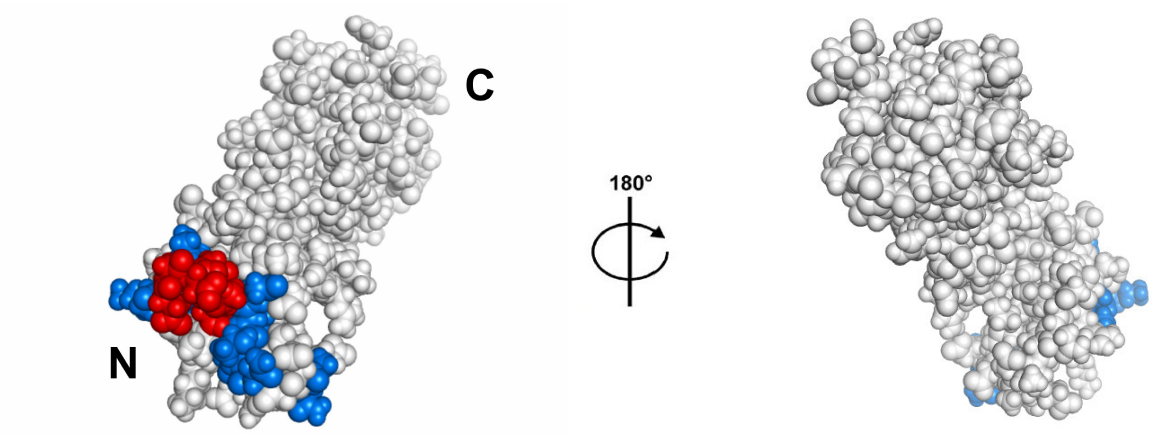

Figure 31. Atomic model of apo-CaM, showing the surface interacting with FKBP38$^{35\text{-}153}$. Residues displaying chemical shift perturbations higher than 0.02 ppm after addition of FKBP38$^{35\text{-}153}$ are colored in blue. The residues of the segment Asp22-Ile27, which experience a change in backbone dynamics upon complex formation, are highlighted in red.

This interaction between the N-terminal domains of FKBP38 and CaM is in good agreement with recently performed studies (Edlich et al., in preparation), which showed that the CaM N-terminal domain (CaM$^{1\text{-}75}$) is sufficient to (i) increase the PPIase activity of FKBP38$^{35\text{-}153}$ and (ii) to activate FKBP38 for its interaction with Bcl-2 independently of the presence or absence of Ca^{2+}.

A comparison of the amino acid sequences of both CaM domains (Figure 32A) provides an explanation for their different affinity for FKBP38$^{35\text{-}153}$. In the N-terminal CaM domain, the side-chains of residues Thr26 and Thr62 form the outer part of the short β-sheet that connects both EF-hand loops. In the C-terminal CaM domain, on the other hand, the corresponding positions are occupied by the more bulky side-chains of Tyr99 and Gln135. These variations thus produce different molecular surfaces in this region of the CaM domains (Figure 32B): (i) in the N-terminal domain a surface with a small cavity, capable to interact with FKBP38$^{35\text{-}153}$, and (ii) in

the C-terminal domain a surface lacking this cavity, apparently rendering it unsuitable for the interaction with FKBP38$^{35\text{-}153}$.

```
Nterm    IAEFKEAFSLFDKDGDGTITTKELGTVMRSLGQNPTEAELQDMINEVDADGN
Cterm    EEEIREAFRVFDKDGNGYISAAELRHVMTNLGEKLTDEEVDEMIREADIDGD

Nterm    GTIDFPEFLTMMARK
Cterm    GQVNYEEFVQMMTAK
```

A

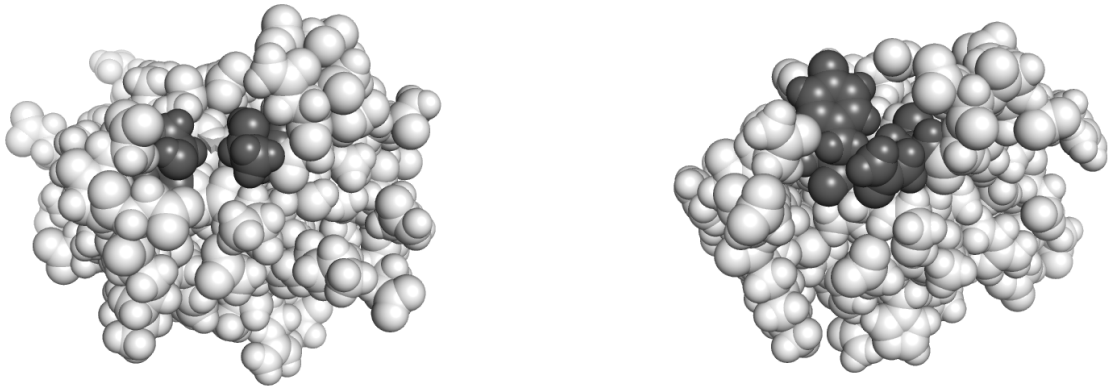

B

Figure 32. (**A**) Sequence alignment of the N-terminal and C-terminal domains of CaM. The residues Thr26, Thr62, Tyr99 and Gln135 are highlighted in bold. (**B**) Atomic models of the N-terminal (**left**) and C-terminal (**right**) domains of apo-CaM. The side-chains of residues Thr26 and Thr62 in the N-terminal domain as well as the corresponding residues Tyr99 and Gln135 in the C-terminal domain are highlighted in dark gray.

3.4.3. Interaction of FKBP38$^{35\text{-}153}$ with holo-calmodulin

As mentioned already in section 2.2.4.2.3., the titration of ^{15}N-labelled FKBP38$^{35\text{-}153}$ with holo-CaM produced no results due to the denaturation of FKBP38$^{35\text{-}153}$ during the experiment. However, ^{15}N-labelled holo-CaM was successfully complexed with FKBP38$^{35\text{-}153}$. The chemical shift changes obtained were even larger than those found in the corresponding experiment with apo-CaM (Figure 33), as an average value of 0.031 ppm was obtained for the combined chemical shift perturbations $\Delta\delta$, with a maximal value of 0.185 ppm for Glu68 (Figure 34). Moreover, several signals of the N-terminal holo-CaM domain (e.g. Phe19 and Thr70) (Figures 33 and 34) disappeared upon complex formation due to extensive line-broadening. This change on the backbone relaxation could originate from (i) the presence of an additional relaxation process in the complexed state of holo-CaM or (ii) a change in the time scale of a conformational interconversion that may lead to an increase of the relaxation rates for these resonances.

All residues undergoing either significant chemical shift perturbations (i.e. those larger than 0.04 ppm) or changes of their backbone relaxation upon complex formation are located in the N-terminal holo-CaM domain. Again, pronounced effects were found in the central loops of both

EF-hand motifs of this domain, which are therefore considered as the region of the protein directly in contact with FKBP38$^{35\text{-}153}$ (Figure 35).

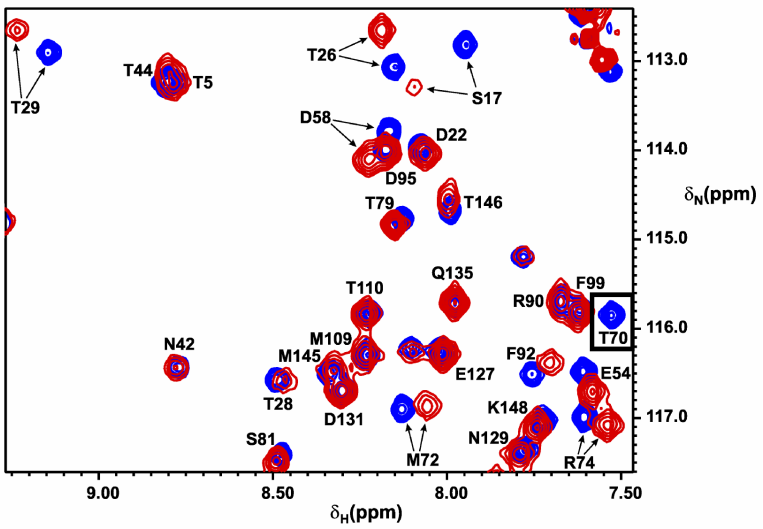

Figure 33. Section from the $^{1}H/^{15}N$-HSQC spectrum of ^{15}N-labelled holo-CaM, showing the changes produced in the backbone resonances by the complex formation with FKBP38$^{35\text{-}153}$. The red signals correspond to the free form of holo-CaM, while the blue signals correspond to the FKBP38$^{35\text{-}153}$/holo-CaM complex. The resonance belonging to Thr70, shown in a black box, is visible only in the spectrum of the free form.

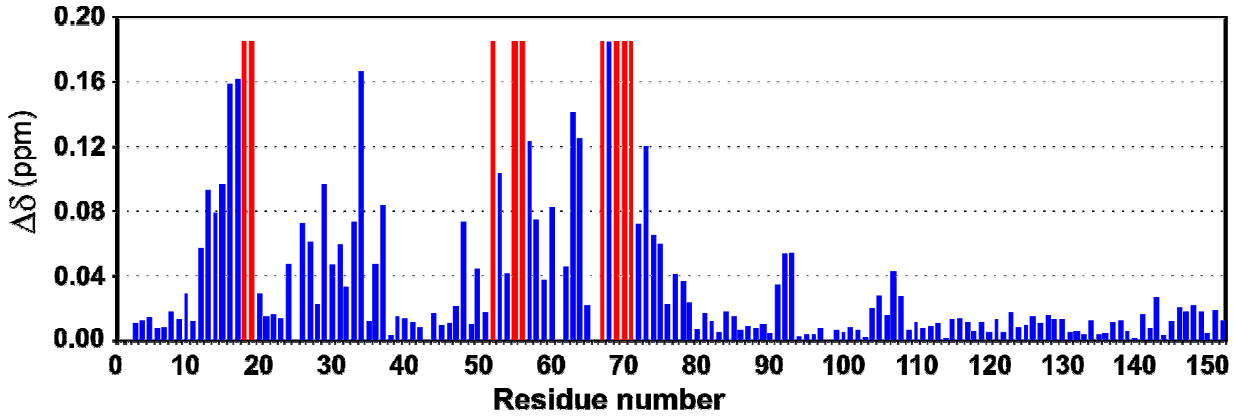

Figure 34. Overview of the combined chemical shift changes (Δδ) observed for ^{15}N-labelled holo-CaM upon addition of a 3-fold molar excess of FKBP38$^{35\text{-}153}$. Residues showing changes in the backbone dynamics (i.e. signals with extensive line-broadening) upon complex formation were assigned the maximal chemical shift perturbation value (represented by red bars).

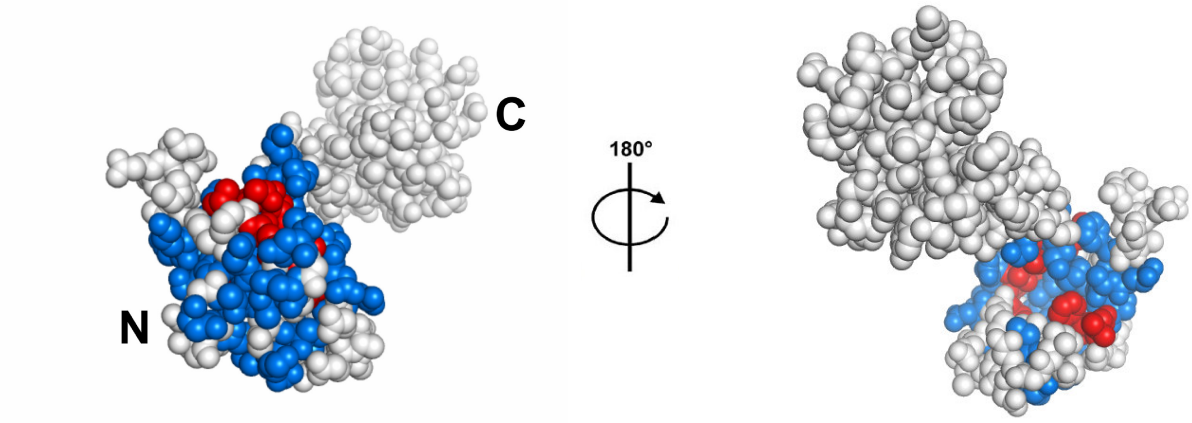

Figure 35. Atomic model of holo-CaM that shows the surface which interacts with FKBP38$^{35\text{-}153}$. Residues displaying chemical shift perturbations higher than 0.04 ppm due to the presence of FKBP38$^{35\text{-}153}$ are colored in blue. Residues undergoing a change in backbone dynamics upon complex formation are highlighted in red.

Nevertheless, additional perturbation effects of considerable magnitude were also found in all four helices of the N-terminal domain, always at the ends that are closer to the central loops. These residues, however, are either not surface accessible (e.g. Phe16, Gly33, Ile52, Asp56 and Phe68) or can not easily contribute to the formation of a more reasonable interacting surface as that featured by the central loops of the EF-hand motifs. Therefore, these effects at the helices are considered as secondary effects, which propagate through the helices as the result of the FKBP38$^{35\text{-}153}$ interaction with the surface defined by both central loops.

As in the case of apo-CaM, the replacement of the residues Thr26 and Thr62, which are located at the center of the contact region of the N-terminal holo-CaM domain, with Tyr99 and Gln135 in the C-terminal domain seems to be the reason for the higher affinity of FKBP38$^{35\text{-}153}$ for the N-terminal holo-CaM domain. Both side-chains, especially that of Tyr99, protrude from the surface of the C-terminal holo-CaM domain (Figure 36), producing an uneven surface instead of a flat or slightly caved surface in the N-terminal domain.

Figure 36. Atomic models of the N-terminal (**left**) and C-terminal (**right**) domains of holo-CaM. The side-chains of residues Thr26 and Thr62 in the N-terminal domain as well as the corresponding residues Tyr99 and Gln135 in the C-terminal domain are highlighted in dark gray.

3.4.4. Comparison of the interactions of FKBP38$^{35\text{-}153}$ with apo- and holo-calmodulin

The chemical shift perturbations calculated from the titrations of ^{15}N-labelled apo- and holo-CaM with FKBP38$^{35\text{-}153}$ are presented in Figure 37. Remarkably, in both forms of CaM only residues belonging to the N-terminal domain were affected by the complex formation with FKBP38$^{35\text{-}153}$. Moreover, the affected residues can be grouped into two segments (Lys13-Arg37 and Asn53-Asp64), which are centered at the EF-hand loops of the N-terminal CaM domain. Interestingly, although these protein segments are responsible for the Ca^{2+}-binding in this CaM domain, their conformation does not change considerably between the apo- and the holo-form (Figure 38), as reflected by a backbone RMSD of 2.09 Å between this region (i.e. the segments Lys13-Glu31 and Asp58-Asp64) of the apo- and holo-CaM structures. On the other hand, the

amide resonances corresponding to the segment Ser38-Met51, the one displaying the most pronounced structural variation upon Ca^{2+}-binding, show no significant shift effects as a result of the complex formation with $FKBP38^{35-153}$ (with the single exception of Leu48 in holo-CaM). The fact that the regions of CaM which are involved in the interaction with $FKBP38^{35-153}$ essentially present the same backbone fold could provide an explanation why the interaction between the N-terminal CaM domain and $FKBP38^{35-153}$ is Ca^{2+}-independent.

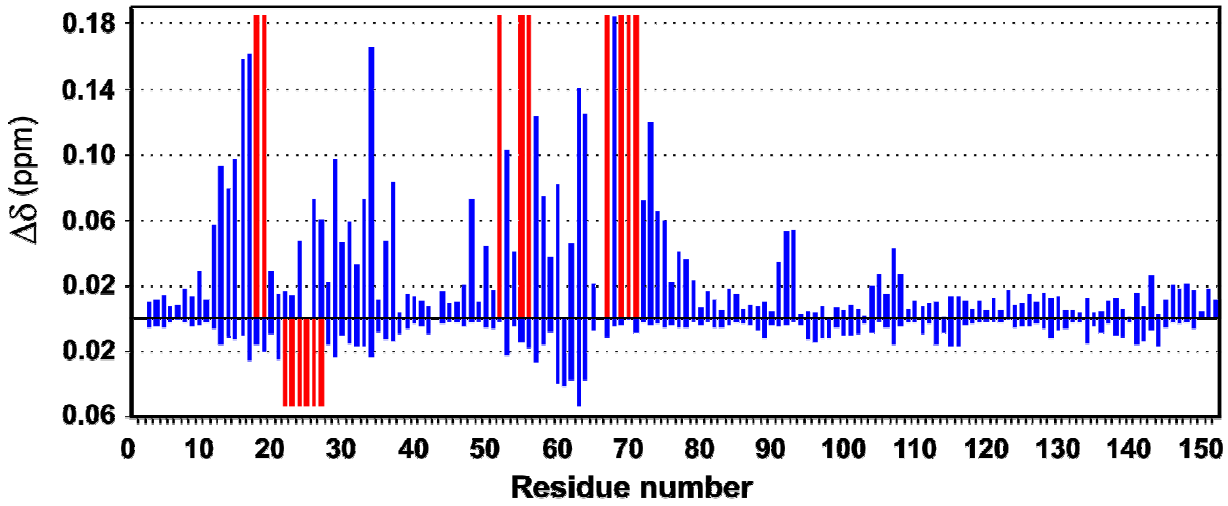

Figure 37. Comparison of the combined chemical shift changes (Δδ) observed for ^{15}N-labelled apo- (**lower part**) and holo-CaM (**upper part**) upon addition of a 3-fold molar excess of $FKBP38^{35-153}$. Residues undergoing changes in the backbone dynamics upon complex formation were assigned the maximal chemical shift perturbation value (represented by red bars).

Nevertheless, a few differences were observed between the experiments with apo- and holo-CaM. First, the magnitude of the chemical shift changes produced by the complex formation with $FKBP38^{35-153}$ was about 3-fold higher in the case of holo-CaM. Moreover, additional residues (e.g. Ile52 and especially the segment Glu67-Lys75) were affected by the interaction of holo-CaM with $FKBP38^{35-153}$. An explanation for these observations might be a more pronounced conformational disturbance in holo-CaM during the binding event, compared to apo-CaM.

In addition, a different response in the relaxation of certain resonances upon binding to $FKBP38^{35-153}$ was found between apo- and holo-CaM. In the case of apo-CaM, the signals of the resonances corresponding to the segment Asp22-Lys27 were observed only in the complexed form, whereas in holo-CaM several resonances belonging to residues in the helices A, C and D were detected only in the free form. The origin of these effects could be associated with the differences in backbone dynamics between both forms of CaM (i.e. a more flexible backbone in apo-CaM than in holo-CaM) (Kuboniwa et al. 1995, Tjandra et al. 1995, Barbato et al. 1992).

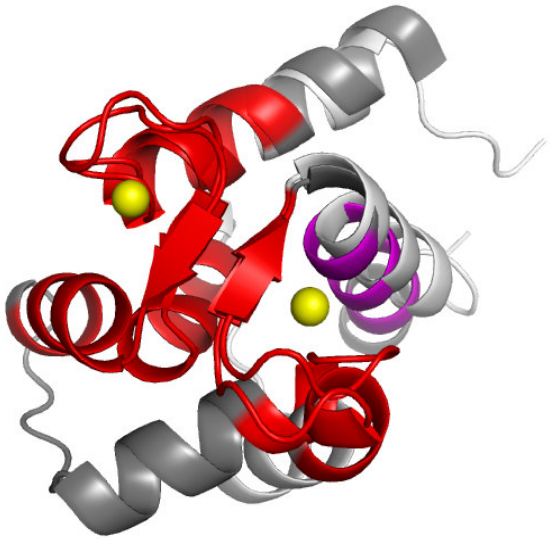

Figure 38. Backbone superposition of apo-CaM (white ribbon) and holo-CaM (gray ribbon). The regions affected by the interaction with FKBP38$^{35-153}$ are highlighted in red. The segment Glu67-Lys75, which is affected only in holo-CaM, is represented in magenta. The Ca^{2+} atoms of holo-CaM are shown as yellow spheres.

3.4.5. Three-dimensional structures of the FKBP38$^{35-153}$/CaM complexes

For the calculation of the three-dimensional structures of the apo- and holo-CaM/FKBP38$^{35-153}$ complexes with HADDOCK, the information obtained from the NMR titration experiments (i.e. residues experiencing chemical shift changes or dynamic effects upon complex formation) was converted into AIRs. The cut-offs for the combined chemical shift changes ($\Delta\delta_{cut-off}$) were selected arbitrarily, but always at values higher than the average chemical shift changes ($\Delta\delta_{ave}$) of each data set. A surface accessibility of at least 20%, calculated for all atoms of the residues with the program NACCESS (Hubbard and Thornton, 1993), was introduced as an additional precondition. The residues complying with both requirements were selected as active AIRs. Furthermore, residues directly adjacent to other that represent active AIRs were selected as passive AIRs, if they are surface accessible as well. The result of this selection process was a well-defined interaction surface, composed of active and passive AIR residues, which could be used for the docking calculation with HADDOCK. The transformation of a set of chemical shift perturbations into an interaction surface for HADDOCK calculations is exemplified for FKBP38$^{35-153}$ in Figure 39.

3.4.5.1. Three-dimensional structure of the FKBP38$^{35-153}$/apo-CaM complex

In the case of FKBP38$^{35-153}$, a $\Delta\delta_{cut-off}$ of 0.005 ppm was chosen, which is slightly higher than the $\Delta\delta_{ave}$ of 0.004 ppm. The residues Glu35, Trp36, Leu37, Lys48, Leu51, Ser58, His69, Gln71, Leu74, Glu75, Asn76, Gly77, Arg79, Val80, Gln81, Asp94, Val95, Ile96, Asp107, Thr111,

Tyr122, Ser128, Tyr130 and Ile131 all showed Δδ values above this cut-off. Residues Glu75, Asn76, Gly77 and Arg79, all surface accessible and defining the central region of the interaction surface, were selected as active AIRs. On the other hand, residues Val80, Val95, Ile96, Tyr122 and Ile131, which are not surface accessible, as well as Leu37, Leu51, Ser58, His69, Gln81, Asp94, Asp107 and Thr111, which are located either at the opposite side of the protein or too peripheral relative to the rest in the molecular surface, were rejected as AIRs. The rest of these residues were selected as passive AIRs for the following reasons: (i) Glu35, Trp36, Lys48, Gln71, Ser128 because of their location at the borders of the interaction surface; (ii) Leu74, as a consequence of its rather low surface accessibility and (iii) Tyr130, since its use as active AIR led to a presumably incorrect structural arrangement, were the side-chains of Tyr130 and Lys30 (from CaM) point towards each other in order to fulfill the imposed constraint. Residues Thr78, Pro129, Pro132 and Ala136, which are also part of the interaction surface, were introduced as additional passive AIRs according to the criteria described above (Figure 39, Table 7).

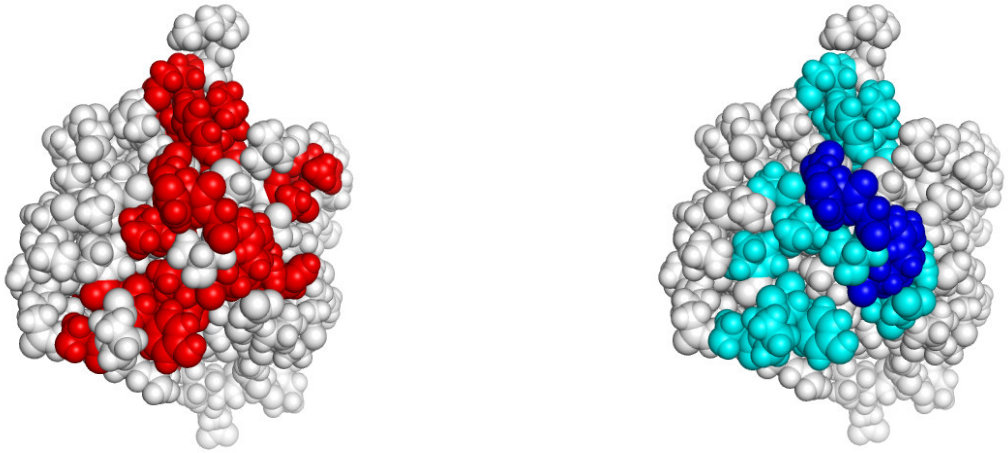

Figure 39. Atomic models of FKBP38$^{35\text{-}153}$ that show (**A**) the residues affected by the interaction with apo-CaM, and (**B**) the residues selected as active (blue) and passive (cyan) AIRs for the docking calculation of the complex structure.

In the case of apo-CaM, where $\Delta\delta_{ave}$ was 0.009 ppm, a $\Delta\delta_{cut\text{-}off}$ of 0.02 ppm is a reasonable criterion for the discrimination of interacting residues. This cut-off value was surpassed by residues Ser17, Lys21, Thr29, Thr34, Asn53, Ala57, Asn60, Gly61, Thr62, Ile63 and Asp64. In addition, the residues experiencing dramatic changes in their dynamics, i.e. Asp22, Gly23, Asp24, Gly25, Thr26 and Ile27, were also considered for selection as possible AIRs. As a consequence, the residues Asp22, Gly23, Asp24, Thr26, Thr29, Asn60, Gly61 and Thr62 were selected as active AIRs. Residues Ile27 and Ile63, on the other hand, were neglected as AIRs due to their low surface accessibility. The residues Ser17, Thr34, Asn53 and Ala57 were rejected as direct contact partners because of their peripheral location relative to the rest. For the same

reason, Lys21, Gly25 and Asp64 were selected only as passive AIRs. In addition, surface-accessible spatial neighbors of the active AIR residues (i.e. residues Thr28, Lys30, Glu31, Asp58 and Gly59) were introduced as passive AIRs (Table 7).

Table 7. Description of the FKBP38$^{35-153}$ and apo-CaM residues that were used as active and passive AIRs in the docking calculations. Δδ: combined chemical shift changes in ppm. SA: surface accessibility. L.N.: Line narrowing observed in apo-CaM upon complex formation with FKBP38$^{35-153}$. In the case of FKBP38$^{35-153}$, the surface accessibilities are reported as average values ± RMSD from all 20 conformers of the NMR structure ensemble.

FKBP38$^{35-153}$					apo-CaM				
active residues			passive residues		active residues			passive residues	
AA	Δδ	SA (%)	AA	SA (%)	AA	Δδ	SA (%)	AA	SA (%)
E75	0.008	62 ± 12	E35	71 ± 14	D22	L.N.	73	K21	87
N76	0.005	94 ± 13	W36	38 ± 8	G23	L.N.	90	G25	46
G77	0.005	73 ± 10	K48	33 ± 9	D24	L.N.	73	T28	35
R79	0.005	61 ± 7	Q71	22 ± 10	T26	L.N.	24	K30	93
			L74	23 ± 12	T29	0.023	20	E31	26
			T78	60 ± 11	N60	0.039	71	D58	79
			E82	43 ± 12	G61	0.041	26	G59	76
			S128	71 ± 13	T62	0.038	50	D64	25
			P129	74 ± 13					
			Y130	63 ± 11					
			P132	32 ± 13					
			A136	33 ± 13					

The 20 best structures of the FKBP38$^{35-153}$/apo-CaM complex calculated with HADDOCK (Figure 40A) display a quite good structural convergence. However, a main cluster comprising 12 structures, including the energetically most favored structures as well as those with the higher buried surface area could be identified. The averages of the total intermolecular energy (E_{tot}) and buried surface area (BSA) for this cluster are -219.8 ± 59.7 kcal/mol and 1046 ± 131 Å^2, respectively, compared to values of -196.2 ± 65.6 kcal/mol and 998 ± 151 Å^2 for all 20 structures. After elimination of three more conformers from this cluster, i.e. those displaying higher intermolecular energies and lower buried surface areas, a cluster of 9 structures with even better quality remains (Figure 40B), as revealed by averages of -241.2 ± 50.5 kcal/mol for E_{tot} and 1095 ± 112 Å^2 for BSA. The structural statistics for this cluster, which can be considered as the final structure of the FKBP38$^{35-153}$/apo-CaM complex, are shown in Table 8. Moreover, the potential energy associated with the AIRs makes an insignificant contribution to the total intermolecular energy in all selected structures, an indication that these are in good agreement with the experimental data.

The FKBP38$^{35-153}$/apo-CaM complex seems to be favored by good surface complementarities between the proteins. Thus, the βC-βD loop of FKBP38$^{35-153}$ (in particular the residues Asn76

and Gly77) is inserted into a cavity located between the central loops (AB and CD) of both EF-hand motifs in the N-terminal apo-CaM domain (Figure 41A). As a consequence, several hydrophobic contacts as well as hydrogen bonds are present between residues belonging to the βC-βD loop of FKBP38$^{35\text{-}153}$ and residues in the CaM segments Asp22-Thr28 and Gly61-Thr62. In a similar manner, part of the AB loop belonging to apo-CaM, especially the segment Asp22-Asp24, is surrounded by the βC-βD loop and the outer part of the β-sheet of FKBP38$^{35\text{-}153}$ (Figure 41B). Additional stabilization of the complex is provided by salt-bridge formation from Lys21 and Glu31 (both CaM) to Glu140 and Arg79 (both FKBP38$^{35\text{-}153}$), respectively (Figure 41C); either one or both of these salt-bridges are present in most of the conformers.

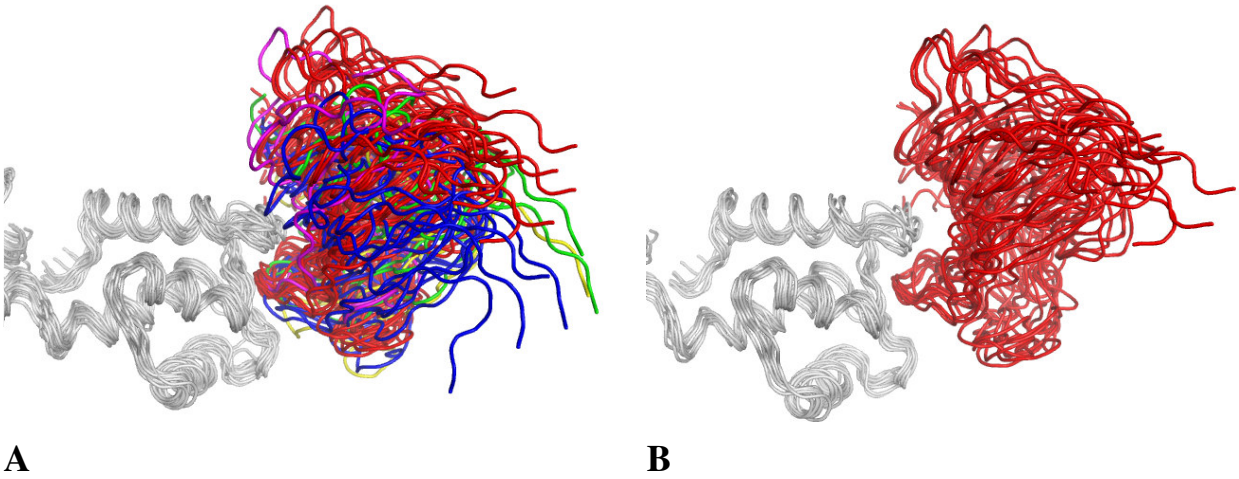

A **B**

Figure 40. Ribbon representation of the backbone of the FKBP38$^{35\text{-}153}$/apo-CaM complex (**A**) All 20 structures of the FKBP38$^{35\text{-}153}$/apo-CaM complex are shown. The N-terminal apo-CaM domains (gray) are superposed, while the FKBP38$^{35\text{-}153}$ molecules are presented in different colors, depending on their structural similarities. The main cluster is colored in red. (**B**) The 9 conformers considered as the final structure of the FKBP38$^{35\text{-}153}$/apo-CaM complex are represented in the same manner as in (A).

Table 8. Statistics of the final 9 conformers of the FKBP38$^{35\text{-}153}$/apo-CaM complex, sorted according to their total intermolecular energy. The backbone RMSDs were calculated for the segment FKBP38$^{36\text{-}150}$ after superposition of CaM$^{5\text{-}75}$.

no.	Backbone RMSDs (Å)									Intermolecular energies (kcal/mol)				BSA (Å^2)
	1	2	3	4	17	12	7	6	14	total	vdw	elec	AIRs	
1	-									-321.9	-39.1	-282.8	0	1249
2	5.27	-								-320.6	-37.5	-283.1	0.01	1308
3	4.50	7.09	-							-270.8	-41.6	-229.2	0.03	1062
4	5.35	4.16	5.66	-						-228.6	-43.0	-185.7	0.03	1099
17	3.22	5.58	6.39	6.09	-					-215.2	-22.7	-192.5	0.02	1000
12	3.05	4.87	5.71	4.83	4.33	-				-211.4	-29.1	-182.4	0.02	977
7	3.84	5.72	6.20	4.44	4.74	3.06	-			-208.1	-33.8	-174.3	0.03	1076
6	5.76	5.58	3.88	4.79	6.74	5.98	7.05	-		-198.6	-37.4	-161.1	0	1043
14	5.59	4.69	4.64	4.30	6.27	5.89	6.89	1.75	-	-196.0	-28.5	-167.5	0.02	1037
Ave.	RMSD = 5.11 ± 1.22									E_{total} = -241.2 ± 50.5 E_{vdw} = -34.7 ± 6.8 E_{elec} = -206.5 ± 47.5 E_{AIRs} = 0.02 ± 0.01 BSA= 1095 ± 112				

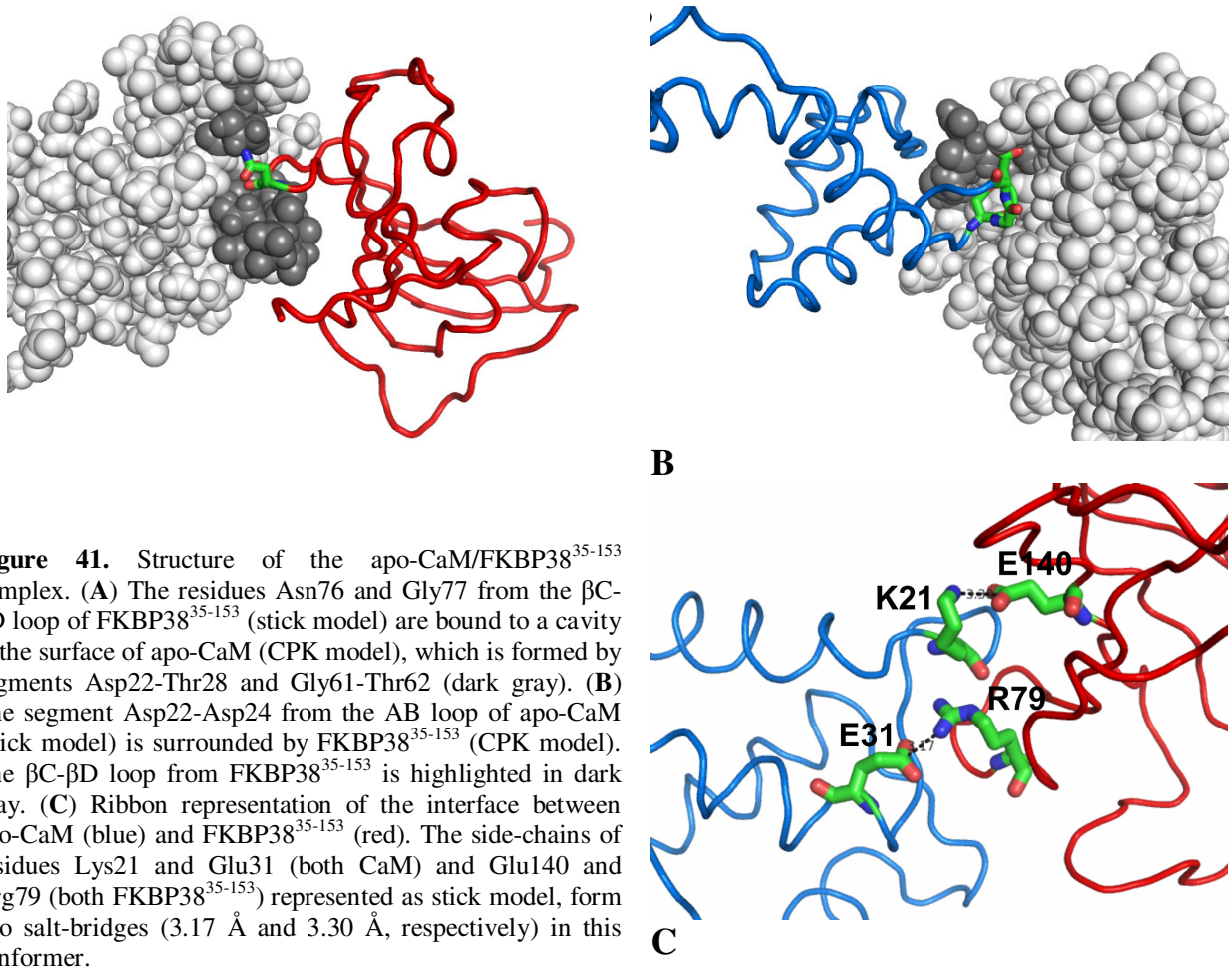

Figure 41. Structure of the apo-CaM/FKBP38$^{35\text{-}153}$ complex. (**A**) The residues Asn76 and Gly77 from the βC-βD loop of FKBP38$^{35\text{-}153}$ (stick model) are bound to a cavity at the surface of apo-CaM (CPK model), which is formed by segments Asp22-Thr28 and Gly61-Thr62 (dark gray). (**B**) The segment Asp22-Asp24 from the AB loop of apo-CaM (stick model) is surrounded by FKBP38$^{35\text{-}153}$ (CPK model). The βC-βD loop from FKBP38$^{35\text{-}153}$ is highlighted in dark gray. (**C**) Ribbon representation of the interface between apo-CaM (blue) and FKBP38$^{35\text{-}153}$ (red). The side-chains of residues Lys21 and Glu31 (both CaM) and Glu140 and Arg79 (both FKBP38$^{35\text{-}153}$) represented as stick model, form two salt-bridges (3.17 Å and 3.30 Å, respectively) in this conformer.

3.4.5.2. Three-dimensional structure of the FKBP38$^{35\text{-}153}$/holo-CaM complex

For the calculation of the FKBP38$^{35\text{-}153}$/holo-CaM complex, no experimental data regarding the interaction surface in FKBP38$^{35\text{-}153}$ could be obtained due to denaturation of FKBP38$^{35\text{-}153}$ in the experiment (see section 2.2.4.2.3.). Nevertheless, as the activation of FKBP38$^{35\text{-}153}$ by CaM has been reported to occur in a Ca^{2+}-independent manner (Edlich et al., in preparation), it could be assumed that the same FKBP38$^{35\text{-}153}$ region interacts with apo- and holo-CaM. Therefore, the same FKBP38$^{35\text{-}153}$ residues as in section 3.4.5.1. were selected for the HADDOCK calculation of the FKBP38$^{35\text{-}153}$/holo-CaM complex (Table 9).

In the case of holo-CaM, were $\Delta\delta_{ave}$ was equal to 0.031 ppm, the $\Delta\delta_{cut\text{-}off}$ was set to 0.04 ppm. The residues showing either CSP above this cut-off or dynamic effects include the segments Phe12-Phe19, Asp24, Thr26-Ile27, Thr29-Glu31, Gly33-Thr34, Met36-Arg37, Leu48, Asp50, Ile52-Asp58, Asn60, Thr62-Asp64 and Glu67-Lys75. Residues located in the four helices of the N-terminal CaM domain were excluded as their CSPs probably represent secondary effects of the interaction. Moreover, residue Asp58 was chosen only as passive AIR due to its peripheral

location at the interaction surface. Hence, the residues Asp24, Thr26, Lys30, Asn60, Thr62 and Asp64 were selected as active AIRs, while their surface-accessible spatial neighbors, i.e. Asp22, Gly23, Gly25, Thr28, Gly59, Gly61, Phe65 and Pro66 were selected as passive AIRs in addition to Asp58 (Table 9).

Table 9. Description of the FKBP38$^{35-153}$ and holo-CaM residues that were used as active and passive AIRs in the docking calculations. Δδ: combined chemical shift changes in ppm. SA: surface accessibility. In the case of FKBP38$^{35-153}$, the surface accessibilities are reported as average values ± RMSD from all 20 conformers of the NMR structure ensemble.

FKBP38$^{35-153}$					holo-CaM				
active residues			passives residues		active residues			passives residues	
AA	Δδ	SA (%)	AA	SA (%)	AA	Δδ	SA (%)	AA	SA (%)
E75	0.008	62 ± 12	E35	71 ± 14	D24	0.047	60	D22	76
N76	0.005	94 ± 13	W36	38 ± 8	T26	0.072	26	G23	72
G77	0.005	73 ± 10	K48	33 ± 9	K30	0.047	65	G25	42
R79	0.005	61 ± 7	Q71	22 ± 10	N60	0.082	73	T28	20
			L74	23 ± 12	T62	0.046	22	D58	68
			T78	60 ± 11	D64	0.125	29	G59	75
			E82	43 ± 12				G61	43
			S128	71 ± 13				F65	22
			P129	74 ± 13				P66	60
			Y130	63 ± 11					
			P132	32 ± 13					
			A136	33 ± 13					

Most of the 20 best structures of the FKBP38$^{35-153}$/holo-CaM complex (Figure 42) calculated with HADDOCK can be grouped into two structural clusters, which consist of 9 (cluster I, Table 10) and 8 structures (cluster II, Table 11), respectively, and differ only by a rather small shift of the FKBP38$^{35-153}$ molecule over the holo-CaM surface. The remaining three structures display a completely different orientation that can be discarded, however, as it does not explain observed contacts between the unstructured FKBP38 N-terminus (FKBP38$^{1-34}$) and the CaM helix A (Katja Heydenreich, unpublished results). Although the structures belonging to cluster I exhibit a slightly better convergence, as revealed by the average backbone RMSD of 5.42 ± 2.03 Å compared to 5.84 ± 1.48 Å in cluster II, the latter can be considered the better solution for this complex structure, as it exhibits a slightly lower average intermolecular energy of -187.3 ± 43.1 kcal/mol (compared to -174.1 ± 39.5 kcal/mol in cluster I) and a considerably higher average BSA of 1182 ± 103 Å^2 (compared to 1042 ± 75 Å^2 in cluster I).

In the FKBP38$^{35-153}$/holo-CaM complex structure, the loops AB (i.e. segment Asp22-Lys30) and CD (i.e. segment Asp58-Pro66) of holo-CaM are interacting with the βC-βD loop (i.e. segment Glu75-Arg79) and part of the β-sheet (external side) of FKBP38$^{35-153}$, including for example, residues Trp36, Lys48, Leu50 (Figure 43). This complex is stabilized by several electrostatic

interactions, such as (i) a salt-bridge between Asp64 from holo-CaM and Lys48 from FKBP38 (present in 4 out of 8 structures) and (ii) some hydrogen bonds as for example between the side-chains of Asn60 (holo-CaM) and Glu75 (FKBP38$^{35\text{-}153}$) (present in 7 structures) and between Thr62 $H^{\gamma 1}$ (holo-CaM) and the Glu75 backbone carbonyl oxygen (FKBP38$^{35\text{-}153}$) (present in 5 structures) Most of these interactions are present in the lowest energy structure (Figure 44).

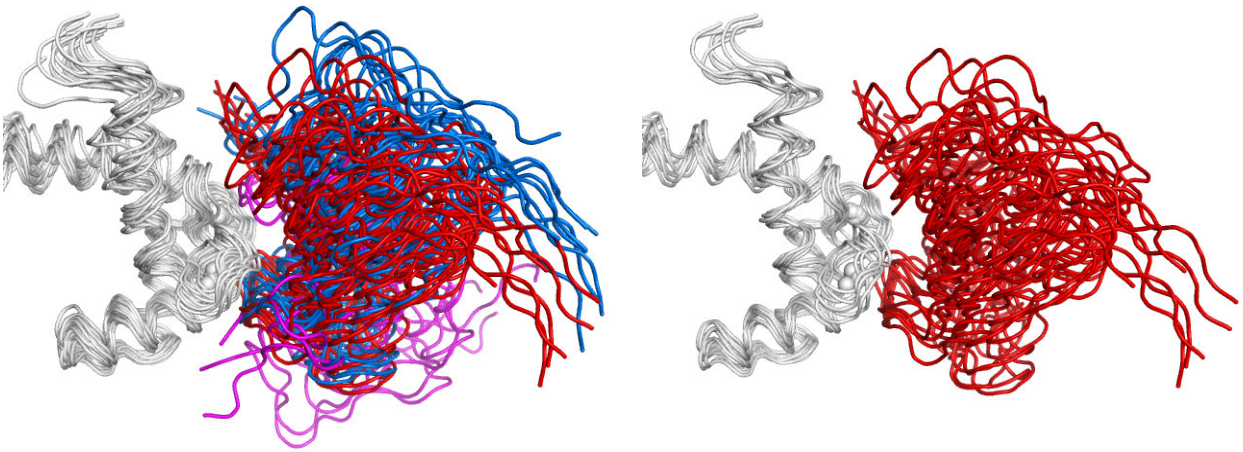

Figure 42. Ribbon representation of the backbone of the FKBP38$^{35\text{-}153}$/holo-CaM complex. (**A**) All 20 structures of the FKBP38$^{35\text{-}153}$/holo-CaM complex are shown. The N-terminal holo-CaM domains (gray) are superposed, while the FKBP38$^{35\text{-}153}$ molecules belonging to the clusters I and II as well as the three structures displaying a different orientation are shown in blue, red and magenta, respectively. (**B**) The structures from cluster II, considered as the best solution for the FKBP38$^{35\text{-}153}$/holo-CaM complex, are represented in the same manner as in (A).

Table 10. Statistics of the 9 conformers belonging to cluster I of the FKBP38$^{35\text{-}153}$/holo-CaM complex, sorted according to their total intermolecular energies. The backbone RMSDs were calculated for the segment FKBP38$^{36\text{-}150}$ after superposition of CaM$^{5\text{-}75}$.

	Backbone RMSDs (Å)									Intermolecular energies (kcal/mol)				BSA (Å^2)
	2	7	1	6	14	15	19	20	13	total	vdw	elec	AIRs	
2	-									-240.0	-36.4	-203.6	0	1037
7	5.39	-								-220.8	-33.2	-187.6	0.03	1084
1	6.44	2.86	-							-194.8	-44.1	-150.7	0	1139
6	7.72	3.97	3.79	-						-191.0	-37.4	-153.7	0.01	1059
14	9.58	5.92	6.86	4.57	-					-157.5	-33.9	-123.6	0	1100
15	5.25	4.32	5.69	7.03	9.19	-				-151.4	-34.6	-116.8	0	1034
19	6.32	2.71	2.45	5.22	7.67	5.00	-			-146.2	-29.7	-116.4	0.02	911
20	5.67	2.05	3.34	4.12	6.49	4.79	2.81	-		-143.1	-23.5	-119.5	0.04	933
13	9.13	5.32	6.28	3.68	2.08	8.18	7.14	5.90	-	-122.2	-37.8	-84.4	0.02	1078
Ave.	RMSD = 5.42 ± 2.03									E_{total} = -174.1 ± 39.5 E_{vdw} = -34.5 ± 5.7 E_{elec} = -139.6 ± 37.9 E_{AIRs} = 0.01 ± 0.02 BSA = 1042 ± 75				

Table 11. Statistics of the 8 conformers belonging to cluster II of the FKBP38$^{35-153}$/holo-CaM complex, sorted according to their total intermolecular energies. The backbone RMSDs were calculated for the segment FKBP38$^{36-150}$ after superposition of CaM$^{5-75}$.

	Backbone RMSDs (Å)								Intermolecular energies (kcal/mol)				BSA
	11	12	3	5	8	18	17	10	total	vdw	elec	AIRs	(Å^2)
11	-								-248.5	-25.7	-222.8	0	1299
12	7.83	-							-234.8	-26.6	-208.1	0.05	1047
3	4.67	6.26	-						-217.0	-37.9	-179.1	0	1300
5	6.77	4.07	5.24	-					-190.9	-39.7	-151.3	0	1245
8	7.07	4.91	7.73	6.17	-				-176.8	-36.4	-140.3	0.04	1173
18	7.40	4.45	7.66	4.56	3.26	-			-154.4	-31.6	-122.8	0.01	1192
17	7.31	3.04	6.23	5.32	3.99	5.11	-		-143.4	-34.1	-109.4	0.01	1025
10	7.80	4.23	5.40	6.20	7.74	7.53	5.64	-	-132.6	-38.2	-94.4	0	1176
Ave.	RMSD = 5.84 ± 1.48								E_{total} = -187.3 ± 43.1 E_{vdw} = -33.8 ± 5.3 E_{elec} = -153.5 ± 46.3 E_{AIRs} = 0.01 ± 0.02 BSA= 1182 ± 103				

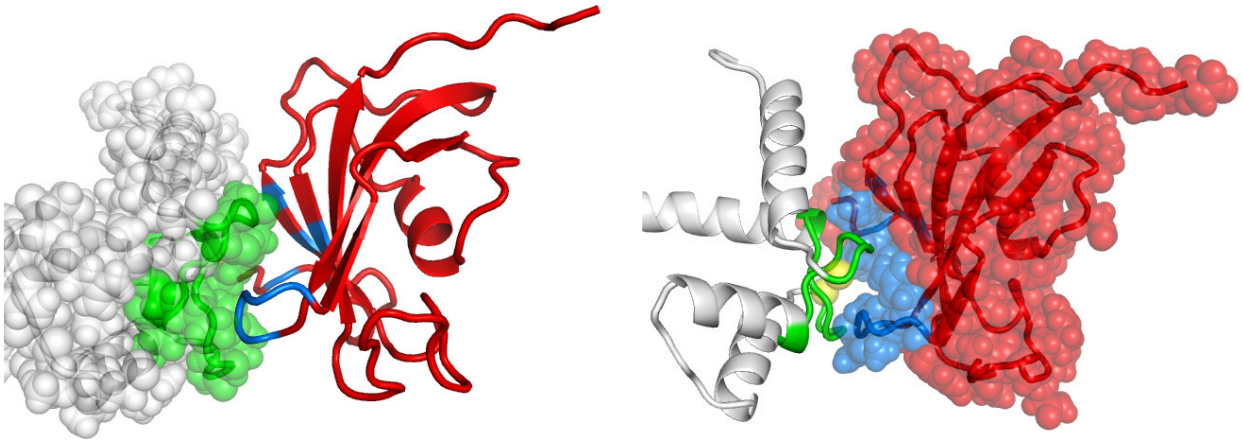

A **B**

Figure 43. Structure of the FKBP38$^{35-153}$/holo-CaM complex. (**A**) The holo-CaM molecule is shown as CPK model and the FKBP38$^{35-153}$ backbone as ribbon. (**B**) The backbone of holo-CaM is represented as ribbon and FKBP38$^{35-153}$ as CPK model. The segments Lys21-Lys30 and Asp58-Pro66 of holo-CaM as well as segment Glu75-Arg79 and residues Trp36, Lys48 and Leu50 belonging to FKBP38$^{35-153}$, which mediate the interaction in the complex, are highlighted in green and blue, respectively. Calcium ions are shown as yellow spheres.

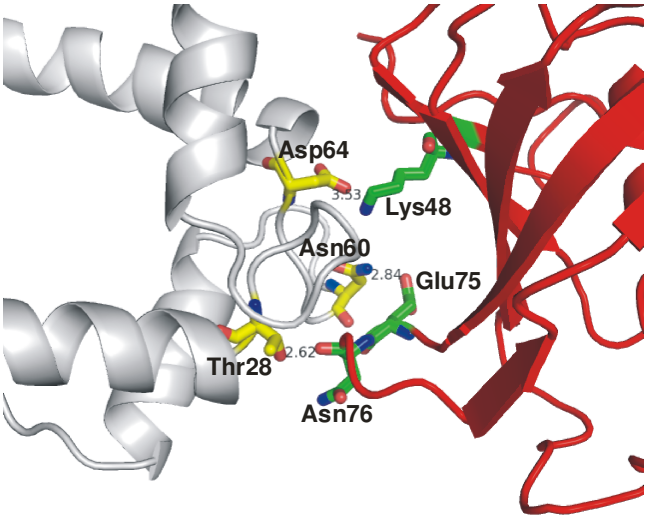

Figure 44. Electrostatic and polar interactions stabilizing the structure of the FKBP38$^{35-153}$/holo-CaM complex. The interface between holo-CaM (gray ribbon) and FKBP38$^{35-153}$ (red ribbon) in the lowest energy conformer of cluster II is displayed. Residues Thr28, Asn60 and Asp64 (all holo-CaM), as well as Asn76, Glu75 and Lys48 (all FKBP38$^{35-153}$), involved in intermolecular hydrogen-bond and salt-bridge formation, are shown as sticks colored by atom type.

3.4.5.3. Comparison of the three-dimensional structures of the FKBP38$^{35\text{-}153}$/CaM complexes

The lowest energy structures of the FKBP38$^{35\text{-}153}$ complexes with apo- and holo-CaM are compared in Figure 45. Both complex structures diverge, as indicated by (i) a difference of ~120º in the orientation of the apo- and holo-CaM molecules relative to FKBP38$^{35\text{-}153}$ and (ii) a considerable displacement of the CaM molecule over the FKBP38$^{35\text{-}153}$ surface (Figure 45A and B). Thus, apo-CaM interacts with a surface centered at the βC-βD loop of FKBP38$^{35\text{-}153}$, also contacting the external side of the β-sheet and the βE-βF loop, whereas the contact with holo-CaM is centered at the external side of the β-sheet of FKBP38$^{35\text{-}153}$.

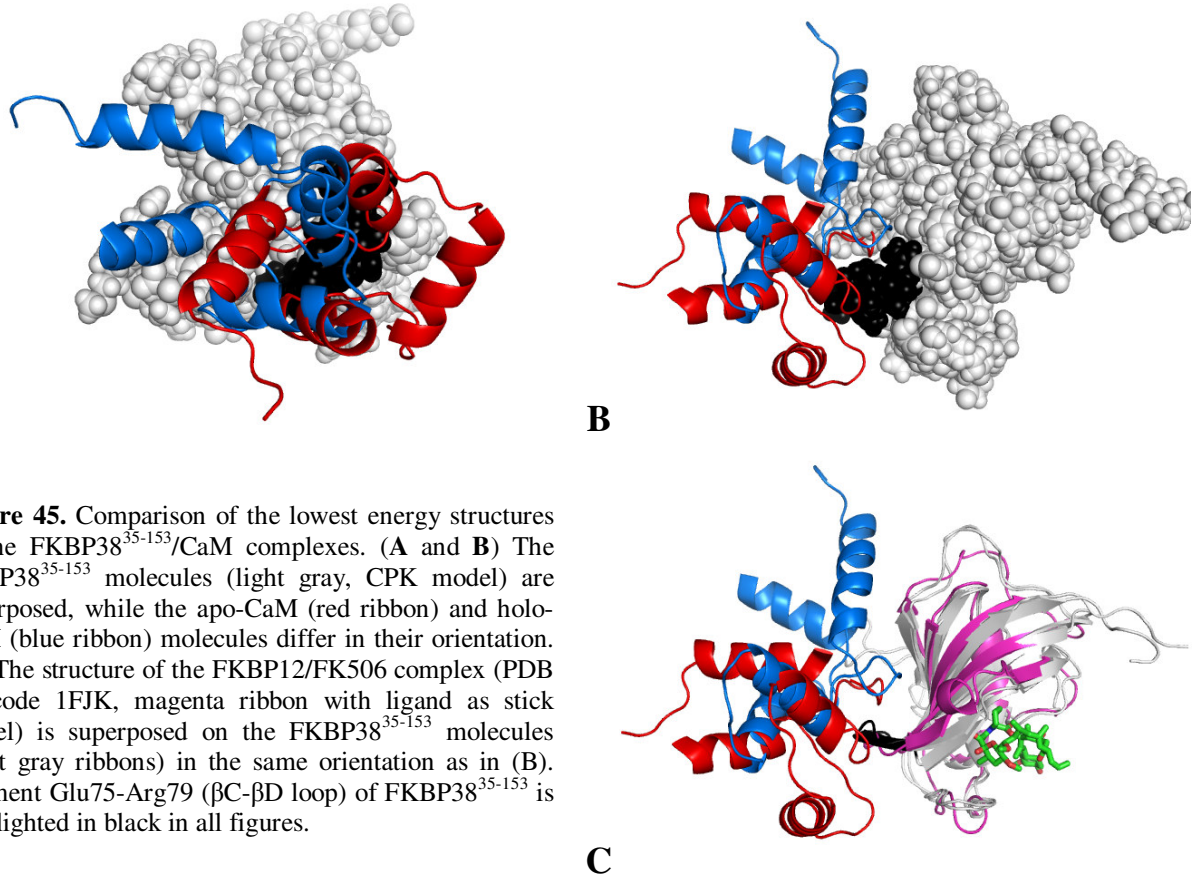

Figure 45. Comparison of the lowest energy structures of the FKBP38$^{35\text{-}153}$/CaM complexes. (**A** and **B**) The FKBP38$^{35\text{-}153}$ molecules (light gray, CPK model) are superposed, while the apo-CaM (red ribbon) and holo-CaM (blue ribbon) molecules differ in their orientation. (**C**) The structure of the FKBP12/FK506 complex (PDB ID code 1FJK, magenta ribbon with ligand as stick model) is superposed on the FKBP38$^{35\text{-}153}$ molecules (light gray ribbons) in the same orientation as in (B). Segment Glu75-Arg79 (βC-βD loop) of FKBP38$^{35\text{-}153}$ is highlighted in black in all figures.

The origin of these structural differences is the diverging contact surfaces of apo- and holo-CaM (Figure 46). In the case of apo-CaM, the surface interacting with FKBP38$^{35\text{-}153}$ features a cavity which accommodates the βC-βD loop of FKBP38$^{35\text{-}153}$. Such a cavity is not present in holo-CaM, which may therefore prefer to bind to the flatter surface presented by the external side of the β-sheet of FKBP38$^{35\text{-}153}$.

Although both complexes display different structural arrangements, they present a fundamental

characteristic in common: the interaction of CaM with the βC-βD loop of FKBP38$^{35\text{-}153}$. This interaction might propagate through the N-terminal end of the βD strand, which in fact includes several resonances (i.e. the segment Val80-Glu82) that display broadened signals in the $^{1}H/^{15}N$-HSQC spectrum of FKBP38$^{35\text{-}153}$ presumably due to increased backbone dynamics or conformational exchange. This could finally lead to a change in the orientation of the Glu83 side-chain, located in βD, which is considered to possibly be responsible for the inactivity of FKBP38$^{35\text{-}153}$, as it is oriented towards the putative binding site where it would collide with the bound substrate (see section 3.2.). Moreover, the interaction of CaM with the βC-βD loop could also produce a conformational rearrangement at the long βE-βF loop, as both loops are in direct contact in the FKBP38$^{35\text{-}153}$ structure. Such a rearrangement could also lead to the activation of FKBP38$^{35\text{-}153}$, as the βE-βF loop is supposedly blocking the access to the active site of FKBP38. This activation of FKBP38$^{35\text{-}153}$ by both apo- and holo-CaM had already been demonstrated in binding assays with Bcl-2 (Edlich et al., in preparation), which corroborates the relevance of both complex structures.

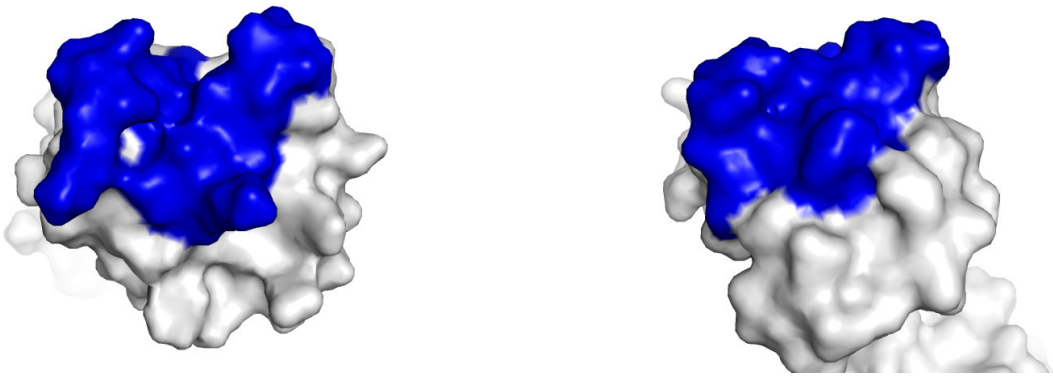

Figure 46. Comparison of the surfaces of apo-CaM (**left**) and holo-CaM (**right**), involved in the complex formation with FKBP38$^{35\text{-}153}$. The residues interacting with FKBP38$^{35\text{-}153}$ are highlighted in blue.

Another common feature of both complexes is the contact between the Trp36 indole ring of FKBP38$^{35\text{-}153}$ and the N-terminal CaM domain. This explains the very similar fluorescence results obtained in titrations of FKBP38$^{35\text{-}153}$ with apo- and holo-CaM (Edlich et al., in preparation).

3.5. Interactions of FKBP38$^{290\text{-}313}$ with holo-calmodulin

As already described in section 1.1.2., FKBP38 contains a putative CaM-binding site located at the C-terminal end of its TPR domain. This binding site was predicted by the Calmodulin Target Database (Yap et al., 2000; http://calcium.uhnres.utoronto.ca/ctdb) for the sequence Leu289-Gly312, with the highest probability in the segment Val293-Arg308. A peptide scan with a

synthetic peptide library of FKBP38 showed a Ca^{2+}-dependent binding to CaM by a peptide comprising residues Ala298-Leu311. This result was subsequently confirmed by binding and competition assays, which were carried out with a synthetic peptide corresponding to $FKBP38^{290-313}$ (Edlich et al., in preparation). In order to structurally characterize this interaction, a CSP study was performed (Figure 47).

The complex formation of ^{15}N-labelled holo-CaM with $FKBP38^{290-313}$ produced an average combined chemical shift change Δδ of 0.017 ppm (Figure 48). The most pronounced effects were found in the C-terminal domain of the protein, with a maximal chemical shift perturbation of 0.100 ppm.

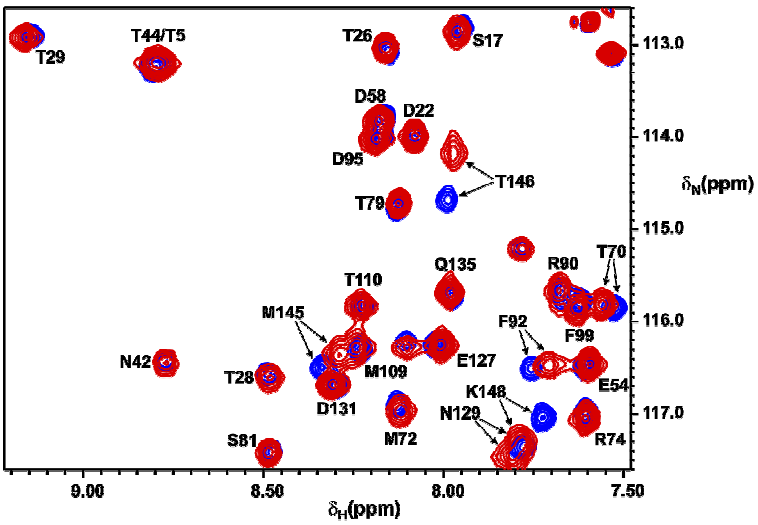

Figure 47. Section from the ^{1}H/^{15}N-HSQC spectrum of ^{15}N-labelled holo-CaM, showing the changes produced in the backbone resonances by the complex formation with $FKBP38^{290-313}$. The blue signals correspond to the free form of holo-CaM, while the red signals correspond to the $FKBP38^{290-313}$/holo-CaM complex.

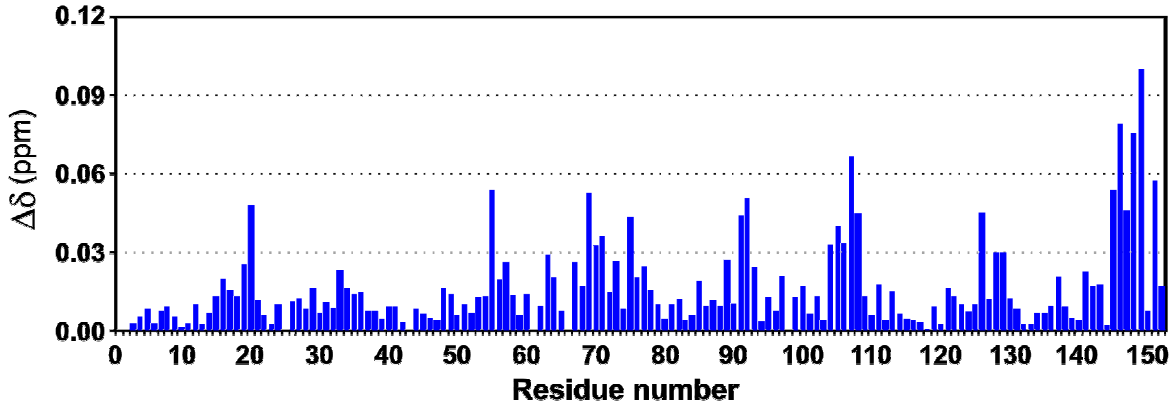

Figure 48. Overview of the combined chemical shift changes (Δδ) observed in ^{15}N-labelled holo-CaM upon addition of a 3-fold molar excess of $FKBP38^{290-313}$.

The CaM residues affected by the interaction with $FKBP38^{290-313}$ are located in different parts of the C-terminal domain (e.g. Val91-Phe92, Glu104-Val108, R126, Ala128-N129 and M145-K148), but most of them are located in or near its methionine-rich cleft (Figure 49), which

suggests that FKBP38$^{290-313}$ binds to this hydrophobic cavity in the C-terminal holo-CaM domain. This interaction could thus resemble that of the CaM complex with the C20W peptide of the plasma membrane Ca^{2+} pump (Elshort et al., 1999), where the C20W peptide binds to the hydrophobic cleft in the C-terminal CaM domain as shown in Figure 49C.

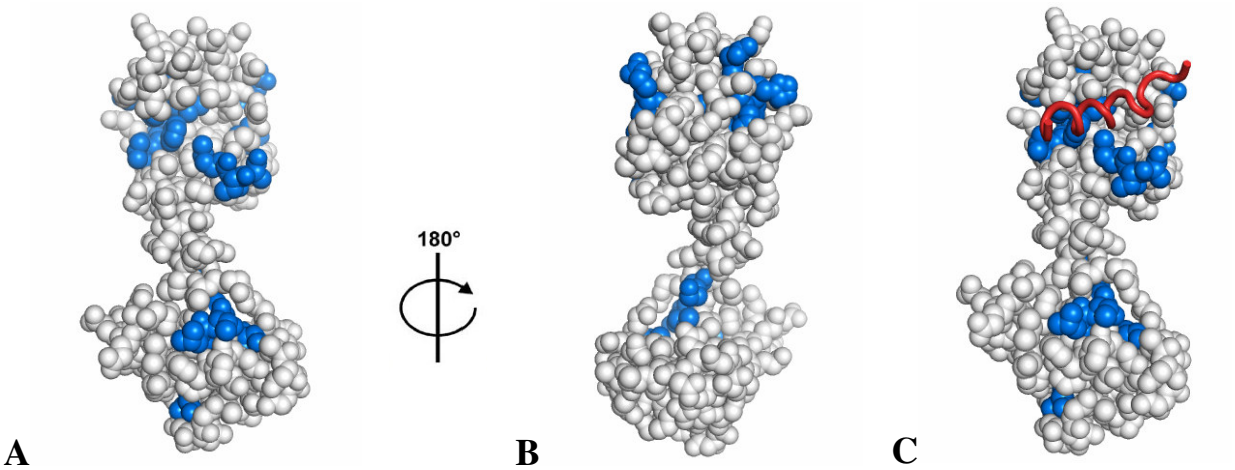

Figure 49. (**A** and **B**) Atomic model of holo-CaM showing the residues affected by the interaction with FKBP38$^{290-313}$. Residues featuring combined chemical shift changes higher than 0.03 ppm upon addition of FKBP38$^{290-313}$ are highlighted in blue. (**C**) The CaM/C20W complex is superposed to holo-CaM (i.e. to its C-terminal domain) and the C20W ligand presented as red ribbon.

At the same time, however, some resonances in the N-terminal holo-CaM domain, i.e. Asp20, Val55, Leu69-Met71 and Lys75, also experienced significant chemical shift changes upon complex formation with FKBP38$^{290-313}$ (Figures 48 and 49). With the exception of Asp20, all these residues are spatially close in the structure of holo-CaM, at a position near the protein surface and not related to the hydrophobic cleft of this domain. An experiment where ^{15}N-labelled holo-CaM was titrated with only 0.8 equivalents of FKBP38$^{290-313}$ showed that these chemical shift changes in the N-terminal CaM domain arose in the same proportion as those observed in the C-terminal domain, which is a clear indication that they are not due to an excess of FKBP38$^{290-313}$. Rather, it suggests a collateral interaction of this part of the N-terminal domain with the FKBP38$^{290-313}$ ligand that is bound to the hydrophobic cleft in the C-terminal CaM domain. Therefore, it can be concluded that FKBP38$^{290-313}$ (i) interacts mainly with the hydrophobic cleft of the C-terminal holo-CaM domain and (ii) produces a secondary interaction with the N-terminal CaM domain.

For the titration with non-labelled holo-CaM, a partially ^{15}N-labelled FKBP38$^{290-313}$ peptide was used. As a first step, the ^{1}H and ^{15}N resonances of this molecule were assigned (Table 12) according to the classical assignment strategy (Wüthrich, 1986).

Table 12. ^{1}H and ^{15}N resonance assignments (in ppm) of FKBP38$^{290-313}$ at 278 K and pH 6.8. The chemical shift values of ^{15}N-labelled amide groups are highlighted in bold.

AA	H^N	*N*	H^a	*Other H*	*Other N*
Ser290	n.a.	-	4.53	3.98, 3.92	
Lys291	n.a.	-	4.39	1.85, 1.46, 1.71, 3.03	
Leu292	**8.50**	**124.6**	4.39	1.64, 1.62, 0.97, 0.91	
Val293	8.40	-	4.11	2.05, 0.97, 0.94	
Lys294	8.60	-	4.31	1.78, 1.75, 1.44, 1.41, 1.75, 3.03	
Lys295	8.55	-	4.28	1.77, 1.44, 1.40, 1.70, 3.02	
His296	8.56	-	4.61	3.14, 8.00, 7.11	
Ala297	**8.51**	**126.4**	4.30	1.40	
Ala298	8.58	-	4.31	1.43	
Gln299	8.52	-	4.34	2.13, 2.04, 2.42, **7.79, 7.10**	**113.3 ε2**
Arg300	8.63	-	4.39	1.91, 1.81, 1.67, 3.22, 7.30	
Ser301	8.66	-	4.53	3.99, 3.92	
Thr302	8.36	-	4.31	1.25	
Glu303	8.49	-	4.37	2.13, 2.02, 2.31	
Thr304	8.27	-	4.30	1.28	
Ala305	**8.50**	**126.2**	4.28	1.41	
Leu306	8.21	-	4.24	1.61, 1.50, 0.94, 0.88	
Tyr307	8.14	-	4.50	3.07, 7.13, 6.83	
Arg308	8.11	-	4.21	1.82, 1.78, 1.65, 1.62, 3.22, 7.30	
Lys309	8.31	-	4.23	1.88, 1.85, 1.51, 1.47, 1.74, 3.04	
Met310	8.45	-	4.47	2.14, 2.07, 2.67, 2.58	
Leu311	**8.29**	**122.9**	4.36	1.72, 1.63, 0.95, 0.90	
Gly312	8.45	-	4.01, 3.95		
Asn313	8.09	-	4.57	2.82, 2.72, 7.60, 6.94	

The results of the titrations of this partially ^{15}N-labelled peptide with (i) holo-CaM and (ii) the C-terminal domain of holo-CaM (holo-CaM$^{76-148}$) are presented in Figure 50. In both titrations, the Leu311 amide signal experienced considerable chemical shift changes of more than 0.10 ppm for the H^N resonance and of ~2 ppm for the N resonance upon complex formation. Moreover, this signal broadened dramatically in the complexed forms. The remaining resonances present in the $^{1}H/^{15}N$-HSQC spectrum were also affected by the complex formation with either holo-CaM or holo-CaM$^{76-148}$, but to a much lower extent. This result suggests that Leu311 is directly involved in the interaction with holo-CaM, while the rest of the labelled residues, i.e. Leu292, Ala297, Ala305 and Gln299, are probably not in close contact with the protein. Furthermore, the fact that very similar effects were observed in both titrations indicates that the C-terminal domain is the one mainly responsible for the interaction with the CaM-binding site of FKBP38.

The observation that FKBP38$^{290-313}$ interacts with the C-terminal domain of holo-CaM is in good agreement with other results (Edlich et al., in preparation), which show that (i) holo-CaM$^{76-148}$

interferes with the activation of FKBP38 by holo-CaM and (ii) FKBP38$^{290-313}$ forms a 1:1 complex with holo-CaM$^{76-148}$ that reveals a binding constant comparable to the FKBP38/holo-CaM complex. This preference of FKBP38$^{290-313}$ for the C-terminal CaM domain is not an isolated case. Another CaM-target peptide structure has been reported where the target peptide binds only to the C-terminal CaM domain (Elshort et al., 1999).

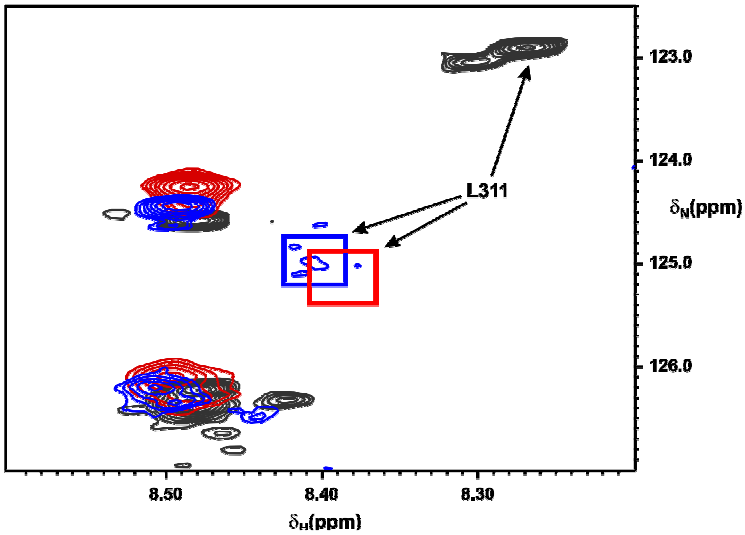

Figure 50. Section from the $^{1}H/^{15}N$-HSQC spectrum of partially ^{15}N-labelled FKBP38$^{290-313}$, showing the changes caused in the backbone resonances by the complex formation with holo-CaM and holo-CaM$^{76-148}$. The black signals correspond to the free form of FKBP38$^{290-313}$, the red signals to the FKBP38$^{290-314}$/holo-CaM complex and the blue signals to the FKBP38$^{290-314}$/holo-CaM$^{76-148}$ complex. The boxes represent the approximate positions of the very broad signal of Leu311 in the complexed forms, which are below the plot level.

3.5.1. Three-dimensional structure of the FKBP38$^{290-313}$/holo-CaM complex

For the docking calculation of the three-dimensional structure of the FKBP38$^{290-313}$/holo-CaM complex, the selection of the AIRs in holo-CaM was carried out in a different manner. This is due to the fact that FKBP38$^{290-313}$ binds to the inner cavity of the C-terminal domain holo-CaM. Therefore, only residues located in this inner cavity were selected as AIRs, instead of surface accessible residues. A cut-off of 0.03 ppm was chosen for the combined chemical shift changes $\Delta\delta$, which is considerably larger than the average value of 0.017 ppm. The residues that exceed this cut-off and either belong to the N-terminal holo-CaM domain, i.e. Asp20, Val55, Leu69-Met71 and Lys75, or are located at the outer surface of the C-terminal holo-CaM domain, i.e. Glu104, Arg106, His107, Arg126 and Asn129, were not considered for the calculation. Lys148, the C-terminal residue of CaM, was also rejected as constraint. The rest of the residues surpassing the $\Delta\delta_{cut\text{-}off}$, i.e. Val91, Phe92, Leu105, Val108, Ala128, Met145, Thr146 and Ala147, which are located in the inner cavity of the C-terminal CaM domain, were selected as active AIRs. Other residues defining this inner cavity, i.e. Ile85, Glu87, Ala88, Met109, Leu112, Met124, Ile125, Glu127 and Met144, were subsequently selected as passive AIRs.

In the case of FKBP38$^{290-313}$, the only residue selected as active AIR was Leu311, which displays dramatic changes both in the chemical shift values and in the signal line-width upon complex formation with holo-CaM or holo-CaM$^{76-148}$. In addition, all residues in the segment FKBP38$^{298-312}$ were selected as passive AIRs, with the exception of the residues Gln299 and Ala305, which were ^{15}N-labelled but displayed no significant effects upon complex formation. The segment FKBP38$^{290-297}$ was excluded as possible contact region, since this part of the protein (based on the expected similarity of the FKBP38 TPR domain of with those of FKBP51 and FKBP52) should be integrated in the structure of the TPR domain and therefore inaccessible for complex formation with CaM. Two residues in this segment, i.e. Leu292 and Ala297, were ^{15}N-labelled but not affected by the interaction with holo-CaM or holo-CaM$^{76-148}$, which supports the assumption that this segment is not involved in the interaction with CaM. Moreover, considering that Leu111 should be located inside the hydrophobic cavity of the C-terminal CaM domain, it is unlikely that a segment longer than 14 residues can fit into the narrow, ~18 Å long binding cleft, even in a helical arrangement.

The 20 structures obtained from the docking calculation of the FKBP38$^{290-313}$/holo-CaM complex can be grouped in three clusters (Figure 51A). Clusters I and cluster II, each consisting of 8 conformers, present the peptide in a similar orientation to that of other known CaM/peptide complexes, as for example the CaM/C20W complex (Elshort et al., 1999), whereas in cluster III, consisting of only 4 conformers, FKBP38$^{290-313}$ adopts a nearly perpendicular orientation (forming an angle of ~60º to the other two clusters). Moreover, the conformers from cluster III display significantly higher intermolecular energies, larger AIR violations (reflected by higher AIR energies) and lower BSA values compared to clusters I and II (Figure 51B), which is a strong indication that this smaller cluster does not represent a reasonable solution for the complex structure.

The remaining clusters I and II present much better structural statistics (Figure 51B), but differ from each other in the direction the FKBP38$^{290-313}$ molecule lies inside the hydrophobic cavity of the C-terminal CaM domain. While FKBP38$^{290-313}$ adopts in cluster II the opposite N-to-C direction as for example the C20W molecule in the CaM/C20W complex (Figure 51A), in cluster I it has the same direction as C20W, which is also observed in the vast majority hitherto reported CaM/peptide complex structures (Vetter and Leclerc, 2003; Ishida and Vogel, 2006). Unfortunately, no clear prediction can be made for one or the other direction based on the sequence of this FKBP38 segment, since (i) it shows no homology to other CaM-binding motifs and (ii) the balance of positively-charged amino acids at its N- and C-terminal ends is nearly equal.

A

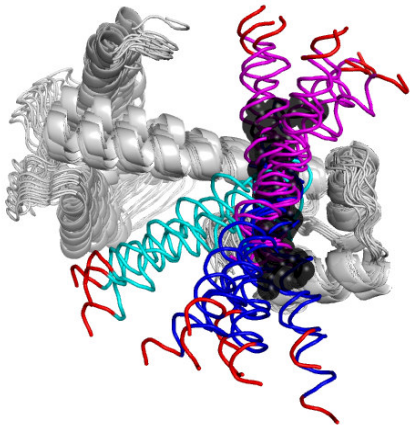

B

Cluster	No. conf.	E_{tot} (kcal/mol)	E_{AIRs} (kcal/mol)	BSA (Å^2)
I	8	-231.1 ± 82.5	0.01 ± 0.02	1510 ± 236
II	8	-189.7 ± 74.9	0.17 ± 0.40	1427 ± 127
III	4	-145.0 ± 71.3	1.60 ± 1.13	1132 ± 109

Figure 51. Calculated structures of the FKBP38$^{290\text{-}313}$/holo-CaM complex. (**A**) All 20 structures of the FKBP38$^{290\text{-}313}$/holo-CaM complex are shown. The C-terminal holo-CaM domains (gray ribbon) are superposed, while the FKBP38$^{290\text{-}313}$ molecules are represented in blue (cluster I), magenta (cluster II) or cyan (cluster III). The N-terminal ends of the FKBP38$^{290\text{-}313}$ molecules are highlighted in red. The backbone of the C20W molecule taken from the structure of its complex with CaM (PDB ID code 1CFF) is represented as CPK model in black. (**B**) Statistics table comparing average energies and BSAs of the three clusters obtained for the FKBP38$^{290\text{-}313}$/holo-CaM complex.

The direction found in cluster I, however, can be considered as the one most likely for the FKBP38$^{290\text{-}313}$/holo-CaM complex, as this cluster displays (i) the lowest average intermolecular energy, (ii) the highest average BSA, and (iii) the same direction as the majority of the known CaM/peptide complex structures. This cluster (Table 13) seems to be favored by better charge complementarities between the peptide and CaM, which stabilize the complex. Especially the lowest energy structure of this cluster, by far the one showing the lowest electrostatic, van der Waals and AIR energy values, and displaying a very similar backbone conformation as the CaM/C20W complex (Figure 52A), seems to be the best solution for the FKBP38$^{290\text{-}313}$/holo-CaM complex structure. In this structure, the side-chains of two hydrophobic residues, i.e. Tyr307 and Leu311, are anchoring the peptide inside the hydrophobic cavity of the C-terminal CaM domain, in addition to Glu303 (Figure 52A). Consequently, these side-chains belonging to FKBP38$^{290\text{-}313}$ interact with several hydrophobic residues in the CaM binding cavity. Moreover, the residues that were ^{15}N-labelled but displayed no chemical shift perturbations upon complex formation, i.e. Leu292, Ala297, Gln299 and Ala305, all show no contacts with CaM (Figure 52B), which provides further support for the selection of this structure.

The presence of a glutamate side-chain inside the hydrophobic cleft of CaM certainly is energetically not favored, also with respect to the acidic character of CaM. This could be the reason for the relatively low affinity of FKBP38$^{290\text{-}313}$ for CaM, as indicated by a K_D of 1.5 µM (Edlich et al., in preparation), whereas other CaM/peptide complexes feature dissociation constants in the nM range.

Table 13. Statistics of the 8 conformers belonging to cluster I of the FKBP38$^{290-313}$/holo-CaM complex, sorted according to their total intermolecular energy. The backbone RMSDs were calculated for the segment FKBP38$^{298-312}$ after superposition of CaM$^{85-145}$.

No.	Backbone RMSDs (Å)								Intermolecular energies (kcal/mol)				BSA (Å^2)
	1	14	2	7	8	18	9	13	total	vdw	elec	AIRs	
1	-								-395.5	-73.8	-321.7	0	1972
14	7.03	-							-286.9	-34.5	-252.4	0	1199
2	4.61	5.27	-						-254.1	-63.2	-190.8	0.01	1680
7	7.74	6.74	6.34	-					-243.7	-49.7	-194.0	0	1468
8	6.51	6.14	5.12	7.09	-				-180.3	-56.0	-124.3	0	1470
18	4.67	3.87	3.38	5.64	3.67	-			-176.4	-39.0	-137.4	0.07	1364
9	3.95	9.06	6.10	10.84	8.10	7.15	-		-159.1	-57.7	-101.4	0	1565
13	5.41	4.91	5.54	9.06	5.24	4.42	6.30	-	-153.1	-51.0	-102.0	0	1358
Ave.	RMSD = 6.07 ± 1.77								E_{total} = -231.1 ± 82.5 E_{vdw} = -53.1 ± 12.7 E_{elec} = -178.0 ± 78.2 E_{AIRs} = 0.01 ± 0.02 BSA = 1510 ± 236				

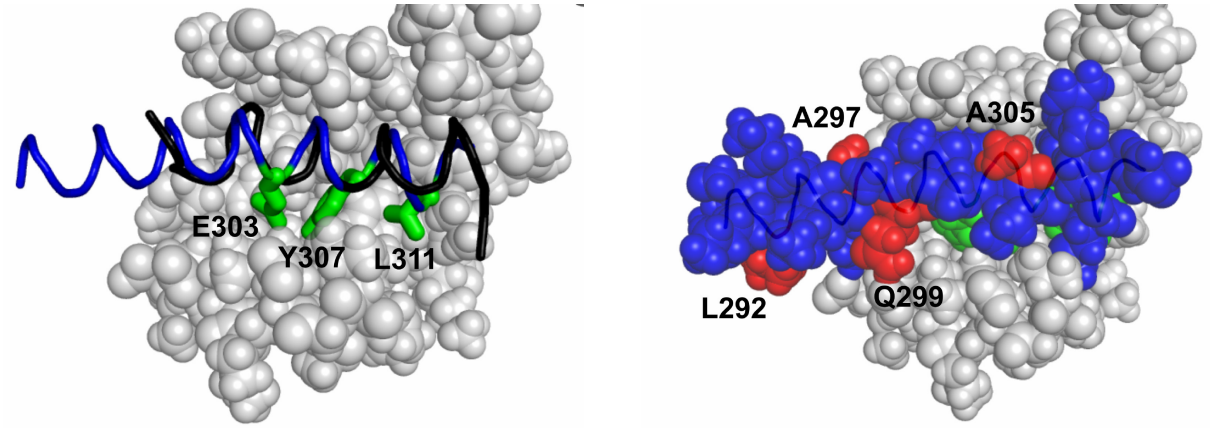

Figure 52. Structure of the FKBP38$^{290-313}$/holo-CaM complex. (**A**) The backbone traces of FKBP38$^{290-313}$ (blue) and C20W (black, from the CaM/C20W complex structure, PDB ID code 1CFF) are represented as ribbons, while holo-CaM is shown as CPK model. The side-chains of Glu303, Tyr307 and Leu311 from FKBP38$^{290-313}$ are represented as green stick models. (**B**) CPK model of the FKBP38$^{290-313}$/holo-CaM complex. CaM and FKBP38$^{290-313}$ are shown in light gray and blue, respectively. The residues Glu303, Tyr307 and Leu311, anchored to hydrophobic cavity of holo-CaM, are colored in green, while the residues Leu292, Ala297, Gln299 and Ala305, which show no direct contacts with holo-CaM, are highlighted in red.

3.6. Three-dimensional models of the overall FKBP38/CaM complexes

The three FKBP38/CaM complex structures determined in this work (i.e. FKBP38$^{35-153}$/apo-CaM, FKBP38$^{35-153}$/holo-CaM and FKBP38$^{290-313}$/holo-CaM) were finally combined to obtain models representing the FKBP38$^{35-313}$/semiloaded-CaM and FKBP38$^{35-313}$/holo-CaM complexes, which are considered to be the active forms of FKBP38 (Edlich et al., unpublished results). These overall complexes (Figure 53) display slightly different quaternary structures, as a result of the diverging relative arrangements found between the FKBP38$^{35-153}$/apo-CaM and FKBP38$^{35-153}$/holo-CaM complexes. Both models, however, seem to present a reasonable structural quality,

as neither the different protein domains nor the linker regions show any significant deformations. Thus, the TPR domains of both complexes (i.e. the segment FKBP38$^{155-281}$, which includes the three TPR motifs) display backbone conformations rather similar to that of FKBP51, as indicated by RMSDs of 1.75 and 2.03 Å for the FKBP38$^{35-313}$/semiloaded-CaM and FKBP38$^{35-313}$/holo-CaM complexes, respectively. Furthermore, the connecting CaM linkers display similar lengths as in other CaM complexes, comprising the segment Met76-Ser81 in the FKBP38$^{35-313}$/semiloaded-CaM complex and Arg74-Ser81 in the FKBP38$^{35-313}$/holo-CaM complex. These results therefore corroborate the feasibility of a complex that features two simultaneous binding interactions between FKBP38 and CaM.

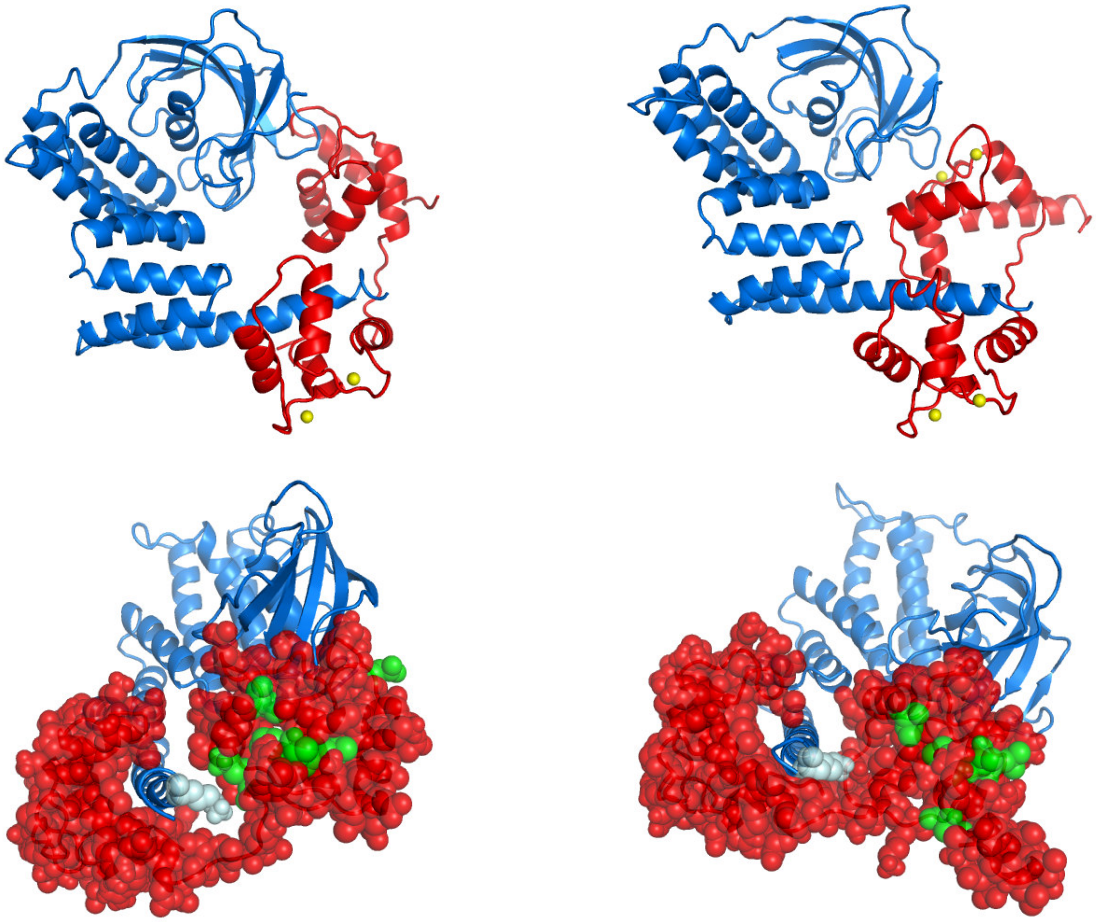

Figure 53. Structures of the FKBP38$^{35-313}$/semiloaded-CaM (**upper panel left**) and FKBP38$^{35-313}$/holo-CaM (**upper panel right**) complexes. The backbone traces of FKBP38$^{35-313}$ (blue) and CaM (red) are represented as ribbons and the Ca^{2+} atoms as yellow spheres. The TPR domains of FKBP38 are presented in the same orientation. In the **lower panel**, the CaM molecules are shown as CPK models, with the residues in the N-terminal CaM domain that displayed chemical shift changes upon binding to FKBP38$^{290-313}$ (i.e. Asp20, Leu69, Thr70, Met71 and Lys75) highlighted in green. Residue Lys309 of FKBP38, which extends towards the N-terminal CaM domain, is also shown as CPK model in light cyan.

In both structures, the CaM molecule is partially wrapped - to a higher or lower extent - around the CaM-binding site of FKBP38 (Figure 53, lower panel). As a consequence, the Lys309 side-chain of FKBP38, which is part of this CaM-binding site, is oriented in both structures towards

the N-terminal CaM domain. This may explain the chemical shift perturbations observed at the N-terminal CaM domain upon complex formation with $FKBP38^{290-313}$ (see section 3.5.).

Interestingly, both models show no additional interactions between the TPR domain of FKBP38 and the CaM molecule. Therefore, the overall FKBP38/CaM complex can be considered as a combination of two individual (i.e. C-terminal ↔ C-terminal and N-terminal ↔ N-terminal) binding modes, lacking any additional stabilizing interactions to those already observed in the individual binding modes. This result is in good agreement with (i) the relatively low binding affinity between both proteins and (ii) with the observation that the affinity of $FKBP38^{290-313}$ to CaM is comparable to that of the entire FKBP38 molecule, as revealed by competition assays and ITC experiments (Edlich et al., in preparation).

3.6.1. Comparison of the overall $FKBP38^{35-313}$/CaM complexes with other known CaM complexes

The three-dimensional structures of the $FKBP38^{35-313}$/CaM complexes display certain similarities to other known CaM/target protein structures. For example, the binding of $FKBP38^{290-313}$ to the CaM C-terminal domain resembles the CaM/C20W complex (Elshort et al., 1999), which was already discussed in detail in section 3.5.1. The most remarkable similitude, however, can be found when $FKBP38^{35-313}$/CaM is compared to the complex of CaM with the exotoxin edema factor from *Bacillus anthracis* (Drum et al., 2002).

In both CaM complexes (Figure 54), interactions occur between both CaM domains and different parts of the target proteins (either FKBP38 or edema factor). First, a helical part of the target protein (i.e. segment Arg300-Asn313 in FKBP38 and segment Asn521-Tyr536 in edema factor) binds to the hydrophobic cleft of the Ca^{2+}-loaded C-terminal CaM domain. Furthermore, in the complex with edema factor the CaM molecule is tightly inserted between the CA domain and the helical domain of the edema factor, which results in several additional interactions of both CaM domains with the target protein, whereas in the $FKBP38^{35-313}$/CaM complex the only additional interaction occurs between the N-terminal CaM domain (i.e. a surface region centered at the Ca^{2+}-binding sites) and the catalytic domain of FKBP38. As a result, there is a significant difference in the binding affinities of CaM for edema factor ($K_D \sim 10^{-10}$ M) and FKBP38 ($K_D \sim 10^{-6}$ M).

Another difference between the two complexes is that the CaM molecule adopts different inter-

domain orientations in both structures. In the edema factor/CaM complex the CaM molecule is extended, whereas in the FKBP38$^{35\text{-}313}$/CaM complex it is partially wrapped around the FKBP38$^{300\text{-}313}$ segment. Moreover, the N-terminal CaM domain is Ca^{2+}-free in the edema factor complex, while it can be either Ca^{2+}-free or Ca^{2+}-bound in the complex with FKBP38.

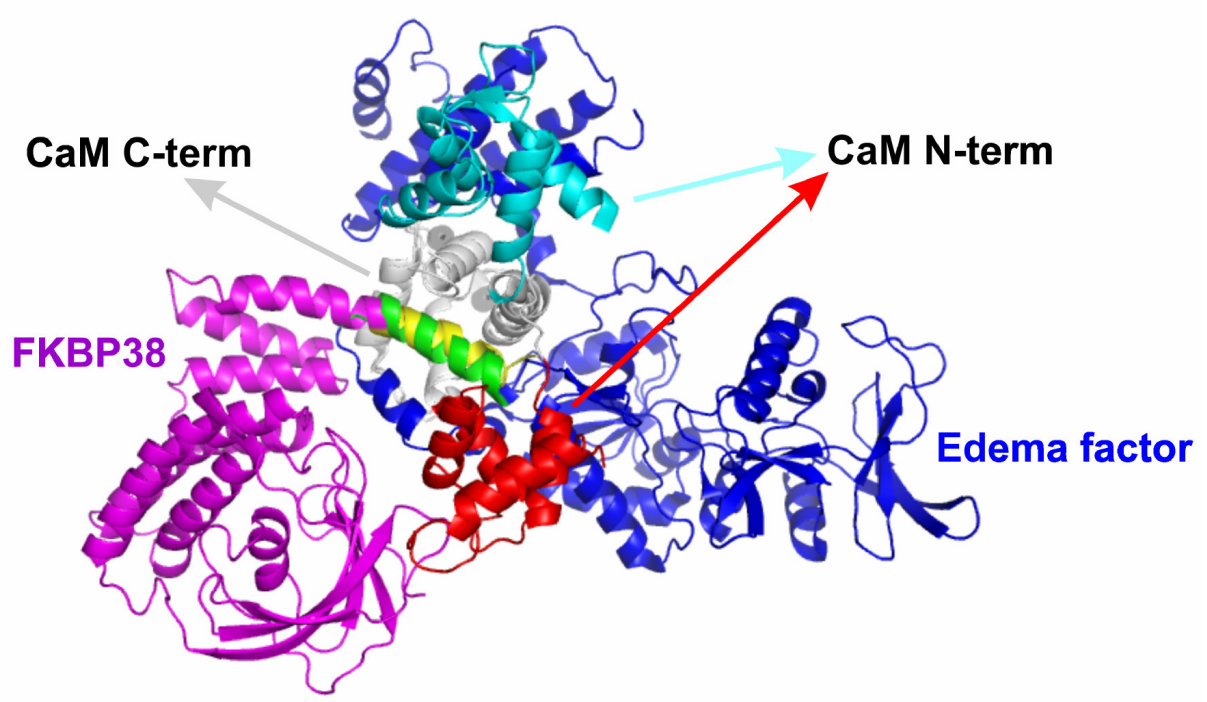

Figure 54. Comparison of the overall structures of the edema factor/CaM and FKBP38$^{35\text{-}313}$/semiloaded-CaM complexes. The C-terminal CaM domains (grey) are superposed, while the N-terminal CaM domains are colored in red (edema factor/CaM) and cyan (FKBP38$^{35\text{-}313}$/semiloaded-CaM). The helical target protein segments bound to the C-terminal CaM domain are highlighted in green (edema factor/CaM) and yellow (FKBP38$^{35\text{-}313}$/semiloaded-CaM).

In both systems, the result of complex formation is an activation of the respective target protein. However, in the edema factor complex this activation is the result of a formation of an active site by protein regions that were solvent exposed in absence of CaM, in what has been referred to as an "active site remodeling" activation mechanism. In the FKBP38 complex, however, the activation seems to be the result of very subtle structural modifications which the N-terminal CaM domain introduces in the catalytic domain of FKBP38, influencing the βD strand and the βE-βF loop of this FKBP domain. Up to date, no structure has been published which displays similar interactions as those found between FKBP38 and CaM. Hence, the FKBP38/CaM system features a novel scenario of enzyme activation by CaM: the C-terminal CaM domain binds to a part of the target molecule (i.e. the CaM-binding site of FKBP38) with higher affinity, subsequently facilitating the lower affinity interaction of the N-terminal CaM domain with a second (in this case the catalytic) domain of the enzyme, thereby producing small conformational changes which lead to activation.

4. Summary

The human FKBP38 is a peptidyl prolyl *cis/trans* isomerase of the FKBP (FK506-binding protein) family, which has been found to play a key role in neuronal apoptosis. This constitutively inactive protein is the first PPIase that has been found to be regulated by calmodulin (CaM) and calcium (Ca^{2+}), as only the FKBP38/CaM/Ca^{2+} complex displays FKBP activity and can inhibit the anti-apoptotic effector Bcl-2. The main aims of this work are the structural study of (i) the catalytic (FKBP) domain of FKBP38 and (ii) the interactions of FKBP38 with CaM/Ca^{2+}, which lead to its activation. The following results have been obtained:

- A construct comprising the catalytic domain of human FKBP38, $FKBP38^{35-153}$, was successfully cloned, expressed and purified for biochemical and structural studies. This construct displays a reasonable stability. It was expressed and purified in large amounts suitable for both the preparation of isotopically labelled NMR samples and crystallization.
- All ^{1}H and ^{15}N resonances of $FKBP38^{35-153}$ were assigned. The good signal dispersion of these resonances provided the basis for an NMR-based structure elucidation and for the study of its interactions with CaM and Ca^{2+}.
- The three-dimensional structure of $FKBP38^{35-153}$ was determined by high-resolution NMR spectroscopy. It displays the typical "half β-barrel" fold of FKBP domains. This structure explains the lack of FKBP activity of $FKBP38^{35-153}$ due to specific differences between $FKBP38^{35-153}$ and FKBP12. More precisely: (i) the lack of a loop that disrupts the βD strand is missing in $FKBP38^{35-153}$ and (ii) the long βE-βF loop blocks the entry portal to the "active site" of $FKBP38^{35-153}$. Considerable differences in the net charge around the active site between $FKBP38^{35-153}$ and FKBP12 could also play a role in the substrate discrimination.
- The structure of $FKBP38^{35-153}$ cannot mimic that of the FKBP12/FK506 complex. This supports the observation that FKBP38 cannot inhibit the protein phosphatase calcineurin in absence of bound FK506.
- For the first time, a weak binding of Ca^{2+} to an FKBP domain has been demonstrated in the case of $FKBP38^{35-153}$. The binding of Ca^{2+} (and also Mg^{2+}) to the βD-α loop of $FKBP38^{35-153}$ has been characterized by NMR chemical shift perturbation mapping, ITC experiments and fluorescence spectroscopy. Structural insight into this binding event was provided by a crystal structure of $FKBP38^{35-153}$, which has been determined at 1.05 Å resolution. The binding of Ca^{2+} to $FKBP38^{35-153}$ might be related to a further regulation of the interaction(s) between FKBP38 and Bcl-2.
- The backbone ^{1}H and ^{15}N amide resonances of apo- and holo-CaM were completely assigned

at the conditions used in the present study. These assignments allowed the investigation of the interactions of both CaM forms with FKBP38 by means of chemical shift perturbation mapping.

- Apo-CaM binds to a surface centered at the βC-βD loop of $FKBP38^{35-153}$.
- $FKBP38^{35-153}$ binds to the N-terminal domain of both apo- and holo-CaM. These interactions are centered at the AB and BC loops of CaM. No interactions were found with the C-terminal CaM domain. The backbone conformation of the CaM segments involved in the interaction with $FKBP38^{35-153}$ is very similar in both CaM forms, which most likely is the reason for the Ca^{2+}-independence of this interaction.
- The structures of $FKBP38^{35-153}$ in complex with apo- and holo-CaM were elucidated by docking calculations using the information provided by the chemical shift perturbation experiments. These structures provide an explanation for the activation of FKBP38 upon CaM binding, since both CaM forms interact with the βC-βD loop. This may result in conformational changes either in the Glu83 side-chain or in the long βE-βF loop, which are both possible factors with respect to the inherent lack of activity of $FKBP38^{35-153}$.
- A peptide comprising the CaM binding site of FKBP38, i.e. the segment $FKBP38^{290-313}$, was completely assigned for the study of its interactions with holo-CaM.
- $FKBP38^{290-313}$ binds to the hydrophobic cavity of the C-terminal holo-CaM domain.
- The structure of the $FKBP38^{290-313}$/holo-CaM complex was determined by means of docking calculations. This complex resembles the structure of holo-CaM in complex with the C20W peptide from the plasma membrane Ca^{2+} pump, where the peptide is bound only to the C-terminal CaM domain. The insertion of the Glu303 side-chain into the hydrophobic binding cavity of CaM may provide an explanation for the relatively low binding affinity of FKBP38.
- Overall model structures of the $FKBP38^{35-313}$/holo-CaM and $FKBP38^{35-313}$/semiloaded-CaM complexes were simulated by means of molecular dynamics calculations. These structures seem to be reasonable approximations of the active FKBP38/CaM/Ca^{2+} complexes and are in good agreement with the biophysical data that is presently available.
- A comparison of the structures of the $FKBP38^{35-313}$/CaM complexes with the edema factor/CaM complex reveals certain similarities. Differences in the enzyme activation exist, however, as the activation of FKBP38 originates from subtle structural modifications caused in its catalytic domain by the interaction with CaM. Hence, the activation of FKBP38 by CaM represents a novel scenario of enzyme activation by CaM.

The activation of FKBP38 by CaM can be summarized as the result of the formation of a 1:1 complex between both proteins, which features two binding modes: one between the CaM-

binding site of FKBP38 and the Ca^{2+}-bound C-terminal CaM domain, and another between the catalytic FKBP domain of FKBP38 and the N-terminal CaM domain that is Ca^{2+} independent. The latter interaction apparently causes certain conformational changes in the FKBP domain that lead to the activation of FKBP38 upon CaM/Ca^{2+} binding. Further investigations will be needed to determine the structural basis of substrate binding to the activated FKBP38/CaM/Ca^{2+} complex.

5. References

Altschul S.F., Gish W., Miller W., Myers E.W. and Lipman D.J. (1990) Basic local alignment search tool. *J. Mol. Biol.* **215**, 403-410.

Andreotti A.H. (2003) Native state proline isomerization: an intrinsic molecular switch. *Biochemistry* **42**, 9515-9524.

Anfinsen C.B. (1973) Principles that govern the folding of protein chains. *Science* **181**, 223-230.

Babu Y.S., Bugg C.E. and Cook W.J. (1988) Structure of calmodulin refined at 2.2 Å resolution. *J. Mol. Biol.* **204**, 191–204.

Babu Y.S., Sack J.S., Greenhough T.J., Bugg C.E., Means A.R. and Cook W.J. (1985) Three-dimensional structure of calmodulin. *Nature* **315**, 37–40.

Barbato G., Ikura M., Kay L.E. and Bax A. (1992) Backbone dynamics of calmodulin studied by ^{15}N relaxation using inverse detected two-dimensional spectroscopy: The central loop is flexible. *Biochemistry* **31**, 5269-5278.

Barent R.L., Nair S.C., Carr D.C., Ruan Y., Rimerman R.A., Fulton J., Zhang Y. and Smith D.F. (1998) Analysis of FKBP51/FKBP52 chimeras and mutants for Hsp90 binding and association with progesterone receptor complexes. *Mol. Endocrinol.* **12**, 342-354.

Berendsen H.J.C., Postma J.P.M., DiNola A. and Haak J.R. (1984) Molecular dynamics with coupling to an external bath. *J. Chem. Phys.* **81**, 3684–3690.

Berendsen H.J.C., Postma J.P.M., van Gunsteren W.F. and Hermans J. (1981) Interaction models for water in relation to protein hydration. In: *Intermolecular Forces.* Pullman, B. ed. D. Reidel Publishing Company, Dordrecht, 331–342.

Berridge M.J. (1990) Calcium oscillations. *J. Biol. Chem.* **265**, 9583-9586.

Berridge M.J., Bootman M.D. and Lipp P. (1998) Calcium - a life and death signal. *Nature* **395**, 645-648.

Berridge M.J., Lipp P. and Bootman M.D. (2000) The versatility and universality of calcium signalling. *Nat. Rev. Mol. Cell Biol.* **1**, 11–21.

Bootman M.D., Collins T.J., Peppiatt C.M., Prothero L.S., MacKenzie L., De Smet P., Travers M., Tovey S.C., Seo J.T., Berridge M.J., Ciccolini F. and Lipp P. (2001) Calcium signaling - an overview. *Semin. Cell Dev. Biol.* **12**, 3-10.

Brandts J.F., Halvorson H.R. and Brennan M. (1975) Consideration of the possibility that the slow step in protein denaturation reactions is due to cis-trans isomerism of proline residues. *Biochemistry* **14**, 4953-4963.

Braunewell K.H. (2005) The darker side of Ca^{2+} signaling by neuronal Ca^{2+}-sensor proteins: from Alzheimer's disease to cancer. *Trends Pharmacol. Sci.* **26**, 345-351.

Brunger A.T., Adams P.D., Clore G.M., DeLano W.L., Gros P., Grosse-Kunstleve R.W., Jiang J.S., Kuszewski J., Nilges J., Pannu N.S., Read R.J., Rice L.M., Simonson T. and Warren G.L. (1998) Crystallography & NMR system: A new software suite for macromolecular structure determination. *Acta Crystallogr. Sect. D Biol. Crystallogr.* **54**, 905–921

Bukau B., Weissman J. and Horwich A. (2006). Molecular chaperones and protein quality control. *Cell* **125**, 443-451.

Carafoli E. (2002) Calcium signaling: a tale for all seasons. *Proc. Natl. Acad. Sci. USA* **99**, 1115-1122.

Carafoli E., Santella L., Branca D. and Brini M. (2001) Generation, control and processing of calcium signals. *Crit. Rev. Biochem. Mol. Biol.* **36**, 107-260.

Chattopadhyaya R., Meador W.E., Means A.R. and Quiocho F.A. (1992) Calmodulin structure refined at 1.7 Angstroms resolution. *J. Mol. Biol.* **228**, 1177-1192.

Chaudhuri T.K. and Paul S. (2006) Protein-misfolding diseases and chaperone-based therapeutic approaches. *FEBS J.* **273**, 1331-1349.

Chazin W.J. (1995) Releasing the calcium trigger. *Nat. Struct. Biol.* **2**, 707–710.

Chin D. and Means A.R. (2000) Calmodulin: a prototypical calcium sensor. *Trends Cell Biol.* **10**, 322-328.

Chou J.J., Li S., Klee C.B. and Bax A. (2001) Solution structure of Ca^{2+}-calmodulin reveals flexible hand-like properties of its domains. *Nat. Struct. Biol.* **8**, 990–997.

Cohen F.E. and Kelly J.W. (2003) Therapeutic approaches to protein-misfolding diseases. *Nature* **426**, 905-909.

Cohen P. and Klee C.B., Eds. (1988) *Calmodulin,* Elsevier, New York.

Crackower M.A., Kolas N.K., Noguchi J., Sarao R., Kikuchi K., Kaneko H., Kobayashi E., Kawai Y., Kozieradzki I., Landers R., Mo R., Hui C.C., Nieves E., Cohen P.E., Osborne L.R., Wada T., Kunieda T., Moens P.B. and Penninger J.M. (2003) Essential role of Fkbp6 in male fertility and homologous chromosome pairing in meiosis. *Science* **300**, 1291-1295.

Crivici A. and Ikura M. (1995) Molecular and structural basis of target recognition by calmodulin. *Annu. Rev. Biophys. Biomol. Struct.* **24,** 85–116.

Darden T., York D. and Pedersen L. (1993) Particle mesh Ewald: An N-log(N) method for Ewald sums in large systems. *J. Chem. Phys.* **98**, 10089–10092.

Dauber-Osguthorpe P., Roberts V.A., Osguthorpe D.J., Wolff D.J., Genest M. and Hagler A.T. (1988) Structure and energetics of ligand binding to proteins: Escherichia coli dihydrofolate reductase-trimethoprim, a drug-receptor system. *Proteins* **4**, 31-47.

Dominguez C., Boelens R. and Bonvin A.M. (2003) HADDOCK: a protein-protein docking approach based on biochemical or biophysical information. *J. Am. Chem. Soc.* **125**, 1731–1737.

Drum C.L., Yan S.Z., Bard J., Shen Y.Q., Lu D., Soelaiman S., Grabarek Z., Bohm A. and Tang W.J. (2002) Structural basis for the activation of anthrax adenylyl cyclase exotoxin by calmodulin. *Nature* **415**, 396–402.

Edlich F., Erdmann F., Jarczowski F., Moutty M.C., Weiwad M. and Fischer G. (2007) The Bcl-2 regulator FKBP38-calmodulin-Ca^{2+} is inhibited by Hsp90. *J. Biol. Chem.* **282**, 15341-15348.

Edlich F., Maestre-Martinez M., Jarczowski F., Weiwad M., Moutty M.C., Malesevic M., Jahreis G., Lücke C. and Fischer G. (In preparation)

Edlich F., Weiwad M., Erdmann F., Fanghänel J., Jarczowski F., Rahfeld J.U. and Fischer G. (2005) Bcl-2 regulator FKBP38 is activated by Ca^{2+}/calmodulin. *EMBO Journal* **24**, 2688-2699.

Edlich F., Weiwad M., Wildemann D., Jarczowski F., Kilka S., Moutty M.C., Jahreis G., Lücke C., Schmidt W., Striggow F. and Fischer G. (2006) The specific FKBP38 inhibitor N-(N',N'-dimethylcarboxamidomethyl)cycloheximide has potent neuroprotective and neurotrophic properties in brain ischemia. *J. Biol. Chem.* **281**, 14961-14970.

Eldik L.J. and Watterson D.M. (1998) *Calmodulin and signal transduction* (Van Eldik, L.J. & Watterson, D.M., eds.). Academic Press, New York, USA.

Ellgard L. and Ruddock L.W. (2005) The human protein disulphide isomerase family: substrate interactions and functional properties. *EMBO Rep.* **6**, 28-32.

Elshorst B., Hennig M., Försterling H., Diener A., Maurer M., Schulte P., Schwalbe H., Griesinger C., Krebs J., Schmid H., Vorherr T. and Carafoli E. (1999) NMR solution structure of a complex of calmodulin with a binding peptide of the Ca^{2+} pump. *Biochemistry* **38**, 12320-12332.

Evenas J., Malmendal A. and Forsen, S. (1998) Calcium. *Curr. Opin. Chem. Biol.* **2**, 293–302.

Essmann U., Perera L., Berkowitz M.L., Darden T., Lee H. and Pedersen L.G. (1995) A smooth particle mesh Ewald potential. *J. Chem. Phys.* **103**, 8577–8592.

Fanghänel J. and Fischer G. (2004) Insights into the catalytic mechanism of peptidyl prolyl cis/trans isomerases. *Front. Biosci.* **9**, 3453-3478.

Fingar D.C. and Blenis J. (2004) Target of rapamycin (TOR): an integrator of nutrient and growth factor signals and coordinator of cell growth and cell cycle progression. *Oncogene* **23**, 3151-3171.

Finn B.E., Evenas J., Drakenberg T., Waltho J.P., Thulin E. and Forsen S. (1995) Calcium-induced structural changes and domain autonomy in calmodulin. *Nat. Struct. Biol.* **2**, 777–783.

Fischer G. (1994) Peptidyl-prolyl cis/trans isomerases and their effectors. *Angew. Chem. Int. Ed. Engl.* **33**, 1415-1436.

Fischer G. and Aumüller T. (2003) Regulation of peptide bond cis/trans isomerization by enzyme catalysis and its implication in physiological processes. *Rev. Physiol. Biochem.*

Pharmacol. **148**, 105–150.

Fischer G., Wittmann-Liebold B., Lang K., Kiefhaber T. and Schmid F.X. (1989) Cyclophilin and peptidyl-prolyl cis-trans isomerase are probably identical proteins. *Nature* **337**, 476-478.

Galat A. (2004a) Function-dependent clustering of orthologues and paralogues of cyclophilins. *Proteins* **56**, 808-820.

Galat A. (2004b) A note on clustering the functionally-related paralogues and orthologues of proteins: a case of the FK506-binding proteins (FKBPs). *Comput Biol Chem.* **28**, 129-140.

Geisler M., Kolukisaoglu H.U., Bouchard R., Billion K., Berger J., Saal B., Frangne N., Koncz-Kalman Z., Koncz C., Dudler R., Blakeslee J.J., Murphy A.S., Martinoia E. and Schulz B. (2003) TWISTED DWARF1, a unique plasma membrane-anchored immunophilin-like protein, interacts with Arabidopsis multidrug resistance-like transporters AtPGP1 and AtPGP19. *Mol. Biol. Cell* **14**, 4238-4249.

Gellman S.H. (1991) On the role of methionine residues in the sequence-independent recognition of nonpolar protein surfaces. *Biochemistry* **30**, 6633–6636.

Gill S.C. and von Hippel P.H. (1989) Calculation of protein extinction coefficients from amino acid sequence data. *Anal. Biochem.* **182**, 319-326. [Erratum in: *Anal. Biochem.* (1990) **189**, 283.]

Gilli R., Lafitte D., Lopez C., Kilhoffer M., Makarov A., Briand C. and Haiech J. (1998) Thermodynamic analysis of calcium and magnesium binding to calmodulin. *Biochemistry* **37**, 5450-5456.

Granzin J., Eckhoff A. and Weiergraber O.H. (2006) Crystal structure of a multi-domain immunophilin from Arabidopsis thaliana: a paradigm for regulation of plant ABC transporters. *J. Mol. Biol.* **364**, 799-809.

Griffith J.P., Kim J.L., Kim E.E., Sintchak M.D., Thomson J.A., Fitzgibbon M.J., Fleming M.A., Caron P.R., Hsiao K. and Navia M.A. (1995) X-ray structure of calcineurin inhibited by the immunophilin-immunosuppressant FKBP12-FK506 complex. *Cell* **82**, 507-522.

Güntert P., Braun W. and Wüthrich K. (1991) Efficient computation of three-dimensional protein structures in solution from nuclear magnetic resonance data using the program DIANA and the supporting programs CALIBA, HABAS and GLOMSA. *J. Mol. Biol.* **217**, 517-530.

Güntert P., Mumenthaler C. and Wüthrich K. (1997) Torsion angle dynamics for NMR structure calculation with the new program DYANA. *J. Mol. Biol.* **273**, 283-298.

Hartl F.U. (1996) Molecular chaperones in cellular protein folding. *Nature* **381**, 571-579.

Hess B., Bekker H., Berendsen H.J.C. and Fraaije J.G.E.M. (1997) LINCS: A linear constraint solver for molecular simulations. *J. Comp. Chem.* **18**, 1463–1472.

Hoeflich K.P. and Ikura M. (2002) Calmodulin in action: diversity in target recognition and activation mechanisms. *Cell* **108**, 739–742.

Hubbard S.J. and Thornton J.M. (1993) *NACCESS Computer Program*, Department of Biochemistry and Molecular Biology, University College London, London, UK.

Ikura M., Kay L.E. and Bax A. (1990) A novel approach for sequential assignment of ^{1}H, ^{13}C, and ^{15}N spectra of proteins: heteronuclear triple-resonance three-dimensional NMR spectroscopy. Application to calmodulin. *Biochemistry* **29**, 4659-4667.

Ikura, M. (1996) Calcium binding and conformational response in EF-hand proteins. *Trends Biochem. Sci.* **21**, 14–17.

Ishida I. and Vogel H.J. (2006) Protein-peptide interaction studies demonstrate the versatility of calmodulin target protein binding. *Protein Pep. Lett.* **13**, 455-465

Jorgensen W.L., Chandrasekhar J., Madura J.D., Impey R.W. and Klein M.L. (1983) Comparison of simple potential functions for simulating liquid water. *J. Chem. Phys.* **79**, 926–935.

Jurado L.A., Chockalingam P.S. and Jarrett H.W. (1999) Apocalmodulin. *Physiol Rev.* **79,** 661–682.

Kamphausen T., Fanghänel J., Neumann D., Schulz B. and Rahfeld J.U. (2002) Characterization of Arabidopsis thaliana AtFKBP42 that is membrane-bound and interacts with HSP90. *Plant J.* **32**, 263–276.

Kang C.B., Feng L., Chia J. and Yoon H.S. (2005) Molecular characterization of FK-506 binding protein 38 and its potential regulatory role on the anti-apoptotic protein Bcl-2. *Biochem. Biophys. Res. Commun.* **337**, 30-38.

Kissinger C.R., Parge H.E., Knighton D.R., Lewis C.T., Pelletier L.A., Tempczyk A., Kalish V.J., Tucker K.D., Showalter R.E., Moomaw E.W., Gastinel L.N., Habuka N., Chen X., Maldonado F., Barker J.E., Bacquet R. and Villafranca J.E. (1995) Crystal structures of human calcineurin and the human FKBP12-FK506-calcineurin complex. *Nature* **278**, 641-644

Kretsinger R.H. (1996) EF-hands reach out. *Nat. Struct. Biol.* **3**, 12–15.

Kuboniwa H., Tjandra N., Grzesiek S., Ren H., Klee C.B. and Bax A. (1995) Solution structure of calcium-free calmodulin. *Nat. Struct. Biol.* **2**, 768-776.

Laemmli U.K. (1970) Cleavage of structural proteins during the assembly of the head of bacteriophage T4. *Nature* **227**, 680-685.

Lam E., Martin M. and Wiederrecht G. (1995) Isolation of a cDNA encoding a novel human FK506-binding protein homolog containing leucine zipper and tetratricopeptide repeat motifs. *Gene* **160**, 297-302.

Laskowski R.A., Rullmann J.A., MacArthur M.W., Kaptein R. and Thornton J.M. (1996) AQUA and PROCHECK-NMR: Programs for checking the quality of protein structures solved by NMR *J. Biomol. NMR* **8**, 477-486.

Leslie A.G.W. (1994) MOSFLM *User Guide* (Medical Research Council (MRC), Laboratory of Molecular Biology, Cambridge, U.K.). Version 5.30.

Lewit-Bentley A. and Rety S. (2000) EF-hand calcium-binding proteins. *Curr. Opin. Struct. Biol.* **10**, 637–643.

Lin D.T. and Lechleiter J.D. (2002) Mitochondrial targeted cyclophilin D protects cells from cell death by peptidyl prolyl isomerization. *J. Biol. Chem.* **277**, 31134-31141.

Linge J.P., O'Donoghue S.I. and Nilges M. (2001) Automated assignment of ambiguous nuclear overhauser effects with ARIA. *Methods Enzymol.* **339**, 71–90.

Liu J., Farmer J.D., Jr. Lane W.S., Friedman J., Weissman I. and Schreiber S.L. (1991) Calcineurin is a common target of cyclophilin-cyclosporin A and FKBP-FK506 complexes. *Cell* **66**, 807–815.

McCaffrey P.G., Perrino B.A., Soderling T.R. and Rao A. (1993) NF-ATp, a T lymphocyte DNA-binding protein that is a target for calcineurin and immunosuppressive drugs. *J. Biol. Chem.* **268**, 3747-3752.

Meador W.E., Means A.R. and Quiocho F.A. (1992) Target enzyme recognition by calmodulin: 2.4 Å structure of a calmodulin-peptide complex. *Science* **257,** 1251–1255.

Meng X., Lu X., Morris C.A. and Keating M.T. (1998) A novel human gene FKBP6 is deleted in Williams syndrome. *Genomics* **52**, 130-137.

Meyer T. and Stryer L. (1991) Calcium spiking. *Ann. Rev. Biophys. Chem.* **20**, 153-174.

Michnick S.W., Rosen M.K., Wandless T.J., Karplus M. and Schreiber S.L. (1991) Solution structure of FKBP, a rotamase enzyme and receptor for FK506 and Rapamycin. *Science* **251**, 836-839.

Moutty M.C. (2006) Interaktion von FKBP mit TPR-Motiven in Multiproteinkomplexen. Ph.D. Thesis, Martin-Luther-Universität, Halle-Wittenberg.

Muhandiram D.R. and Kay L.E. (1994) Gradient-enhanced triple-resonance three-dimensional NMR experiments with improved sensitivity *J. Magn. Reson., Ser. B* **103**, 203–216.

Mulder F.A., Schipper D., Bott R. and Boelens R. (1999) Altered flexibility in the substrate-binding site of related native and engineered high-alkaline Bacillus subtilisins. *J. Mol. Biol.* **292**, 111–123.

Mullis K.B. and Faloona F.A. (1987) Specific synthesis of DNA in vitro via a polymerase-catalyzed chain reaction. *Methods Enzymol.* **155**, 335-50.

Nelson M.R. and Chazin W.J. (1998) Structures of EF-hand Ca^{2+}-binding proteins: diversity in the organization, packing and response to Ca^{2+}-binding. *Biometals* **11**, 297–318.

Nielsen J.V., Mitchelmore C., Pedersen K.M., Kjaerulff K.M., Finsen B. and Jensen N.A. (2004) Fkbp8: novel isoforms, genomic organization, and characterization of a forebrain promoter in transgenic mice. *Genomics* **83**, 181-192.

Ogawa Y. and Tanokura M. (1984) Calcium binding to calmodulin: effects of ionic strength, Mg^{2+}, pH and temperature. *J. Biochem.* (Tokyo) **95**, 19-28.

Okamoto T., Nishimura Y., Ichimura T., Suzuki K., Miyamura T., Suzuki T., Moriishi K. And Matsuura Y. (2006) Hepatitis C virus RNA replication is regulated by FKBP8 and Hsp90. *EMBO Journal* **25**, 5015-5025. [Erratum in *EMBO Journal* (2006) **25**, 5634]

Osawa M., Tokumitsu H., Swindells M.B., Kurihara H., Orita M., Shibanuma T., Furuya T. and Ikura M. (1999) A novel target recognition revealed by calmodulin in complex with Ca^{2+}-calmodulin-dependent kinase kinase. *Nat. Struct. Biol.* **6**, 819–824.

Park S.T., Aldape R.A., Futer O., DeCenzo M.T. and Livingston D.J. (1992) PPIase catalysis by human FK506-binding protein proceeds through a conformational twist mechanism. *J. Biol. Chem.* **267**, 3316-3324.

Potter J.D., Strang-Brown P., Walker P.L. and Iida S. (1983) Ca^{2+} binding to calmodulin. *Methods Enzymol.* **102**, 135-143.

Pratt W.B., Silverstein A.M. and Galigniana M.D. (1999) A model for the cytoplasmic trafficking of signalling proteins involving the hsp90-binding immunophilins and p50cdc37. *Cell Signal.* **11**, 839-851.

Pristovšek P., Lücke C., Reincke B., Ludwig B. and Rüterjans H. (2000) Solution structure of the functional domain of Paracoccus denitrificans cytochrome c552 in the reduced state. *Eur. J. Biochem.* **267**, 4205-4212.

Ramamurthy V., Roberts M., van den Akker F., Niemi G., Reh T.A. and Hurley J.B. (2003) AIPL1, a protein implicated in Leber's congenital amaurosis, interacts with and aids in processing of farnesylated proteins. *Proc. Natl. Acad. Sci. USA* **100**, 12630-12635.

Rhoads A.R. and Friedberg F. (1997) Sequence motifs for calmodulin recognition. *FASEB J.* **11,** 331–340.

Rosen M.K., Standaert R.F., Galat A., Nakatsuka M. and Schreiber S.L. (1990) Inhibition of FKBP rotamase activity by immunosuppressant FK506: twisted amide surrogate. *Science* **248**, 863-866.

Rosner M., Hofer K., Kubista M. and Hengstschlager M. (2003) Cell size regulation by the human TSC tumor suppressor proteins depends on PI3K and FKBP38. *Oncogene* **22**, 4786-4798.

Sabers C.J., Martin M.M., Brunn G.J., Williams J.M., Dumont F.J., Wiederrecht G. and Abraham R.T. (1995) Isolation of a protein target of the FKBP12-rapamycin complex in mammalian cells. *J. Biol. Chem.* **270**, 815-822.

Saiki R.K., Gelfand D.H., Stoffel S., Scharf S.J. Higuchi R., Horn G.T., Mullis K.B. and Erlich H.A. (1988) Primer-directed enzymatic amplification of DNA with a thermostable DNA polymerase. *Science* **239**, 487-491.

Schiene-Fischer C., Habazettl J., Schmid F.X. and Fischer G. (2002) The hsp70 chaperone DnaK is a secondary amide peptide bond cis-trans isomerase. *Nat Struct Biol.* **9**, 419-424.

Schumacher M.A., Rivard A.F., Bachinger H.P. and Adelman J.P. (2001) Structure of the gating domain of a Ca^{2+}-activated K^+ channel complexed with Ca^{2+}/calmodulin. *Nature* **410,** 1120–1124.

Sekerina E., Rahfeld J.U., Müller J., Fanghänel J., Rascher C., Fischer G. and Bayer P. (2000) NMR solution structure of hPar14 reveals similarity to the peptidyl prolyl *cis/trans* isomerase domain of the mitotic regulator hPin1 but indicates a different functionality of the protein. *J. Mol. Biol.* 301, 1003-1017.

Shibasaki F., Price E.R., Milan D. and McKeon F. (1996) Role of kinases and the phosphatase calcineurin in the nuclear shuttling of transcription factor NF-AT4. Nature **382**, 370-373.

Shirane M. and Nakayama K.I. (2003) Inherent calcineurin inhibitor FKBP38 targets Bcl-2 to mitochondria and inhibits apoptosis. *Nature Cell Biology* **5**, 28-37.

Sich C., Improta S., Cowley D.J., Guenet C., Merly J.P., Teufel M. and Saudek V. (2000) Solution structure of a neurotrophic ligand bound to FKBP12 and its effects on protein dynamics. *Eur. J. Biochem.* **267**, 5342-5355.

Sinars C.R., Cheung-Flynn J., Rimerman R.A., Scammell J.G., Smith D.F. and Clardy J. (2003) Structure of the large FK506-binding protein FKBP51, an Hsp90-binding protein and a component of steroid receptor complexes. *Proc. Natl. Acad. Sci. USA* **100**, 868-873.

Sohocki M.M., Perrault I., Leroy B.P., Payne A.M., Dharmaraj S., Bhattacharya S.S., Kaplan J., Maumenee I.H., Koenekoop R., Meire F.M., Birch D.G., Heckenlively J.R. and Daiger S.P. (2000) Prevalence of AIPL1 mutations in inherited retinal degenerative disease. *Mol. Genet. Metabol.* **70**, 142-150.

Swindells M.B. and Ikura M. (1996) Pre-formation of the semi-open conformation by the apo calmodulin C-terminal domain and implications for binding I–Q motifs. *Nat. Struct. Biol.* **3**, 501–504.

Telford J., Boseley P., Schaffner W. and Birnstiel M. (1977) Novel screening procedure for recombinant plasmids. *Science* **195**, 391-393.

Thompson J.D., Higgins D.G. and Gibson T.J. (1994) CLUSTAL W: improving the sensitivity of progressive multiple sequence alignment through sequence weighting, position-specific gap penalties and weight matrix choice. *Nucleic Acids Res.* **22**, 4673-4680.

Tjandra N., Kuboniwa H., Ren H. and Bax A. (1995) Rotational dynamics of calcium-free calmodulin studied by ^{15}N NMR relaxation measurements. *Eur. J. Biochem.* **230**, 1014-1024.

Toutenhoofd S.L. and Strehler E.E. (2000) The calmodulin multigene family as a unique case of genetic redundancy: multiple levels of regulation to provide spatial and temporal control of calmodulin pools? *Cell Calcium* **28**, 83–96.

van der Spoel D., Lindahl E., Hess B., Groenhof G., Mark A.E. and Berendsen H.J.C. (2005) GROMACS: fast, flexible and free. *J. Comp. Chem.* **26**, 1701–1718.

Van Duyne G.D., Staendert R.F., Karplus P.A., Schreiber S.L. and Clardy J. (1991a) Atomic structure of FKBP-FK506, an immunophilin-immunosuppressant complex. *Science* **252**, 839-842.

Van Duyne G.D., Staendert R.F., Schreiber S.L. and Clardy J. (1991b) Atomic structure of the Rapamycin human immunophilin FKBP-12 complex. *J. Amer. Chem. Soc.* **113**, 7433-7434.

Van Duyne G.D., Standaert R.F., Karplus P.A., Schreiber S.L. and Clardy J. (1993) Atomic structures of the human immunophilin FKBP-12 complexes with FK506 and rapamycin. *J. Mol. Biol.* **229**, 105-124.

van Gunsteren W.F., Billeter S.R., Eising A.A., Hünenberger P.A., Krüger P., Mark A.E., Scott W.R.P. and Tironi I.G. (1996) In *Biomolecular Simulation, the GROMOS96 Manual and User Guide*. Hochschulverlag AG der ETH, Zürich.

Vetter S.W. and Leclerc E. (2003) Novel aspects of calmodulin target recognition and activation. *Eur. J. Biochem.* **270**, 404–414.

Vogel K.W., Briesewitz R., Wandless T.J., Crabtree G.R. (2001) Calcineurin inhibitors and the generalization of the presenting protein strategy. *Adv. Protein Chem.* **56**, 253–291.

Wang H.Q., Nakaya Y., Du Z., Yamane T., Shirane M., Kudo T., Takeda M., Takebayashi K., Noda Y., Nakayama K.I. and Nishimura M. (2005) Interaction of presenilins with FKBP38 promotes apoptosis by reducing mitochondrial Bcl-2. *Hum. Mol. Genet.* **14**, 1889-1902.

Wang J., Tong W., Zhang X., Chen L., Yi Z., Pan T., Hu Y., Xiang L. and Yuan Z. (2006) Hepatitis C virus non-structural protein NS5A interacts with FKBP38 and inhibits apoptosis in Huh7 hepatoma cells. *FEBS Lett.* **580**, 4392-4400.

Wedemeyer W.J., Welker E. and Scheraga H.A. (2002) Proline cis-trans isomerization and protein folding. *Biochemistry* **41**, 14637-14644.

Wehrens X.H., Lehnart S.E., Reiken S.R., Deng S.X., Vest J.A., Cervantes D., Coromilas J., Landry D.W. and Marks A.R. (2004) Protection from cardiac arrhythmia through ryanodine receptor-stabilizing protein calstabin2. *Science* **304**, 292-296.

Weiergraber O.H., Eckhoff A. and Granzin J. (2006) Crystal structure of a plant immunophilin domain involved in regulation of MDR-type ABC transporters. *FEBS Lett.* **580**, 251-255.

Weiwad M., Edlich F., Kilka S., Erdmann F., Jarczowski F., Dorn M., Moutty M.C. and Fischer G. (2006) Comparative analysis of calcineurin inhibition by complexes of immunosuppressive drugs with human FK506 binding proteins. *Biochemistry* **45**, 15776-15784.

Weiwad, M., Edlich, F., Erdmann, F., Jarczowski, F., Kilka, S., Dorn, M., Pechstein, A. and Fischer, G. (2005) A reassessment of the inhibitory capacity of human FKBP38 on calcineurin. *FEBS Letters* **579**, 1591-1596.

Wilson K.P., Yamashita M.M., Sintchak M.D., Rotstein S.H., Murcko M.A., Boger J., Thomson J.A., Fitzgibbon M.J. and Navia M.A. (1995) Comparative X-ray structures of the major binding protein for the immunosuppressant FK506 (Tacrolimus) in unliganded form and in

complex with FK506 and rapamycin. *Acta Crystallogr. D* **51**, 511-521.

Wishart D.S., Bigam C.G., Yao J., Abildgaard F., Dyson H.J., Oldfield E., Markley J.L. and Sykes B.D. (1995) ^{1}H, ^{13}C and ^{15}N chemical shift referencing in biomolecular NMR. *J. Biomol. NMR* **6**, 135–140.

Wu B., Li P., Liu Y., Lou Z., Ding Y., Shu C., Ye S., Bartlam M., Shen B. and Rao Z. (2004) 3D structure of human FK506-binding protein 52: implications for the assembly of the glucocorticoid receptor/Hsp90/immunophilin heterocomplex. *Proc. Natl. Acad. Sci. USA* **101**, 8348-8353.

Wulf G., Finn G., Suizu F. and Lu K.P. (2005) Phosphorylation-specific prolyl isomerization: is there an underlying theme? *Nat. Cell Biol.* **7**, 435-441.

Wüthrich K. (1986) In: *NMR of Proteins and Nucleic Acids*. Wiley, New York, NY.

Wüthrich K., Billeter M. and Braun W. (1983) Pseudo-structures for the 20 common amino acids for use in studies of protein conformations by measurements of intramolecular proton-proton distance constraints with nuclear magnetic resonance. *J. Mol. Biol.* **169**, 949-961.

Xia X.M., Fakler B., Rivard A., Wayman G., Johnson-Pais T., Keen J.E., Ishii T., Hirschberg B., Bond C.T., Lutsenko S., Maylie J. and Adelman J.P. (1998) Mechanism of calcium gating in small-conductance calcium-activated potassium channels. *Nature* **395**, 503–507.

Yamniuk A.P. and Vogel H.J. (2004) Calmodulin's flexibility allows for promiscuity in its interactions with target proteins and peptides. *Mol. Biotechnol.* **27**, 33-57.

Yap K.L., Ames J.B., Swindells M.B. and Ikura M. (1999) Diversity of conformational states and changes within the EF-hand protein superfamily. *Proteins* **37**, 499-507.

Yap K.L., Kim J., Truong K., Sherman M., Yuan T. and Ikura M. (2000) Calmodulin target database. *J. Struct. Funct. Genomics*. **1**, 8-14.

Zhang M. and Vogel H.J. (1994) Two-dimensional NMR studies of selenomethionyl calmodulin. *J. Mol. Biol.* **239**, 545–554.

Zhang M., Li M., Wang J.H. and Vogel H.J. (1994) The effect of Met—>Leu mutations on calmodulin's ability to activate cyclic nucleotide phosphodiesterase. *J. Biol. Chem.* **269**, 15546–15552.

Zhang M., Tanaka T. and Ikura M. (1995) Calcium-induced conformational transition revealed by the solution structure of apo calmodulin. *Nat. Struct. Biol.* **2**, 758–767.

6. Figure Index

Figure 1. Schematic representation of the human FKBPs and their domain structures …….. 3

Figure 2. Model of the regulation of apoptosis by FKBP38 in neuroblastoma cells …….. 6

Figure 3. Comparison of the three-dimensional structures of FKBP12 and the FKBP12/FK506 complex …….. 7

Figure 4. Graphic representation of the FKBP12/FK506 complex structure …….. 8

Figure 5. Comparison of the sequences and structures of FKBP domains from FKBP52, FKBP51 and *At*FKBP42 with FKBP12 …… 10

Figure 6. Superpositions of different regions of the FKBP51, FKBP52 and *At*FKBP42 structures …….. 11

Figure 7. Overall structures of holo- and apo-CaM ……. 13

Figure 8. Comparison of the N-terminal domains of apo- and holo-CaM highlighting the hydrophobic cavity in holo-CaM …….. 14

Figure 9. Comparison of the structures of holo-CaM in complex with peptides derived from different CaM-binding domains …… 16

Figure 10. Structures of CaM in complex with rat Ca^{2+}-activated K^+ channel and anthrax adenylyl cyclase …… 18

Figure 11. Picture of $FKBP38^{35-153}$ crystals and the corresponding diffraction image …… 37

Figure 12. Two-dimensional $^1H/^{15}N$-HSQC spectrum of $FKBP38^{35-153}$ …….. 38

Figure 13. Section of the NOESY spectrum as well as ^{15}N slices from the 3D $^1H/^{15}N$-NOESY-HSQC spectrum of $FKBP38^{35-153}$ …….. 39

Figure 14. Representation of the $FKBP38^{35-153}$ structure ……. 43

Figure 15. Ramachandran diagram of the 20 energy-minimized $FKBP38^{35-153}$conformers … 44

Figure 16. Structural features of $FKBP38^{35-153}$ …… 46

Figure 17. Surface potentials of FKBP12 and $FKBP38^{35-153}$ …….. 47

Figure 18. Comparison of the molecular surfaces of $FKBP38^{35-153}$ and the FKBP12/FK506

complex ……. 47

Figure 19. Atomic model of FKBP38$^{35\text{-}153}$ showing possible amino acids interacting with Ca^{2+} ……... 48

Figure 20. Superposition of a section from the $^{1}H/^{15}N$-HSQC spectrum of FKBP38$^{35\text{-}153}$, showing the shifts of certain backbone amide resonances during the titration with Ca^{2+} …… 49

Figure 21. Chemical shift perturbations produced by the addition of 7.3 mM $CaCl_2$ to a 0.4 mM solution of FKBP38$^{35\text{-}153}$ ……... 49

Figure 22. Sections from the 1D-^{1}H-NMR spectrum of FKBP38$^{35\text{-}153}$, showing the shift of certain protons during the course of titrations with $CaCl_2$ and $MgCl_2$ ……. 50

Figure 23. Section of the FKBP38$^{35\text{-}153}$ X-ray structure, showing the interactions of the Asp92 and Asp94 side-chains with the guanidinium group of Arg34 from a neighboring molecule in the crystal …….. 51

Figure 24. Two-dimensional $^{1}H/^{15}N$-HSQC spectrum of apo-CaM …… 54

Figure 25. Two-dimensional $^{1}H/^{15}N$-HSQC spectrum of holo-CaM ……... 57

Figure 26. Section from the $^{1}H/^{15}N$-HSQC spectrum of ^{15}N-labelled FKBP38$^{35\text{-}153}$, showing the changes caused in the backbone resonances by the complex formation with apo-CaM …. 58

Figure 27. Overview of the combined chemical shift changes observed for ^{15}N-labelled FKBP38$^{35\text{-}153}$ upon addition of a 3-fold molar excess of apo-CaM ……..... 58

Figure 28. Atomic model of FKBP38$^{35\text{-}153}$ showing the residues affected by the interaction with apo-CaM ……... 59

Figure 29. Section from the $^{1}H/^{15}N$-HSQC spectrum of ^{15}N-labelled apo-CaM, showing the changes produced in the backbone resonances by the complex formation with FKBP38$^{35\text{-}153}$ 60

Figure 30. Overview of the combined chemical shift changes observed for ^{15}N-labelled apo-CaM upon addition of a 3-fold molar excess of FKBP38$^{35\text{-}153}$ …….. 61

Figure 31. Atomic model of apo-CaM, showing the surface interacting with FKBP38$^{35\text{-}153}$ .. 61

Figure 32. Comparison of the sequences and surfaces of the N-terminal and C-terminal domains of CaM …… 62

Figure 33. Section from the $^{1}H/^{15}N$-HSQC spectrum of ^{15}N-labelled holo-CaM, showing

changes produced in the backbone resonances by the complex formation with FKBP38$^{35-153}$ 63

Figure 34. Overview of the combined chemical shift changes observed for ^{15}N-labelled holo-CaM upon addition of a 3-fold molar excess of FKBP38$^{35-153}$ ……. 63

Figure 35. Atomic model of holo-CaM showing the surface interacting with FKBP38$^{35-153}$ .. 63

Figure 36. Comparison of the surfaces of the N-terminal and C-terminal domains of holo-CaM ……... 64

Figure 37. Comparison of the combined chemical shift changes observed for ^{15}N-labelled apo- and holo-CaM upon addition of a 3-fold molar excess of FKBP38$^{35-153}$ ……. 65

Figure 38. Backbones superposition of apo- and holo-CaM …… 66

Figure 39. Atomic models of FKBP38$^{35-153}$, showing the amino acids affected by the interaction with apo-CaM, and the residues selected as active and passive AIRs for the docking calculation of the complex structure ……... 67

Figure 40. Ribbon representation of the backbone of the FKBP38$^{35-153}$/apo-CaM complex ... 69

Figure 41. Structure of the apo-CaM/FKBP38$^{35-153}$ complex …….. 70

Figure 42. Ribbon representation of the backbone of the FKBP38$^{35-153}$/holo-CaM complex . 72

Figure 43. Structure of the FKBP38$^{35-153}$/holo-CaM complex ……. 73

Figure 44. Electrostatic and polar interactions stabilizing the structure of the FKBP38$^{35-153}$/holo-CaM complex …….. 73

Figure 45. Comparison of the lowest energy structures of the FKBP38$^{35-153}$/CaM complexes 74

Figure 46. Comparison of the surfaces of apo- and holo-CaM involved in the complex formation with FKBP38$^{35-153}$ …… 75

Figure 47. Section from the ^{1}H/^{15}N-HSQC spectrum of ^{15}N-labelled holo-CaM, showing changes produced in the backbone resonances by the complex formation with FKBP38$^{290-313}$ 76

Figure 48. Overview of the combined chemical shift changes observed on ^{15}N-labelled holo-CaM by the addition of a 3-fold molar excess of FKBP38$^{290-313}$ ……. 76

Figure 49. Atomic model of holo-CaM, showing the residues affected by the interaction with FKBP38$^{290-313}$ …… 77

Figure 50. Section from the ^{1}H/^{15}N-HSQC spectrum of partial ^{15}N-labelled FKBP38$^{290-313}$,

showing the changes produced in the backbone resonances by the complex formation with holo-CaM and holo-CaM$^{76-148}$ …….. 79

Figure 51. Calculated structures of the FKBP38$^{290-313}$/holo-CaM complex …… 81

Figure 52. Structure of the FKBP38$^{290-313}$/holo-CaM complex ……... 82

Figure 53. Structures of the FKBP38$^{35-313}$/holo-CaM and FKBP38$^{35-313}$/semiloaded-CaM complexes ……. 83

Figure 54. Comparison of the overall structures of the edema factor/CaM and FKBP38/semiloaded-CaM complexes …… 85

Table 1. Description of the PCR experiment displaying the best results ……. 24

Table 2. X-ray data collection and refinement statistics …….. 37

Table 3. ^{1}H and ^{15}N resonance assignments of FKBP38$^{35-153}$ at 298 K and pH 6.7 …… 40

Table 4. Structural statistics of the final 20 energy-minimized FKBP38$^{35-153}$ conformers ….. 43

Table 5. ^{1}H and ^{15}N backbone amide resonance assignments of apo-CaM at 298 K and pH 6.8 …….. 53

Table 6. ^{1}H and ^{15}N resonance assignments of holo-CaM at 298 K and pH 6.8 …….. 55

Table 7. Description of the FKBP38$^{35-153}$ and apo-CaM residues that were used as active and passive AIRs in the docking calculations of the FKBP38$^{35-153}$/apo-CaM complex ……... 68

Table 8. Statistics of the final 9 conformers of the FKBP38$^{35-153}$/apo-CaM complex ……. 69

Table 9. Description of the FKBP38$^{35-153}$ and holo-CaM residues that were used as active and passive AIRs in the docking calculations of the FKBP38$^{35-153}$/holo-CaM complex …….. 71

Table 10. Statistics of the 9 conformers from cluster I of the FKBP38$^{35-153}$/holo-CaM complex ……. 72

Table 11. Statistics of the 8 conformers from cluster II of the FKBP38$^{35-153}$/holo-CaM complex ……. 73

Table 12. ^{1}H and ^{15}N resonance assignments of FKBP38$^{290-313}$ at 278 K and pH 6.8 ……. 78

Table 13. Statistics of the 8 conformers from cluster I of the FKBP38$^{290-313}$/holo-CaM complex ……. 82

7. Abbreviations

AA	Amino acid
AIR	Ambiguous interaction restraint
Apo-CaM	Calcium-free calmodulin
Bcl-2	B-cell lymphoma protein 2
bp	Base pair
BSA	Buried surface area
CaM	Calmodulin
CaMKK	CaM-dependent kinase kinase
CaN	Calcineurin (protein phosphatase 2B, PP2B)
COSY	Correlated spectroscopy
CsA	Cyclosporin A
CSP	Chemical shift perturbation
Cyp	Cyclophilin
DEAE	Diethylaminoethyl
DM-CHX	N-(N',N'-dimethylcarboxamidomethyl)cycloheximide
DNA	Deoxyribonucleic acid
dNTP	Deoxyribonucleotide phosphate
EDTA	Ethylene-diamine-tetraacetic acid
EF-hand	Ca^{2+}-binding motif
EGTA	Ethylenglycol-bis(β-aminoethylether)N,N,N',N'-tetraacetic acid
FKBP	FK506-binding protein (human if not otherwise indicated)
GPI1046	3-(3-pyridyl)-1-propyl(2S)-1-(3,3-dimethyl-1,2-dioxopentyl)-2-pyrrolidinecarboxylate
HEPES	N-2-hydroxyethylpiperazine-N'-2-ethanesufonic acid
holo-CaM	Calmodulin saturated with calcium
Hsp90	Heat shock protein 90
HSQC	Heteronuclear single quantum correlation
HTQC	Heteronuclear triple quantum correlation
IPTG	Isopropyl-β-D-thiogalactopyranoside
ITC	isothermal titration calorimetry
MALDI-TOF	Matrix-assisted laser desorption/ionization time-of-flight mass

	spectrometry
MD	Molecular dynamics
MES	2-(N-morpholino)ethanesulfonic acid
mTOR	mammalian target of rapamycin
NFAT	Nuclear factor of activated T-cell
NOE	Nuclear Overhauser enhancement
NOESY	Nuclear Overhauser enhancement spectroscopy
OD	Optical density, absorbance
OMIM	Online Mendelian inheritance in man
PCR	Polymerase chain reaction
PDB	Protein data bank
PEG	Polyethyleneglycol
PPIase	Prolyl *cis/trans* isomerase
ppm	Parts per million
PSI	Pounds per square inch
RMSD	Root mean square deviation
RNAi	RNA interference
rpm	Rotations per minute
SDS	Sodium dodecylsulfate
SDS-PAGE	Sodium dodecylsulfate - polyacrylamide gel electrophoresis
siRNA	Small interfering RNA
SK channel	small conductance Ca^{2+}-activated K^+ channel
smMLCK	Smooth muscle myosin light chain kinase
TAE	TRIS-acetate-EDTA
TOCSY	Total correlated spectroscopy
TPPI	Time proportional phase incrementation
TPR	Tetratricopeptide repeat
TRIS	Tris-(hydroxymethyl)-aminomethane
U	Unit (for enzymes)
UV-VIS	Ultra violet – visible

8. Appendix

8.1. Acknowledgments

I want to express my gratitude to several persons who made a direct or indirect contribution to the fulfillment of this work.

First to my advisor P.D. Dr. Christian Lücke, for offering me this interesting research project, for his dedicate supervision and for all I learned from him.

To Prof. Dr. Gunter Fischer, who provide the financial support and an excellent research environment, also for excellent advices.

To Dr. Frank Edlich, who has play the key role in the execution of the "FKBP38 Project", for all the preparative support, for his help in the design and execution of the different experiments, and for very productive discussions.

To Franziska Jarczowski for her decisive contribution to the cloning, expression and purification of the FKBP domain.

To Beate Rappsilber and Melanie Kirchner for doing most of the work in the preparation of several FKBP38 and CaM samples.

To Dr. Güther Jahreis, who provided the peptides for the NMR experiments.

To the AK Stubs, especially Beatrice Epler, Dr. Piotr Neumann, and Dr. Christoph Parthier, for their valuable contribution to the crystallographic structural determination of the FKBP domain.

To Monica Seidel, for valuable help in the work with the spectrometer and for been a very good friend at work.

To Lucia Moresanu-Lücke and Carmen Mrestani, who shared a lot of nice time with us, forming a small "NMR group".

To Katja Heydenreich for continuing this project, providing some new results that in fact contribute to this work.

To the rest of the collective of the Max-Planck Research Unit for Enzymology of Protein Folding, for sharing some moments at seminars, parties, etc, and for any help provided.

This work is dedicated to my wife and to my parents.

8.2. Publications

Maestre M. and Perez C. (2000) Conformational analysis of diribosylribitolphosphate by NMR spectroscopy and Molecular Dynamics. *Magn. Reson. Chem.* **38**, 123-125

Wienk H.L., **Martinez M.M.**, Yalloway G.N., Schmidt J.M., Perez C., Ruterjans H., Lohr F. (2003) Simultaneous measurement of protein one-bond and two-bond nitrogen-carbon coupling constants using an internally referenced quantitative J-correlated [^{15}N,^{1}H]-TROSY-HNC experiment. *J. Biomol. NMR* **25**, 133-45.

Suardiaz R., **Maestre M.**, Suarez E. and Perez C. (2006) Parameterization and validation of Gromos force field to use in conformational analysis of epoxidic systems. *THEOCHEM* **778**, 21–25.

Containing results from the present work:

Maestre-Martínez M., Edlich F., Jarczowski F., Weiwad M., Fischer G., Lucke C. (2006) Solution structure of the FK506-binding domain of human FKBP38. *J. Biomol. NMR* **34**, 197-202.

Edlich F., **Maestre-Martínez M.**, Jarczowski F., Weiwad M., Moutty M.C., Malesevic M., Jahreis G., Fischer G. and Lücke C. A novel calmodulin/Ca^{2+} target recognition activates the Bcl-2 regulator FKBP38. *J. Biol. Chem.* submitted

Maestre-Martinez M., Edlich F., Jahreis G., Jarczowski F., Moutty M.C., Fischer G. and Lücke C. Structural basis of FKBP38 activation by calmodulin. In preparation

Maestre-Martinez M., Edlich F., Heydenreich K., Neumann P., Parthier C., Stubbs M.T., Fischer G. and Lücke C. Calcium-binding site in the catalytic domain of FKBP38. In preparation

8.3. Curriculum vitae

Surname	Maestre Martínez
Name	Mitcheell
Date of birth	29.04.1974
Place of birth	Havana, Cuba
Citizenship	Cuban
Legal status	Married

School

1980-1986	Primary School "Jorge Agostini", Havana, Cuba
1986-1987	High School "Raul Gomez", Havana, Cuba
1987-1989	High School "Mariana Grajales", Havana, Cuba
1989-1992	Senior High School "IPVCE V.I. Lenin", Havana, Cuba

Studies

1992-1997	Chemistry studies at the Faculty of Chemistry, University of Havana
1997	Diploma in Chemistry at the Department of Physical Chemistry, Faculty of Chemistry, University of Havana. Title: "Conformational study of oligomers of the antigenic determinant of *Haemophilus influenzae* type b by NMR and Molecular Dynamics"
1997- 2002	Graduate Student at the Department of Physical Chemistry, Faculty of Chemistry, University of Havana
2002- 2003	PhD Student at the Institute for Biophysical Chemistry, University of Frankfurt
2003- 2007	PhD Student at the Max-Planck Research Unit for Enzymology of Protein Folding, Halle, Advisor: P.D. Dr. C. Lücke Dissertation under advice from: P.D. Dr. C. Lücke Topic: NMR structural characterization of FKBP38 and its interactions with calmodulin

Halle/Saale, im August 2007

Eidesstattliche Erklärung

Hiermit erkläre ich, dass die vorliegende Arbeit von mir selbständig und nur unter Verwendung der angegebene Hilfsmittel angefertigt wurde. Ich versichere weiterhin, dass alle wörtlich oder inhaltlich entnommenen Stellen als solch gekennzeichnet sind.

Diese Arbeit wurde bisher an keine andere Universität vorgelegt.

Halle/Saale, im August 2007